INFORMATION TO USERS

This manuscript has been reproduced from the microfilm master. UMI films the text directly from the original or copy submitted. Thus, some thesis and dissertation copies are in typewriter face, while others may be from any type of computer printer.

The quality of this reproduction is dependent upon the quality of the copy submitted. Broken or indistinct print, colored or poor quality illustrations and photographs, print bleedthrough, substandard margins, and improper alignment can adversely affect reproduction.

In the unlikely event that the author did not send UMI a complete manuscript and there are missing pages, these will be noted. Also, if unauthorized copyright material had to be removed, a note will indicate the deletion.

Oversize materials (e.g., maps, drawings, charts) are reproduced by sectioning the original, beginning at the upper left-hand corner and continuing from left to right in equal sections with small overlaps. Each original is also photographed in one exposure and is included in reduced form at the back of the book.

Photographs included in the original manuscript have been reproduced xerographically in this copy. Higher quality 6" x 9" black and white photographic prints are available for any photographs or illustrations appearing in this copy for an additional charge. Contact UMI directly to order.

UMI

A Bell & Howell Information Company
300 North Zeeb Road, Ann Arbor MI 48106-1346 USA
313/761-4700 800/521-0600

HARVARD UNIVERSITY

THE GRADUATE SCHOOL OF ARTS AND SCIENCES

THESIS ACCEPTANCE CERTIFICATE

The undersigned, appointed by the

Division

Department of Physics

Committee

have examined a thesis entitled
"Measurement of Photon - Charm Production in $p\bar{p}$ Collisions at $\sqrt{s}$ = 1.8 TeV"

presented by Rowan T. Hamilton

candidate for the degree of Doctor of Philosophy and hereby certify that it is worthy of acceptance.

Signature John Huth

Typed name John Huth, Chair

Signature

Typed name Melissa Franklin

Signature

Typed name Howard Georgi

Date June 12, 1996

Measurement of Photon - Charm Production in $p\bar{p}$ Collisions at $\sqrt{s}$=1.8 TeV

A thesis presented

by

Rowan T. Hamilton

to

The Department of Physics

in partial fulfillment of the requirements
for the degree of

Doctor of Philosophy

in the subject of

Physics

Harvard University
Cambridge, Massachussetts
June 1996

Abstract

The cross section for $\gamma\mu$ production in $p\bar{p}$ collisions at $\sqrt{s} = 1.8$ TeV is measured, after detailed studies of both photon and muon background subtraction methods. The results are interpreted in terms of the $p\bar{p} \rightarrow \gamma c$ cross section, after kinematic analysis excludes γb production, and the measured $\gamma\mu$ cross section is compared to a NLO calculation of the γc cross section, after correction for branching ratio and acceptance. The experimental cross section is measured to be $29 \pm 8(stat) \pm 4(sys)$ pb, while the corresponding NLO prediction is found to be $35 \pm 1(stat)$ pb.

Contents

Abstract v

Table of Contents vii

List of Tables ix

List of Figures xi

Acknowledgments xviii

1 Introduction 1

1.1 Historical Perspective 1

1.2 Experimental Observations 2

1.3 Outline of Dissertation 3

2 Theory 4

2.1 The Standard Model 4

2.1.1 Electroweak Interactions 4

2.1.2 Quantum Chromodynamics 5

2.2 Perturbative QCD and the Parton Model 10

2.2.1 Deep Inelastic Scattering 10

2.2.2 The Need for QCD 15

2.2.3 Details of QCD 15

2.3 Phenomenology of Associated Production of Photons and Charm in $p\bar{p}$ Collisions 25

3 Experiment **30**

3.1 The Tevatron 30

3.2 The CDF Detector 32

3.2.1 Vertex Time Projection Chamber 33

3.2.2 Central Tracking Chamber 35

3.2.3 Calorimetry 37

3.2.4 Central Strip Chambers 38

3.2.5 Muon Systems 38

3.3 The CDF Data Aquisition System 51

3.3.1 Level 1 51

3.3.2 Level 2 52

3.3.3 Level 3 53

3.4 The CDF Run 1A Photon Trigger 53

4 Analysis **55**

4.1 Event Selection 56

4.2 CDF Photon Trigger Efficiency and Acceptance 60

4.3 Photon Background Estimates 61

4.3.1 High Statistics Case 62

4.3.2 Low Statistics Case 63

4.4 CMX Muon Variables 66

4.5 CDF Muon Reconstruction Efficiency and Acceptance 73

4.6 Muon Background Estimates 75

4.6.1 CMX Accidental Background 76

4.6.2 Analytic Decay-in-Flight Estimate 77

4.6.3 Monte Carlo Decay-in-Flight Estimate 85

4.6.4 Background Estimate from the Data 88
4.7 Heavy Quark Background Estimates 96
4.8 Systematic Errors 106
4.9 Photon-Muon Cross Section 107
4.10 Comparison With Monte Carlo 107

5 Conclusions **110**

A Low Statistics Photon Background Estimate **113**

List of Tables

2.1 This table summarizes the properties of the matter fields. 6

2.2 Shown above are the gauge fields of the Standard Model. 7

2.3 This table summarizes the properties of the gauge fields. 7

2.4 This table summarizes the elements of the CKM matrix, and how they are experimentally determined. 8

4.1 Number of events found in the various regions of the $W - \Delta z$ plane. . 81

4.2 Numerical results of the background estimate method varying the background cuts in the $W-\Delta z$ plane. 82

4.3 Decay-in-Flight and Punch-Through Results: The first column is the decay-in-flight and punch–through estimate for the bin, the second is the number of events in the raw photon sample with muons, and the third is the number of events with real photons and muons. The final column is the number of events with real photons and prompt muons (*i.e.*, not decay-in-flight). The negative entry in the first P_T bin of the CMX results is due to the high statistics background subtraction method discussed in Section 4.3. The errors on the last two columns are statistical only, and properly include the effects of the CES weighting. 89

4.4 Calculated decay-in-flight and punch-through numbers of events using CDFSIM for several assumptions about the charged particle fractions. The numbers are normalized to the total integrated luminosity of the $\gamma - \mu$ Run 1A sample. The CMU-CMP and CMX contributions are separated. The errors in the Table are due only to the finite statistics of the simulated sample. 95

List of Figures

2-1 Shown above are the matter fields of the Standard Model. 5

2-2 The figure above describes schematically the method used to calculate hadronic cross sections in the NPM, as described in Equation 2.5. The initial state is to the left and the final state is to the right, with the dashed lines representing the final state of the hard scatter, and the solid lines representing the proton remanent. In this diagram parton flavor i from the proton (with momentum fraction x) scatters off of parton flavor j from the anti-proton (with momentum fraction x'). . . 11

2-3 The top diagram shows the topology of a typical DIS process, while the bottom diagram shows the interpretation of this process in the Naive Parton Model. Labeled are the initial and final state parton and lepton momenta, following the nomenclature of Equations 2.6 and 2.7. Q^2 denotes the invariant mass of the virtual photon exchanged. . . . 13

2-4 Typical one loop contributions from QCD. The top diagram shows one loop contribution to a quark propagator, while the bottom diagram shows a one loop contribution to a quark-gluon vertex. 17

2-5 Shown above are diagrams for the NLO contribution to DIS. Note that crossing the diagrams right for left yields the diagrams for standard Compton scattering, with the initial state off-shell photon replaced with an on-shell photon, and the final state gluon replaced with a photon. Hence the term Compton Process. 19

2-6 The nucleon structure function F_2 measured in deep inelastic scattering of electrons (SLAC), muons (BCDMS, NMC), and neutrinos (CCFR) on deuterium (BCDMS, NMC, SLAC), carbon (BCDMS C), and iron (CCFR Fe) targets. 23

2-7 Shown here are the charm structure function data points as measured by the European Muon Collaboration (EMC). The Q^2 and x regions probed at CDF are above the data points in x and offscale to the right in Q^2. 24

2-8 Shown above are some typical LO (top) and NLO (bottom) Feynman diagrams contributing to the Compton process. Note that in the bottom diagram the initial state charm quark derives from the splitting of an initial state sea gluon into a $c\bar{c}$ pair. 26

2-9 The ratio of the charm content to the total quark content of the proton as a function of x, for various values of Q. Note that for x_1x_2 values corresponding to W production at the LHC, charm makes up 20% of the quark content. 28

3-1 The accelerators and related devices used to deliver protons and antiprotons to the CDF Experiment. 31

3-2 A three dimensional perspective of CDF displaying the pertinent muon subsystems. 33

3-3 A lateral perspective of CDF displaying the relevant muon systems and calorimeter. 34

3-4 The wire layout at the endplate of the Central Tracking Chamber. . . 35

3-5 Shown above is a 3D perspective of a single wedge of the Central Electromagnetic Calorimeter. Displayed are both the lead–scintillator sandwich of the calorimeter itself, together with the phototube readout, and the position of the shower–max Central Strip chambers. . . . 39

3-6 Here we display a map of the Central Electro-Magnetic calorimeter response. The vertical axis is a 12 parameter fit to the calorimeter response for minimum ionizing particles, while the horizontal axes are the longitudinal and polar coordinates. 40
3-7 Shown above is a schematic description of a CES chamber, displaying the perpendicular cathode and anode construction. 41
3-8 An $\eta - \phi$ plot of the central muon coverage at CDF. Note the effect of the CMP's box geometry on its acceptance, and the gaps in the CMX acceptance at the top and bottom of the detector. 42
3-9 Here we display the organization of drift chambers of the CMU, in both η and ϕ space, superimposed on the structure of the CEM. 43
3-10 The structure of a single chamber of the CMU. 44
3-11 Above we display the geometry of the 16 chambers of a single CMU tower. 44
3-12 The effect of the CMP at reducing hadronic punch-through is demonstrated by the distribution of energy observed in the CHA towers traversed by muon candidates with $P_T > 15$GeV observed with CMU only stubs (dashed) and with CMU-CMP coincidence (solid). Note the strong minimum-ionizing particle peak observed for the CMU-CMP coincidence candidates. 46
3-13 The number of interaction lengths of matter traversed by a particle en route to each of the muon detectors, as a function of the polar angle θ. 47
3-14 Here we show the mechanical layout of a drift chamber for the CMP or CMX. 48
3-15 Level 2 muon trigger rates from the 1995 run for CMU only and CMU-CMP coincidence muon candidates with a 12 GeV threshold. 49
3-16 Above is displayed the geometry of the drift tube layout for a 15° CMX wedge. 50

4-1 The efficiency for the high statistics CES weighting routine to identify a CES cluster as a photon or a neutral meson, as a function of candidate E_T. Displayed are the results for both the CES method (top) and the CPR (bottom). 64

4-2 The ratio of the photon background subtraction methods, CES over CPR, for photon E_T region in which both apply. It is apparent that there is good agreement between two methods. 65

4-3 PYTHIA prediction of the charm η distribution for the charm Compton process with photons in our fiducial volume, with the approximate CMP and CMX coverage superimposed. 67

4-4 Scatter plot of the differences in slope and intercept in the transverse plane for CMX J/ψ decay tracks. The ellipse is the $\chi^2 = 1$ contour for a 2D Gaussian fit to a Monte-Carlo study of multiple scattering in the CDF detector. The left distribution corresponds to positively charged muons, the right plot to negative ones. 68

4-5 This figure displays the geometry of multiple scattering in the calorimetry in front of the CMX, and justifies our definition of the variable W. 70

4-6 Here the general characteristics of the ψ sample are displayed. The mass spectrum is presented with peak and sideband regions marked. The transverse momentum distribution is shown for signal (open) and background (dark) ,and the distribution of the number of stub hits is shown with the estimated background fraction darkened. The number of ψ candidates recorded is shown as a function of run number over the course of Run 1A. 71

4-7 The CTC-CMX track-stub mismatch resolution for the ψ sample discussed. The curves are Gaussian fits. 72

4-8 Mismatch variable distributions for muons passing the gamma-muon analysis selection cuts $p_T \geq 4$ GeV and $\chi^2_r \leq 9$. The applied cuts to separate signal and background are indicated. 74
4-9 Cuts used in the $W-\Delta z$ plane. The regions labeled as 2, 3, and 4 correspond to background, while region 1 corresponds to signal. The 4 boxes labeled as region 4 were checked and found to have a similar population. 78
4-10 Δz plotted in slices of W (top), and W plotted in slices of Δz (bottom). 79
4-11 Δz plotted in slices of W (top), and W plotted in slices of Δz (bottom), but with the signal region included. 80
4-12 P_T distribution for charged tracks fiducial to the CMP and CMX muon detectors in the 16GeV photon sample. 84
4-13 Shown here are the possible reconstruction pathologies that can occur when a charged meson decays in flight to a muon before traversing the muon chambers. 85
4-14 The decay radius for kaons and pions decaying in flight, and producing a muon candidate passing the cuts. The full histogram is for $P_T^\mu \geq 2$ GeV, and the dashed plot is for $P_T^\mu \geq 4$ GeV. Note the dip at roughly 75 cm in the kaon plot, which corresponds to the center of the CTC. The kinematic energy freed up in the kaon decay can result in a kink in the reconstructed track, which in turn gives rise to a reconstruction inefficiency, as displayed above. 90
4-15 The average number of interaction lengths a meson should punch-through to reach the CMU-CMP or the CMX, and produce a muon candidate passing our cuts, as a function of rapidity. The triangles are for pions and the circles are for kaons. 91

4-16 CHA energy deposition for muons satisfying our cuts, compared with ψ's. The data points are photon-weighted, and include both CMX and CMP muons. 92
4-17 Track-stub match χ^2 for muons satisfying our cuts, compared with ψ's. All histograms are normalized to unit area, and CES-weighted. 93
4-18 Track-stub match $\Delta R - \phi$ for muons satisfying our cuts, compared with ψ's, with the CMP and CMX displayed separately (top) and combined (bottom). All histograms are normalized to unit area, and CES-weighted. 94
4-19 The P_T^{rel} of the muon-jet system is defined as the the momentum of the muon times the sine of the opening angle between the muon and the nearest jet in $\eta - \phi$ space. 98
4-20 P_T^{rel} distributions for the $\gamma - \mu$ data compared to the PYTHIA prediction for the $\gamma - c$ and $\gamma - b$ Compton processes, all normalized to unit area. 99
4-21 P_T^{rel} distributions for data (muons) compared to random charged particles in the photon data, normalized, at top, and the same for PYTHIA $\gamma - c$ compared to PYTHIA $\gamma -$ jet, at bottom. 100
4-22 P_T^{rel} distributions for data (muons) compared to charm Monte Carlo, normalized, at top, and the same for data compared to charm Monte Carlo after smearing the Monte Carlo by a 2D Gaussian in $\eta - \phi$ space with width 0.15, at bottom. 101
4-23 $\Delta\phi$ γ - jet for charm Monte Carlo with a Gaussian fit superimposed, at top, and the same for Monte Carlo random tracks, at bottom. . . . 102
4-24 $\Delta\phi$ γ - jet for $\gamma - \mu$ data with a Gaussian fit superimposed, at top, and the same for $\gamma -$ jet data random tracks, at bottom. 103

4-25 Constrained fit (solid histogram) of the data (points) P_T^{rel} distribution to a normalized sum of the smeared Monte Carlo c (dashed) and b (dotted) distributions, with the c and b templates superimposed. Both the c and b Monte Carlo templates have been smeared in $\eta - \phi$ space by a Gaussian with width 0.15, and, as can be seen, the χ^2 of the fit is very good. The bottom fraction found, $30 \pm 15\%$, is in agreement with theoretical predictions. 104

4-26 The χ^2 of the constrained fit of the data P_T^{rel} distribution to a normalized sum of the smeared Monte Carlo $\gamma - c$ and the smeared Monte Carlo $\gamma - b$, as a function of the b-fraction. A $\Delta\chi^2$ argument for the 90% confidence level limit with 4 degrees of freedom yields $\Delta\chi^2 = 7.78$, and thus a 90% confidence level limit that the bottom fraction in this data is less than about 80%. 105

4-27 Efficiency for a charm quark to decay into a muon with P_T^{μ} above 4 GeV and fiducial to the CDF muon detectors, integrated over $P_T^{\mu} \geq P_T^{c}$. Curves displayed are for default PYTHIA fragmentation (at top), and for Peterson fragmentation with $\epsilon = 0.04$, 0.06, and 0.08 (below). . . 109

5-1 A comparison of the ratio of the measured photon-charm cross section to the PYTHIA prediction, for the three different analyses conducted at CDF during Run 1A. 112

A-1 Fractional difference in the predicted number of photons between our likelihood code and the standard photon weighting method, as a function of the number of photon candidates. 116

Acknowledgements

Graduate school is not a pleasant experience, and it can only be survived with the support of great number of people. I'd like to take a moment to thank some of the many people whose work, sometimes inadvertantly, contributed either directly or indirectly to the completion of this dissertation.

First of all, I'd like to thank all the advisors who helped steer me through the long and painful course of grad school. In chronological order, the first is Marge Shapiro, who encouraged me to think for myself. The next is Melissa Franklin, who nurtured my interest in particle physics, and then Howard Georgi, who taught me far more about theoretical physics than any experimentalist has a right to know. Finally, I'd like to thank my advisor John Huth, who gave me invaluable advice about choosing thesis topics, pestered me when I deserved to be pestered, and lead me through the final phases of my thesis. I'd also like to thank George Brandenburg for being unfailingly tolerant and patient, and putting up with me through my years in graduate school.

In addition I'd like to thank all the people who helped keep me sane throughout grad school. In particular, Martin, Suzie, Alistair, Amy, Adrian, and Kristen all worked to give me a life in Cambridge. My old friends Dave and Cindy also deserve credit for standing by me through hard times. Sarah Hogarth and Sarah Redmon were both particularly supportive when I needed it, and the technicians of HEPL are to be thanked for occasional illicit beer consumption.

I'd also like to thank the people at Fermilab who assisted both directly and indirectly in the completion of this dissertation. Phil Schlabach and Jorge de Fernandez Troconiz contributed substantially to this analysis, and were good friends as well. Brenna Flaugher and Steve Kuhlmann provided support and guidance when it was needed. And of course I must thank my local Fermilab buddies, Bob Mattingly, Steve Vejcik, Brian Harral, Chris Boswell, Doug Benjamin, Steve Hahn, and Gary Houk, even though he's a white-bread schmuck.

My mother and my sister, Nancy Anne Severson Hamilton and Rebecca Elizabeth Hamilton, were incredibly supportive and tolerant throughout my graduate years, and deserve thanks that I cannot express. And I love them very much. My niece Rachel King didn't do much to further this thesis, but deserves mention nonetheless merely for existing.

Finally, I'd like to dedicate this thesis to my father, Terrell Hunter Hamilton, who died while I was in grad school. Dad, I'm sorry you couldn't see me graduate.

WRTH.

Chapter 1

Introduction

1.1 Historical Perspective

The topic of this dissertation is particle physics. Particle physics is arguably the most fundamental science currently being probed experimentally, and it is worth taking the time to make some comments putting this field in historical perspective.

In ancient Greece Democritus theorized that all matter was composed of tiny indivisable atoms, while centuries later Mendeleev proposed that there were a structured variety of these atoms, and that they were described by the periodic table. Either one of these events might be abstractly assigned the label of the birth of particle physics, but it was Thompson's 1897 discovery of the electron and Rutherford's famous 1911 scattering experiment proving the nuclear structure of the atom, that marked the experimental maturity of particle physics. These discoveries were directly responsible for the development of quantum mechanics and eventually of quantum electrodynamics.

In the years that followed, the observation of non-conservation of energy in nuclear β decay lead Pauli to speculate in 1933 on the existence of the neutrino. This, together with the discovery of the neutron, lead to the development of the theory of the weak nuclear force, and later quantum flavor dynamics.

Subsequent discoveries of a plethora of particles lead eventually to the Standard Model of electroweak interactions with its three generations of quarks and leptons and four gauge bosons, the proposed spontaneous symmetry breaking of the electroweak sector along with its proposed mechanisms and cosmological implications, and quantum chromodynamics. These topics will be discussed in more detail in Chapter 2.

1.2 Experimental Observations

Over the course of this century experimental particle physics has enjoyed a period of great growth and excitement. The initial discoveries of the low-lying mesons and baryons lead to their description with the flavor SU(3) group, proposed in 1961 independently by Gell–Mann and Ne'eman [1], and thus the possibility of the existence of 3 constituent quarks making up all of the observed hadrons of the time.

In November 1974, however, a very narrow resonance was observed in e^+e^- collisions around 3.1 GeV, and named the ψ. This was interpreted as a quark-antiquark bound state made up of a new fourth quark named charm. This new quark supported theoretical models that explained electroweak unification and symmetry breaking, and the suppression of flavor changing neutral currents.

1977 brought the discovery of a fifth quark, named bottom, in the form of a $b\bar{b}$ resonance observed in proton–nucleus interactions with 400 GeV incident protons at Fermilab. The evident symmetry between the quark and lepton generations lead physicists to predict the existence of a partner to the bottom, named the top quark. The top quark was discovered in $p\bar{p}$ collisions at CDF in 1995.

This dissertation is devoted to the study of the $p\bar{p} \rightarrow \gamma\mu$ cross section, and its interpretation in terms of the $p\bar{p} \rightarrow \gamma c$ cross section. The $p\bar{p} \rightarrow \gamma\mu$ cross section is interesting in its own right, since it has never before been measured. In addition, the $p\bar{p} \rightarrow \gamma c$ cross section is being probed for the first time in the CDF Run 1A data, and, as discussed in Section 2.3, it is a probe of the proton charm structure function.

Future particle physics experiments have been designed in order to probe the electroweak symmetry breaking sector of the Standard Model. The most prominent of these is the LHC at CERN, which will collide protons on protons at $\sqrt{s} = 14$ TeV. At this center-of-mass energy, many physics analyses will depend on knowledge of the charm structure function of the proton. The research presented in this dissertation represents a first step towards the measurement of the charm structure function.

1.3 Outline of Dissertation

In Chapter 2 we will review the current status of the theoretical models relevant to this dissertation. We will discuss the Standard Model in both its electroweak and quantum chromodynamic sectors, and we will review what is known about the phenomenology of the $p\bar{p} \rightarrow \gamma c$ process. In Chapter 3 we will discuss the experimental apparatus used to conduct the measurement, including both the Fermilab Tevatron and the CDF Detector. Chapter 4 will describe in detail our data selection, our estimates of backgrounds, acceptances, and efficiencies, and our determination of systematic errors. Finally, in Chapter 5 we will draw conclusions from our measurement.

Chapter 2

Theory

2.1 The Standard Model

The Standard Model (SM) [2] is a theory describing the fundamental constituents of matter and their interactions which has survived all experimental challenges to date. The model describes three generations of spin-$\frac{1}{2}$ matter fields, each consisting of left-handed quark and lepton doublets and right-handed quark and lepton singlets, and their interactions which are mediated by spin-1 gauge bosons. The details of the Standard Model can be found in the literature [3], but here we will briefly review its salient points.

2.1.1 Electroweak Interactions

The Lagrangian describing the electroweak interactions respects a local gauge symmetry of $SU(2)_L \otimes U(1)$ at high energy, where the subscript L reflects the fact that only the left-handed quark and lepton components transform under the $SU(2)$ gauge group, which is to say that only left-handed particles participate in the weak nuclear interactions. At low energies, the postulated $SU(2)_L \otimes U(1)$ gauge symmetry is empirically observed to be broken down to the $U(1)$ gauge group of the electromagnetic interactions. Mechanisms for this Spontaneous Symmetry Breakdown (SSB)

have been proposed [4], but are not germane to this thesis. The pertinent features of the electroweak sector are the matter fields involved, the gauge bosons, both massive and massless, and the coefficients which couple them, including the elements of the Cabbibo-Kobayashi-Maskawa (CKM) matrix. The matter fields of the Standard Model are summarized in Figure 2-1, and their properties are summarized in Table 2.1. Correspondingly, the gauge fields of the Standard Model are summarized in Table 2.2, and their properties are summarized in Table 2.3. The interactions be-

$$\begin{pmatrix} u_L \\ d_L \end{pmatrix} \; u_R \quad \begin{pmatrix} c_L \\ s_L \end{pmatrix} \; c_R \quad \begin{pmatrix} t_L \\ b_L \end{pmatrix} \; t_R$$

$$\begin{pmatrix} e_L \\ \nu_{eL} \end{pmatrix} \; e_R \quad \begin{pmatrix} \mu_L \\ \nu_{\mu L} \end{pmatrix} \; \mu_R \quad \begin{pmatrix} \tau_L \\ \nu_{\tau L} \end{pmatrix} \; \tau_R$$

Figure 2-1: Shown above are the matter fields of the Standard Model.

tween the matter fields and the gauge fields are determined by coupling coefficients. These coefficients are uniquely determined by the SM quantities α_{EM}, α_S, $\sin\theta_W$, and the CKM matrix elements V_{ij}. The quantity α_{EM} describes the magnitude of the electro-magnetic interaction, and the quantity α_S describes the magnitude of the strong interaction, as will be described in the next section 2.1.2. The quantity $\sin\theta_W$ and the CKM matrix elements V_{ij} describe the weak interactions, and the CKM matrix elements, and how they are measured experimentally, are summarized in Table 2.4.

2.1.2 Quantum Chromodynamics

The strong nuclear interactions of the Standard Model are described by Quantum Chromodynamics, or QCD. According to this aspect of the Standard Model, the experimentally observed hadrons, both baryons and mesons, are composite particles made up of spin $\frac{1}{2}$ matter fields called quarks. QCD is a non–Abelian gauge theory

Matter Field	Strong	Weak	Electromagnetic
$\begin{pmatrix} u_L \\ d_L \end{pmatrix}$	yes	yes	yes
$\begin{pmatrix} c_L \\ s_L \end{pmatrix}$	yes	yes	yes
$\begin{pmatrix} t_L \\ b_L \end{pmatrix}$	yes	yes	yes
$\begin{pmatrix} e_L \\ \nu_{eL} \end{pmatrix}$	no	yes	yes no
$\begin{pmatrix} \mu_L \\ \nu_{\mu L} \end{pmatrix}$	no	yes	yes no
$\begin{pmatrix} \tau_L \\ \nu_{\tau L} \end{pmatrix}$	no	yes	yes no
u_R	yes	no	yes
d_R	yes	no	yes
c_R	yes	no	yes
s_R	yes	no	yes
t_R	yes	no	yes
b_R	yes	no	yes
e_R	no	no	yes
μ_R	no	no	yes
τ_R	no	no	yes

Table 2.1: This table summarizes the properties of the matter fields.

Gauge Field	Particle Name	Particle Function
g	the gluon	mediates the strong nuclear interactions
Z	the Z boson	mediates the neutral-current weak nuclear interactions
$W^{\pm}$	the W bosons	mediate the charged-current weak nuclear interactions
γ	the photon	mediates the electromagnetic interactions.

Table 2.2: Shown above are the gauge fields of the Standard Model.

Gauge Field	Strong	Weak	Electromagnetic
g	yes	no	no
Z	no	yes	no
$W^{\pm}$	no	yes	yes
γ	no	no	yes

Table 2.3: This table summarizes the properties of the gauge fields.

described by an SU(3) gauge group. The Lagrangian for QCD is shown in Equation 2.1,

$$\mathcal{L} = -\frac{1}{4}F_a^{\mu\nu}F_{a\mu\nu} + \bar{\psi}_j(i\gamma_\mu D^\mu_{jk} - M_{jk})\psi_k, \tag{2.1}$$

where the indices a, j and k refer to color and assume the values a = 1,...,8 and j, k = 1,2,3. In this expression the term D is the covariant derivative, which, acting on the quark field ψ, has the form

$$D^\mu_{jk} = \delta_{jk}\partial^\mu + ig(T_a)_{jk}G^\mu_a, \tag{2.2}$$

where the G^μ_a are the eight gluon fields, the T_a are the SU(3) generators, g is the strong coupling, and M_{jk} is the quark mass matrix. Also, the gluon field tensor $F^{\mu\nu}_a$ is given by

$$F^{\mu\nu}_a = \partial^\mu G^\nu_a - \partial^\nu G^\mu_a - g f_{abc} G^\mu_b G^\nu_c, \tag{2.3}$$

Element	Method of Measurement
V_{ud}	Nuclear β decay and Muon decay
V_{us}	Analysis of K_{e3} [1] and Hyperon decays
V_{ub}	No direct measurement. Value is 90% confidence level using $\|V_{ub}/V_{cb} = 0.08 \pm 0.02$
V_{cd}	ν and $\bar{\nu}$ production of charm off valence d quarks
V_{cs}	D_{e3} (analgous to K_{e3}) decay combined with the lifetimes τ_D
V_{cb}	Semileptonic B decays
V_{td}	B_d mixing, limits on m_t, and theoretical assumptions
V_{ts}	B_s mixing, limits on m_t, and theoretical assumptions
V_{tb}	Unitarity of the CKM Matrix

Table 2.4: This table summarizes the elements of the CKM matrix, and how they are experimentally determined.

where the constants f_{abc} are the SU(3) structure constants, defined by the commutation relations of the SU(3) generators,

$$[T_a, T_b] = i f_{abc} T_c. \tag{2.4}$$

QCD also manifests a feature unique to certain non–Abelian gauge theories [5], namely, *asymptotic freedom.* In asymptotically free theories, the strength of the interaction, in QCD described by α_S, vanishes as the Q^2, or momentum transfer, of the interaction approaches infinity. Simply put, this means that the interaction strength gets weaker as the energy scale increases – this is an example of a *running coupling constant.* There are other examples of running coupling constants to be found in the Standard Model – in fact, all of the coupling constants of the Standard Model run to some extent. The strongest coupling at low Q^2, that of QCD, decreases strongly with increasing Q^2. The next strongest coupling, that of the SU(2) sector of the electroweak interaction, also decreases with increasing Q^2, though not as steeply. (It is worth noting that, although the coupling constant of the SU(2) sector is the second strongest of the forces, the physical amplitudes of the weak nuclear interactions are additionally suppressed by large massive gauge boson denominators, which make the weak nuclear interactions the weakest of the Standard Model.) Finally, the coupling constant of the U(1) sector of the electroweak interactions runs weakly, but increases with increasing Q^2. It is speculated that at some large Q^2 these three forces become equal and can be described by subgroups of some larger unified gauge group, but such speculation is beyond the scope of this thesis.

These issues will be discussed in more depth in Section 2.2. Let us note here that since QCD is described by $SU(3)_{color}$, a QCD neutral, or color singlet, object can only be constructed from either three quarks, or a quark and an antiquark. This can be seen in group theoretic terms by the fact that both of the product representations $\mathbf{3} \otimes \mathbf{3} \otimes \mathbf{3} = \mathbf{10} \oplus \mathbf{8} \oplus \mathbf{8} \oplus \mathbf{1}$ and $\mathbf{3} \otimes \bar{\mathbf{3}} = \mathbf{8} \oplus \mathbf{1}$ contain singlet representations.

The fact that the postulated quarks are only experimentally observed as color neutral hadronic states is referred to as *confinement.* Although we cannot today

explain confinement completely in terms of QCD, lattice gauge calculations are having some success in describing the low energy properties of, *e.g.*, kaons, glueballs, etc.

2.2 Perturbative QCD and the Parton Model

We begin our discussion of perturbative QCD by studying Deep Inelastic Scattering (DIS) and the Naive Parton Model (NPM). Although an analysis of DIS does not involve QCD directly, it does set the stage for a more in-depth discussion of perturbative QCD.

In the NPM, the phenomenology of $p\bar{p}$ collisions is conceptually simple. One calculates the leading order parton level cross section for the process one in which is interested, $\sigma_{q_iq_j\to X}$ (where q_i and q_j are the initial state partons involved in the scatter, and X is the final state of the process of interest), using the empirically determined value of α_S. One then convolutes this calculation with experimentally measured *parton distribution functions* $q_i(x)$, where $q_i(x)$ represents the probability that in a $p\bar{p}$ hard scatter one finds a parton q of flavor i at momentum fraction x, where x is the fraction of the proton 3-momentum carried by the parton q, as shown below and described schematically in Figure 2-2:

$$\sigma_{p\bar{p}\to X} = \sum_{\text{partons } i,j} \int_0^1 dx dx' \sigma_{q_iq_j\to X} q_i(x) q_j(x') \tag{2.5}$$

For now, we will restrict our discussion to the light parton distribution functions. Discussion of the heavy quark distribution functions involves subtleties that will be studied in Section 2.3.

2.2.1 Deep Inelastic Scattering

Experimentally, the parton distribution functions are determined by measuring *structure functions* in, *e.g.*, deep inelastic scattering (DIS), which is the process of scattering energetic leptons off protons, as shown in Figure 2-3. The proton structure

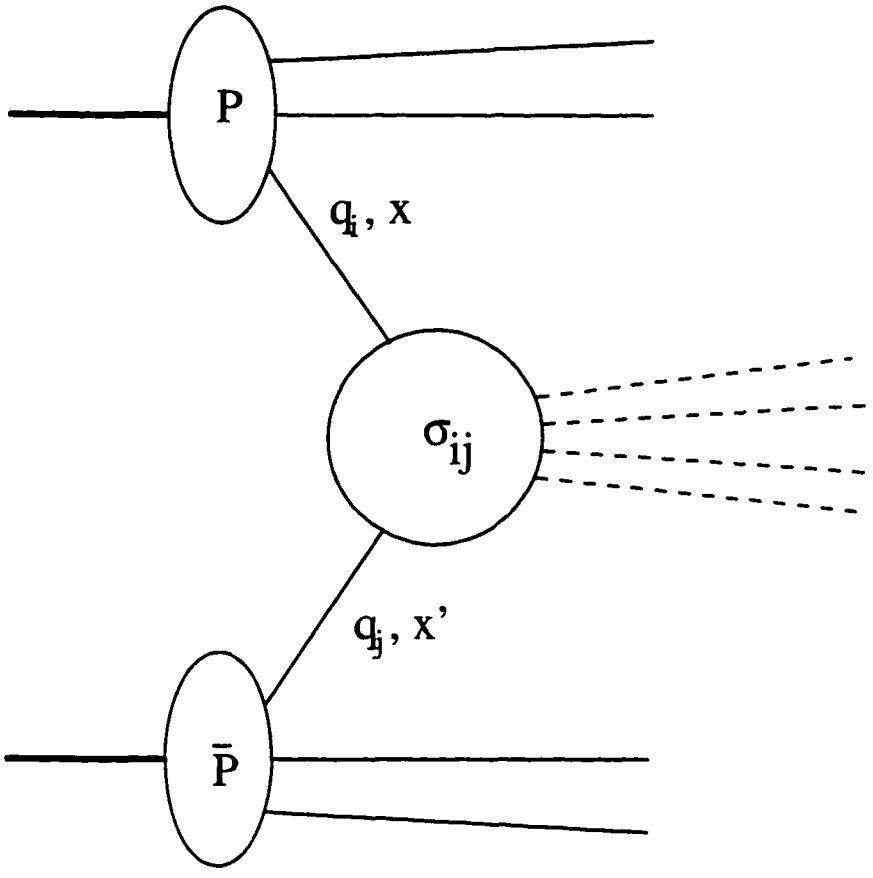

Figure 2-2: The figure above describes schematically the method used to calculate hadronic cross sections in the NPM, as described in Equation 2.5. The initial state is to the left and the final state is to the right, with the dashed lines representing the final state of the hard scatter, and the solid lines representing the proton remanent. In this diagram parton flavor i from the proton (with momentum fraction x) scatters off of parton flavor j from the anti-proton (with momentum fraction x').

functions are also studied with other processes like direct-photon and jet production in hadron collisions, but here we limit ourselves to DIS for ease of discussion.

In DIS the squared and spin-averaged matrix element for the process is expressed in terms of the lepton and hadron tensors $L^{\alpha\beta}$ and $W_{\alpha\beta}$, which themselves depend on the initial and final state lepton momenta (k and k') and the initial and final state parton momenta (p and p')

$$L_{\alpha\beta} = \frac{1}{2}\sum_{spins}\left[\bar{u}(k')\gamma^{\alpha}\mathcal{O}u(k)\right]\left[\bar{u}(k')\gamma^{\beta}\mathcal{O}u(k)\right]^{*}, \tag{2.6}$$

$$W_{\alpha\beta} = \frac{1}{2}\sum_{spins}\int\langle X|J_{\alpha}|p\rangle\langle X|J_{\beta}|p\rangle^{*}(2\pi)^{3-3n}\frac{d_n(PS)}{2E_p}, \tag{2.7}$$

where $\mathcal{O}$ is the appropriate operator for the coupling at the lepton vertex, J is the appropriate hadronic current, and $d_n(PS)$ is the n-body Lorentz invariant phase space for the final state hadrons. The variables p, p', k, and k' are the initial and final state parton and lepton momenta, as shown in Figure 2-3.

In terms of these tensors the inclusive spin-averaged cross section can be expressed as

$$E_{k'}\frac{d\sigma}{d^3k'} = \frac{1}{16\pi^2 E_k}\frac{g^4}{|D|^2}L^{\alpha\beta}W_{\alpha\beta}, \tag{2.8}$$

where g^4 represents the appropriate combination of coupling constants and D is the denominator of the gauge boson propagator. The Lorentz structure of the hadronic tensor described above dictates that it can be decomposed into six terms. In the limit of vanishing lepton masses, however, three of these vanish when contracted with $L^{\alpha\beta}$. Thus the pertinent parts of the hadronic tensor can be written as

$$W_{\alpha\beta} = -g_{\alpha\beta}W_1 + \frac{p_\alpha p_\beta}{M^2}W_2 - \frac{i\epsilon_{\alpha\beta\delta\gamma}p^{\gamma}q^{\delta}}{2M^2}W_3, \tag{2.9}$$

where q is the 4-momentum of the off-shell photon mediating the scatter, and p is 4-momentum of the initial state parton involved in the interaction. The empirically determined structure functions W_1, W_2, and W_3 can depend only on $\nu = \frac{p\cdot q}{M}$ and

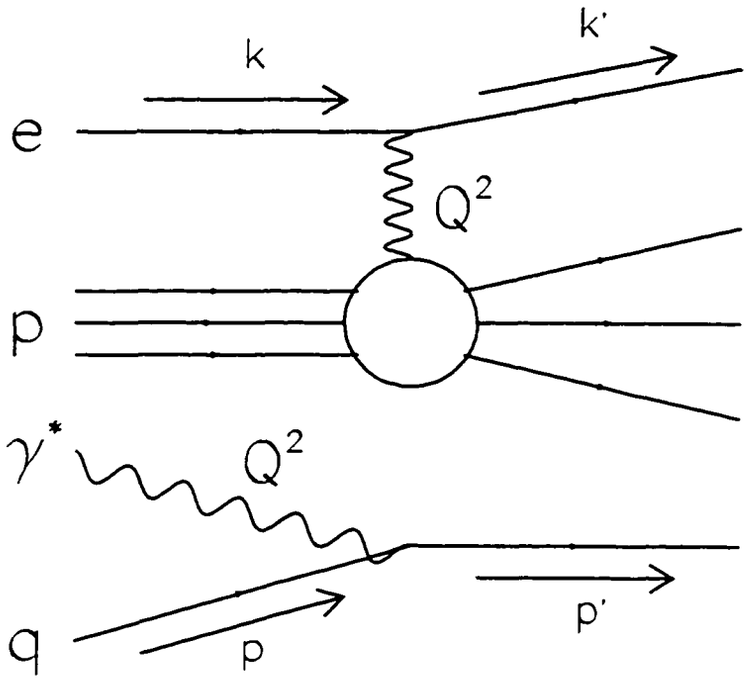

Figure 2-3: The top diagram shows the topology of a typical DIS process, while the bottom diagram shows the interpretation of this process in the Naive Parton Model. Labeled are the initial and final state parton and lepton momenta, following the nomenclature of Equations 2.6 and 2.7. Q^2 denotes the invariant mass of the virtual photon exchanged.

$Q^2 = -q^2$, since these variables comprise a maximal set of uncorrelated variables derived purely from the kinematics of the process. The coefficient of W_3 is odd under parity, and thus this term vanishes for photon exchange (though not for neutrino DIS), and the term W_1 can be expressed in terms of W_2, as will be shown presently. The remaining term, W_2, is usually written as $F_2 = \nu W_2$.

These structure functions are intimately related to the parton distribution functions. In the Naive Parton Model (NPM), F_1 and F_2 satisfy the relation

$$F_1(x) = x^{-1}F_2(x) = \sum_q e_q^2 \int \frac{dw}{w} q(w)\delta\left(1 - \frac{x}{w}\right) = \sum_q e_q^2 q(x), \tag{2.10}$$

where e_q^2 is the electromagnetic charge of parton flavor q. Note the appearance of the delta-function $\delta(1 - x/w)$, imposing the kinematic requirement that $x = w$, *i.e.* that the momentum fraction in the parton distribution function equal that of the structure function.

The fact that the structure functions in the above relation depend only on x is merely a reflection of the assertion that the partons can be treated as free point-like particles within the proton. When higher-order QCD effects are included, things are not so simple. On the one hand, the QCD coupling α_S depends on the Q^2 of the process; on the other hand, the initial and final state partons are capable of gluon bremsstrahlung, thus altering the Q^2 dependence of the measured quantity. Both of these effects conspire to introduce Q^2 dependence to both the structure functions and the parton distributions. The fact that the NPM lacks this dependence is referred to as *approximate scaling*, and is observed experimentally.

The above mentioned parton distribution functions have been analyzed in detail by several groups, notably by Martin, Roberts, and Stirling (MRS), and by the CTEQ collaboration, as described by [6] and [7] and the references there contained.

2.2.2 The Need for QCD

The above discussion neglects several issues key to the historical development of QCD. The first of these is the spin statistics problem, which noted early on that there was an inconsistency in the parton model of hadrons composed of constituent fermionic quarks. For example, the Δ^{++} baryon is experimentally observed to have a spin of $\frac{3}{2}$, while the the Standard Model requires that its flavor structure be $|uuu\rangle$. This means that the Δ^{++} wave function must be symmetric under interchange of the constituent fermions, which contradicts the spin statistics theorem, one of the fundamental theorems of quantum mechanics. The theoretical answer to this apparent contradiction was to add a new quantum number to the partons, namely the color of QCD, in order to antisymmetrize the wave function.

Once it was determined that a new quantum number was necessary for the partons, it then became necessary to determine the range of values that quantum number could take. This was measured by studying the quantity

$$R = \frac{\sigma(e^+e^- \rightarrow hadrons)}{\sigma(e^+e^- \rightarrow \mu^+\mu^-)}. \tag{2.11}$$

Here, the only differences between the hadronic and muonic cross sections are the charges of the partons and number of color states summed over in the hadronic final state. The charges of the partons are determined by the charges of the observed hadronic bound states, and thus R determines the number of colors. From studies of R the number of colors was found to be 3; thus, the SU(3) gauge group was proposed for QCD.

2.2.3 Details of QCD

The fact that QCD is an asymptotically free theory allows perturbative QCD calculations at sufficiently high energies. At low energies, α_S is sufficiently large that the expansion in terms of the coupling coefficient does not converge rapidly, so perturbation theory fails.

At energies much greater than 1 GeV, however, α_S becomes small enough that perturbation theory becomes a valid tool. For any given QCD process, at Leading Order (LO) in perturbation theory one has the NPM, where one treats the partons as free point-like particles within the proton, and one assumes that α_S does not run. (In fact, in the NPM, α_S is generally not an issue, since it typically deals with processes like DIS.) The NPM, of course, neglects a great deal of the physics content of QCD, since the valence quarks are not free, but rather are bound by the strong nuclear force. This is especially true for the process studied here, given that neither of the initial state partons is a valence quark – one is a gluon and the other is a charm quark resulting from an upstream gluon splitting.

At higher-orders in perturbation theory, perturbative QCD suffers from ultra-violet divergences due to loop diagrams. These loop diagrams, *e.g.*, those shown in Figure 2-4, are evaluated by integrating over all possible momenta for each closed loop, and some of these diagrams are divergent when evaluated to arbitrarily high loop momenta. A variety of tools have been developed to deal with these divergences, and these methods are refered to as *renormalization techniques.* One effect of these renormalization techniques is the running of the effective QCD coupling constant. If α_S is measured at one particular $Q^2 = \mu^2$, then evaluation of the appropriate loop diagrams allows one to extrapolate its value at a different Q^2 via the relation

$$\alpha_S(Q^2) = \frac{\alpha_S(\mu^2)}{1 + 4\pi b \alpha_S(\mu^2) ln(Q^2/\mu^2)}. \tag{2.12}$$

where $b = \frac{1}{48\pi^2}(33 - 2n_f)$ and n_f is the number of flavors contributing to the loops. The factor of 33 in the above relation is determined by the SU(3) gauge group structure of QCD. It is convention at this point to recast the above equation in a form that replaces the measured value of α_S at a fixed reference scale with a dimensional parameter Λ,

$$\alpha_S(Q^2) = \frac{1}{4\pi b \ln(Q^2/\Lambda^2)} = \frac{12\pi}{(33 - 2n_f)\ln(Q^2/\Lambda^2)}. \tag{2.13}$$

The conventional fixed reference scale used to determine the value of the parameter Λ is $\mu^2 = M_Z^2$, and the experimental results from the LEP collider at CERN, operating

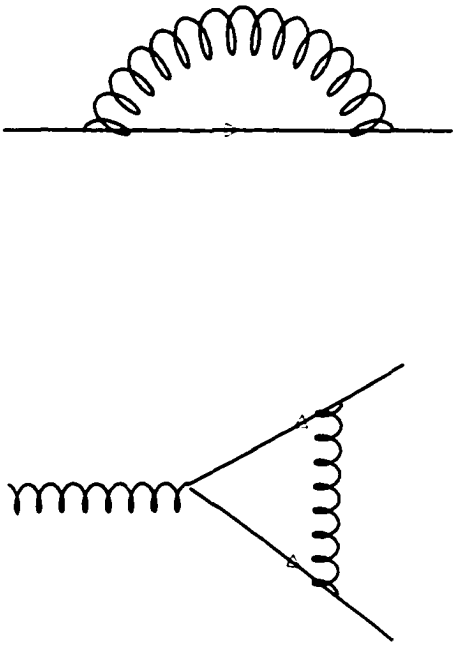

Figure 2-4: Typical one loop contributions from QCD. The top diagram shows one loop contribution to a quark propagator, while the bottom diagram shows a one loop contribution to a quark-gluon vertex.

on resonance at the Z mass, are used to measure its value at $\alpha_S(M_Z) = 0.1134 \pm 0.0035$ [8].

As mentioned in Section 2.2.1, QCD introduces a Q^2 dependence not only to α_S, but also to the structure functions and parton distribution functions. The Q^2 dependence of the nucleon structure function $F_2(x, Q^2)$ is shown in Figure 2-6 [8], where the data are diplayed for a variety of experiments. The Q^2 dependence of the parton distribution functions is apparent on the one hand from the fact that all partons, light and heavy alike, have some probability of coming from the sea, and thus from an upstream gluon splitting, and on the other hand from the possibility of initial or final state gluon bremstrahlung from a parton. This Q^2 dependence can be understood in a number of ways, but here we describe only the methods of Dokshitzer, Gribov, and Lipatov and of Altarelli and Parisi [9], collectively referred to as the DGLAP method, simply due to ease of discussion.

For simplicity, we discuss the case of electron-proton scattering mediated by a virtual photon. In the DGLAP approach, one studies this process by starting with the calculation of the NLO contribution in perturbative QCD. This amounts to adding a single gluon brem to either the initial or final state quark leg, as shown in Figure 2-5. These diagrams are referred to as the QCD Compton Process, since they are obviously intimately related to traditional Compton Scattering. In fact, the spin-averaged matrix element for the Compton Process is identical to that for Compton Scattering, up to a multiplicative constant due to the summing of the gluon color states. From this calculation one finds that the equation for $x^{-1}F_2$ becomes

$$x^{-1}F_2 = 4\alpha_S \sum_q e_q^2 \int_x^1 \frac{dw}{w} q(w) \int d(PS) \frac{4}{3} \left[\frac{\hat{s}}{-\hat{t}} + \frac{-\hat{t}}{\hat{s}} + \frac{2\hat{u}Q^2}{\hat{s}\hat{t}} \right], \qquad (2.14)$$

where the phase space integration is over the final state gluon and the parton distribution functions $q(w)$ are the bare functions from which the Q^2 dependence will be calculated. We note here that, at this order, F_1 no longer equals $x^{-1}F_2$, and that since F_2 satisfies the Adler sum rules, consistent with the parton model, F_1 no longer has a simple interpretation within the parton model.

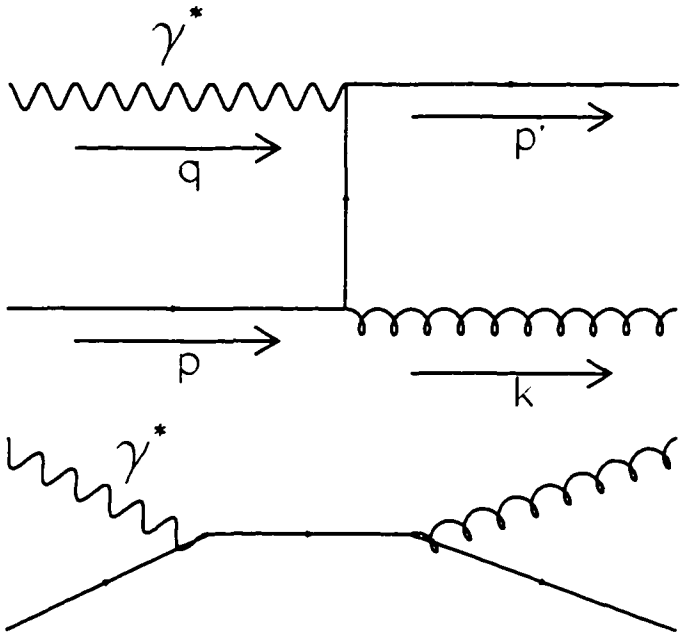

Figure 2-5: Shown above are diagrams for the NLO contribution to DIS. Note that crossing the diagrams right for left yields the diagrams for standard Compton scattering, with the initial state off-shell photon replaced with an on-shell photon, and the final state gluon replaced with a photon. Hence the term Compton Process.

In this expression the Mandelstam variables $\hat{s}$, $\hat{t}$, and $\hat{u}$ are given by

$$\hat{s} = (p' + k)^2 \tag{2.15}$$

$$\hat{t} = (p - k)^2 \tag{2.16}$$

$$\hat{u} = (p - p')^2, \tag{2.17}$$

where the momenta are defined in Figure 2-5. This expression introduces two singularities, the first of which is an infrared singularity when the emitted gluon has zero momentum. This singularity is canceled by contributions from the one-loop vertex corrections. The second singularity occurs at $\hat{t} = 0$ and is due to the possibility of collinear gluon emission with non-zero momentum, and this singularity, the *mass singularity*, requires a regularization distinct from the renormalization of most perturbative calculations. In this manner the mass singularity is absorbed into the bare parton distribution function, resulting in a renormalized parton distribution function which is finite, but dependent on Q^2. This separation of long-distance and short-distance effects is referred to as *factorization*, and it results in two mass scales being introduced into the calculation, μ and μ_f. The former is the renormalization scale common to perturbative calculations, while the latter, specific to factorization calculations, is refered to as the *factorization scale*. Roughly speaking, one may consider any propagator off-shell by more than μ_f^2 as contributing to the hard scatter, and any propagator off-shell by less than μ_f^2 as contributing to the parton distribution function. The value of μ_f depends on the factorization scheme invoked, however it is often convenient to set $\mu_f = \mu$, as we now do here. In this simple factorization scheme one finds that after, regularization at NLO, F_2 can be expressed in terms of the single mass scale μ as

$$x^{-1}F_2 = \sum_q e_q^2 \int \frac{dw}{w} q(w) \left[\delta\left(1 - \frac{x}{w}\right) + \frac{\alpha_S}{2\pi} P_{qq}\left(\frac{x}{w}\right) \ln\left(\frac{Q^2}{\mu^2}\right) \right] \tag{2.18}$$

where the delta function term is simply the NPM contribution discussed earlier. This

relation refers to the *quark-quark splitting function* $P_{qq}(z)$, where

$$z = \frac{x}{w} = \frac{Q^2}{2p \cdot q} = \frac{Q^2}{\hat{s} + Q^2}, \tag{2.19}$$

and P_{qq} is given by

$$P_{qq}(z) = \frac{4}{3}\left(\frac{1+z^2}{1-z}\right). \tag{2.20}$$

It is worth noting that P_{qq} describes the probability of a quark turning into a quark with the emission of a gluon, and that it is, in fact, independent of the regularization prescription. This quantity is determined by the regularization of the $\frac{1}{t} = 0$ singularity in Equation 2.14.

Equation 2.18 neglects several important effects. First of all, the one-loop vertex corrections that cancel the aforementioned, infrared divergence and give rise to the running of α_S have not been included. Also, the possibility of the initial state quark arising from splitting off an initial state gluon has not been included. To address these issues, one first notes that Equation 2.18 can be rewritten as a differential equation for $q(x, Q^2)$,

$$\frac{dq(x,Q^2)}{d(\ln(Q^2)} = \frac{\alpha_s(Q^2)}{2\pi}\int_x^1 \frac{dw}{w} q(w,Q^2) P_{qq}\left(\frac{x}{w}\right) + \mathcal{O}(\alpha_S^2(Q^2)\ln Q^2) \tag{2.21}$$

Solving this equation by iteration will generate the contributions to q of order $(\alpha_S \ln Q^2)^n$ from n-fold collinear gluon emission. This is known as the *Leading Log Approximation.* Adding the leading log contribution from vertex and propagator loop diagrams amounts merely to using the running coupling $\alpha_S(Q^2)$ in the above relation.

In order to address the possibility that the initial state quark came from a gluon, one can calculate gluon-quark, quark-gluon, and gluon-gluon splitting functions, analogous to the quark-quark splitting function, in the same manner that the quark-quark splitting function was calculated:

$$P_{qg}(z) = \frac{1}{2}\left[z^2 + (1-z)^2\right], \tag{2.22}$$

$$P_{gq}(z) = \frac{4}{3}\left(\frac{1+(1-z)^2}{z}\right), \tag{2.23}$$

and

$$P_{gg}(z) = 6\left[\frac{z}{(1-z)_+} + \frac{1-z}{z} + z(1-z) + \left(\frac{11}{12} - \frac{n_f}{18}\right)\delta(1-z)\right]. \tag{2.24}$$

With these one finds that the evolution function for the quark distribution functions to be given by

$$\frac{dq_i(x,Q^2)}{d(\ln(Q^2))} = \frac{\alpha_S(Q^2)}{2\pi}\int_x^1 \frac{dw}{w}\left[q_i(w,Q^2)P_{qq}\left(\frac{x}{w}\right) + g(w,Q^2)P_{gq}\left(\frac{x}{w}\right)\right]. \tag{2.25}$$

When one is studying heavy quark distribution functions, the Q^2 evolution of the distribution function is a bit more complicated. The heavy quark distibution functions are sea quark distribution functions, where the name *sea quark* serves to denote the difference between the intrinsic *uud valence* quark content of the proton, and the virtual cloud (or *sea*) of gluons and $q\bar{q}$ pairs one expects from the laws of quantum mechanics. The usual approach in dealing with the heavy quarks is to set the heavy quark distribution function to zero below mass threshold, and at the mass threshold turn the function on and evolve up via Altarelli-Parisi. However, most Altarelli-Parisi calculations neglect mass terms, and in the region near the mass threshold the mass terms can be important. These issues will be dealt with in Section 2.3.

We also note here that the experimental data for the charm content of the proton are somewhat scant. The CCFR Collaboration has placed a limit on the fraction of quarks in the nucleon constituting charm [10] by studying wrong-sign single muon production in ν_μ–nucleon interactions. Neglecting the strange content of the nucleon, they place a limit on the charm quark content of 0.035 at 90% CL. The European Muon Collaboration (EMC) has explicitly measured the charm structure function of the nucleon F_2^c [11] by studying the process $\mu N \rightarrow c\bar{c}X$, and in Figure 2-7 we show the EMC results superimposed on the corresponding MRS fits [6]. Note that the x and Q^2 regions probed by CDF lie above and to the right of the data points in Figure 2-7, and thus at CDF we are studying the charm structure function in a regime never before investigated.

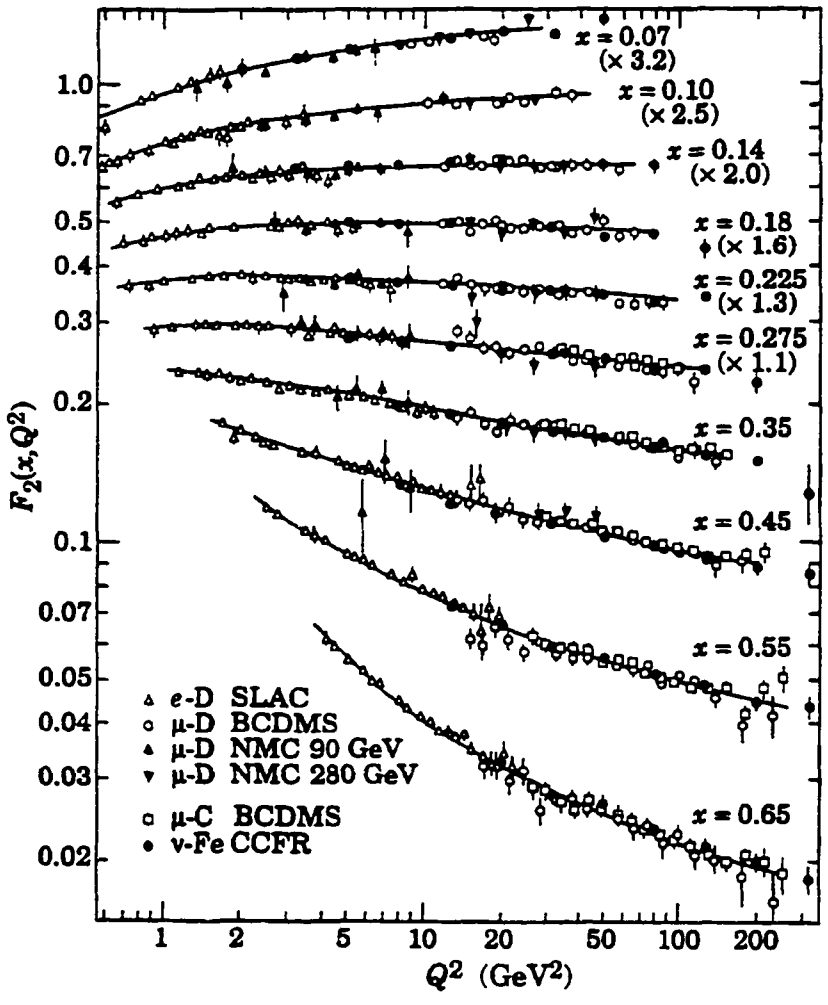

Figure 2-6: The nucleon structure function F_2 measured in deep inelastic scattering of electrons (SLAC), muons (BCDMS, NMC), and neutrinos (CCFR) on deuterium (BCDMS, NMC, SLAC), carbon (BCDMS C), and iron (CCFR Fe) targets.

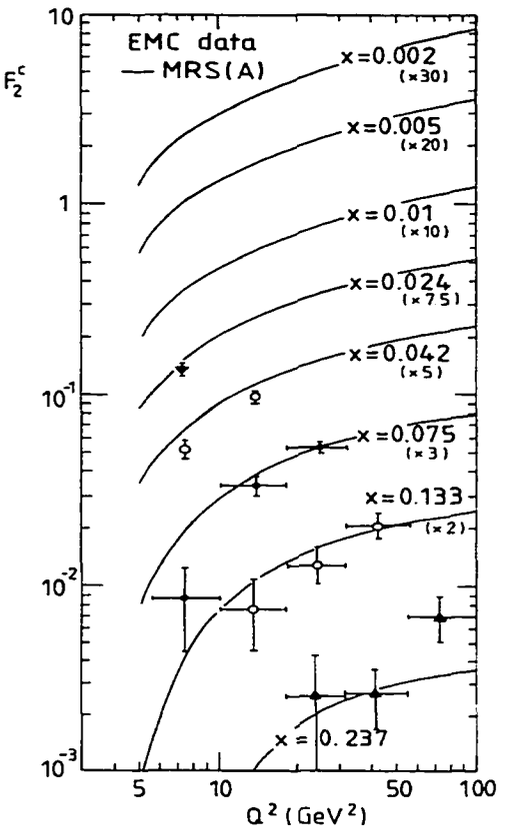

Figure 2-7: Shown here are the charm structure function data points as measured by the European Muon Collaboration (EMC). The Q^2 and x regions probed at CDF are above the data points in x and offscale to the right in Q^2.

2.3 Phenomenology of Associated Production of Photons and Charm in $p\bar{p}$ Collisions

The study of the $p\bar{p} \rightarrow \gamma\mu + X$ process involves two primary components - namely the phenomenology of the $p\bar{p} \rightarrow \gamma c + X$ process, including both the $gc \rightarrow \gamma c$ subprocess and the $gg \rightarrow \gamma c\bar{c}$ subprocess, where the $c\bar{c}$ pair result from initial state gluon splitting, and the $\gamma\mu$ final states due to bottom quark production and due to final state gluon splitting into charm. All of these processes will be discussed here. Of course, there are also experimental backgrounds due to neutral mesons mimicking photons and due to decays-in-flight of light charged mesons and punch throughs into the muon chambers, but these will be dealt with later in Sections 4.3 and 4.6.

A number of references can be found in the literature studying the phenomenolgy of the $p\bar{p} \rightarrow \gamma c$ process, most notably the analysis of Fletcher, Halzen, and Zas [12] and that of Stratmann and Vogelsang [13]. In the former analysis the authors perform a straightforward LO calculation, including the dependence of the process on the gluon distribution function via initial state gluon splitting. The latter analysis studies the differences found between including and neglecting the charm mass terms in the LO calculation; Strattman and Volgelsang find little difference in the two approaches.

In addition to the calculations of Fletcher, Halzen and Zas and of Stratmann and Vogelsang, Bailey, Berger and Gordon have performed a NLO massless calculation [15], which incorporates a combination of analytic and Monte Carlo techniques. This calculation is particularly appropriate to this analysis for two reasons. First of all, the combination of analytic and Monte Carlo techniques employed allows them to apply the same photon isolation cuts that are applied to the CDF data. Also, they provide a calculation of the differential cross section $\frac{d\sigma}{dE_t^{charm}}$. This differential cross section allows us to convolute their results with the PYTHIA Monte Carlo prediction [14] for the efficiency of a charm quark to decay into a muon in our fiducial volume, and thus allows us to compare their calculation directly with our measured

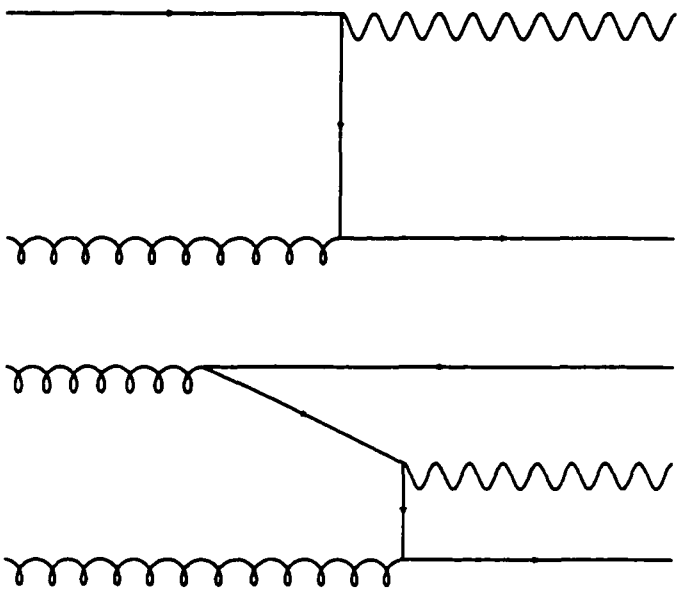

Figure 2-8: Shown above are some typical LO (top) and NLO (bottom) Feynman diagrams contributing to the Compton process. Note that in the bottom diagram the initial state charm quark derives from the splitting of an initial state sea gluon into a $c\bar{c}$ pair.

photon–muon cross section.

Finally, we note that this measurement has impact on future collider experiments, regardless of which calculational approach is taken. One would expect that at high enough center–of–mass energies, and at small x, where the valence quarks are less important, and at Q^2's well above the charm mass threshold, an approximate SU(4) flavor symmetry would hold, so that a significant fraction of the proton's momentum would be carried by charm quarks. In fact, CTEQ [7] estimates that at LHC energies as much as 20% of the quark content of the proton can be charm, as shown in Figure 2-9 [16].

We also note here that the charm structure function is interesting in its own right, regardless of its importance to future experiments. The charm structure function is a structure function whose parameters are mostly specified by the physics of the Standard Model. Although there are subtleties at the charm mass threshold, evolution above the threshold is completely determined by the DGLAP equations, and, well above threshold, the threshold effects are negligible compared to the effects of the DGLAP evolution.

In addition to the phenomenology of the signal process, we here discuss potential background processes such as γb and $\gamma c\bar{c}$ production. One knows immediately that γb Compton production will be suppressed relative to γc Compton production by a factor of 4 due to the electromagnetic vertices involved, and one would expect a further suppression due to the differences in the parton masses involved. Lionel Gordon *et al.* have estimated that the bottom to charm ratio in photon events at CDF is given by [17]

$$\frac{\gamma c + \gamma c\bar{c}}{\gamma b + \gamma b\bar{b}} = \frac{8}{1}. \tag{2.26}$$

In order to estimate expermentally the relative b and c content of our data, we searched for kinematic variables to differentiate the two processes. We found one, but ultimately determined that the statistics of this measurement were not sufficient to concretely distinguish the two, as discussed in Section 4.7.

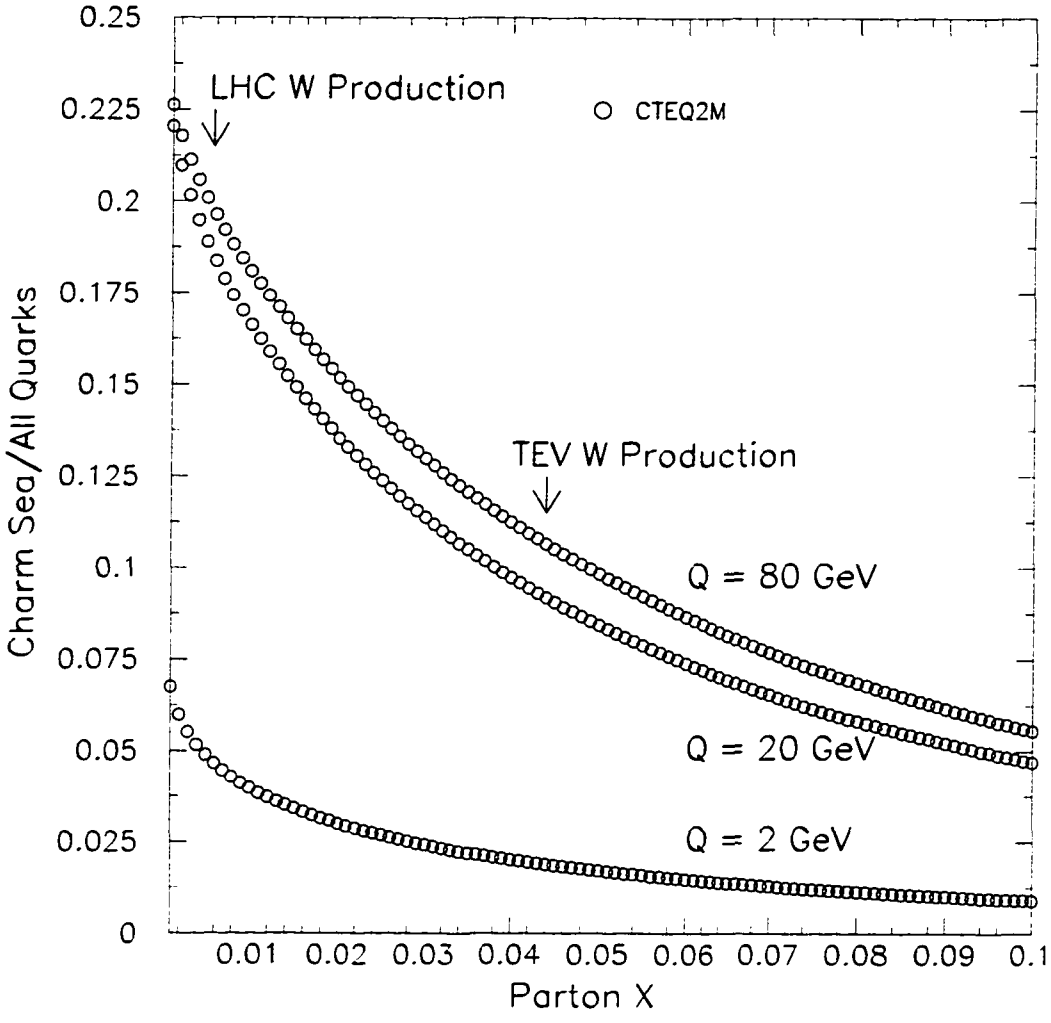

Figure 2-9: The ratio of the charm content to the total quark content of the proton as a function of x, for various values of Q. Note that for $x_1 x_2$ values corresponding to W production at the LHC, charm makes up 20% of the quark content.

The $\gamma c\bar{c}$ final state, while a background to the LO calculations, is in fact a part of the signal for the NLO calculation of Gordon, *et al.*, where the $2 \rightarrow 3$ processes have been explicitly included. Nonetheless, we have estimated the rate of charm production in jets recoiling against photons by performing a Monte Carlo study using PYTHIA with string fragmentation. We found that 5% of PYTHIA's gluon derived jets contained charm, while 0.6% of PYTHIA's quark derived jets contained charm. Using these numbers, and PYTHIA derived cross sections, we determined

$$\frac{\sigma(p\bar{p} \rightarrow \gamma \text{jet} \rightarrow \gamma c\bar{c})}{\sigma(p\bar{p} \rightarrow \gamma c)} = \frac{1}{9} \tag{2.27}$$

where the numerator includes contributions derived from both gluons and light quarks, and the denominator includes only the charm Compton process. We conclude that, given the statistics of this measurement, the $\gamma c\bar{c}$ background is not relevant to this analysis, and the γb background, though larger than $\gamma c\bar{c}$, is still much smaller than the statistical errors on the measurement.

In conclusion, we reiterate that the cross section $\sigma_{p\bar{p}\rightarrow c\gamma}$ has never before been measured, and that this measurement was made possible due to the luminosity delivered to CDF by the Tevatron during Run 1A. In addition to the $\gamma\mu$ analysis presented here, CDF is conducting separate analyses looking for the γe final state [22], and searching for $\gamma - c$ final states by fully reconstructing $\gamma - D^*$ events where the D^* decays in the mode $D^* \rightarrow D\pi \rightarrow K\pi\pi$, as discussed in [18].]

Chapter 3

Experiment

3.1 The Tevatron

The Tevatron at the Fermi National Accelerator Laboratory is a superconducting synchrotron designed to store and collide protons and antiprotons at a center-of-mass energy of $\sqrt{s} = 1.8$TeV. Although the Tevatron is the final accelerator used to deliver beam to the CDF Experiment, a number of other particle accelerators are used to provide the protons and antiprotons and to accelerate to sufficient energy for injection to the Tevatron. Here we will discuss the accelerators and other devices used at Fermilab to create, accelerate, and finally collide protons and antiprotons in the Tevatron.

Figure 3-1 displays the Tevatron and related accelerators. The production and acceleration of protons begins with the negative ionization of a small sample of hydrogen gas, and the subsequent acceleration of the H^- ions to 750 KeV in a Cockroft-Walton electrostatic accelerator. This is followed by a linear accelerator, which boosts the ions to 200 MeV. The negative ions are chosen (rather than bare protons) in order to facilitate injection into the next stage - the Booster Ring. At the point of injection the negative ions and the pre-existing protons in the Booster Ring are merged through a single magnetic field into a straight portion of the ring, and then passed

through a thin foil in order to remove the excess electrons from the negative ions. The Booster Ring is a synchrotron accelerator which boosts the protons to 8 GeV and then injects them into the Main Ring. The Main Ring is a synchrotron which can be used either to boost protons and antiprotons to 150 GeV for Tevatron injection, or to boost protons to 120 GeV to be used for antiproton production.

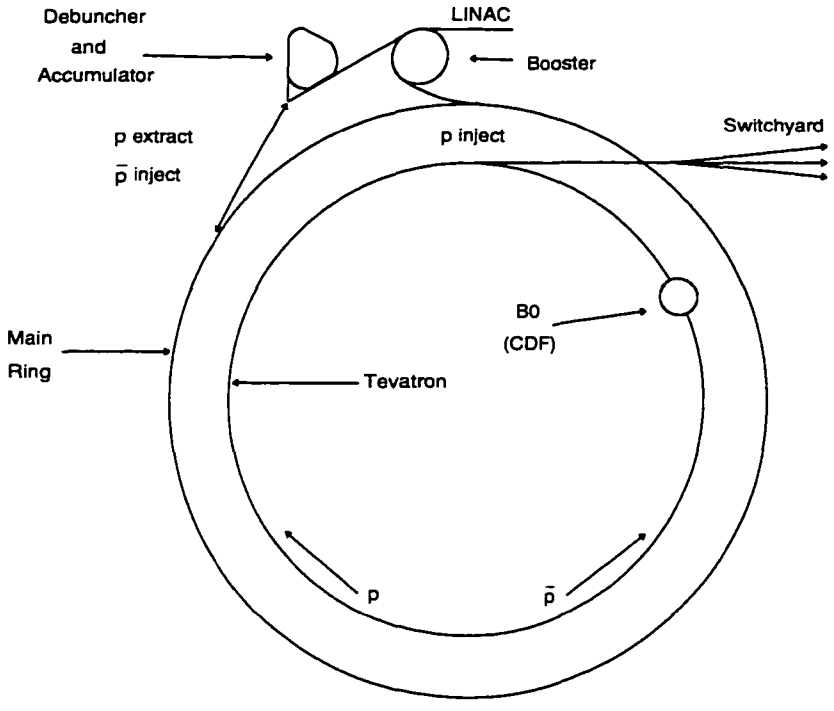

Figure 3-1: The accelerators and related devices used to deliver protons and antiprotons to the CDF Experiment.

At Fermilab, antiprotons are produced by striking a tungsten target with protons extracted from the Main Ring. From the resulting spray of particles, antiprotons are extracted and focused using a lithium electromagnet. These antiprotons are then collected by the Debuncher which reduces their spread in in longitudinal momentum in order to facilitate their eventual injection to the Main Ring. The antiprotons are then ejected from the Debuncher and stacked in the Antiproton Accumulator.

During the Tevatron's Run 1A in 1992, protons would be accelerated to 150 GeV by the Main Ring, and then injected in 6 bunches to the Tevatron. Then antiprotons would be delivered to the Main Ring by the Accumulator and accelerated to 150 GeV, and then injected into the Tevatron also in 6 bunches. Then the protons and antiprotons were simultaneously accelerated to 900 GeV, and Tevatron quadrupoles were turned on to focus the beams at the B0 interaction point, at the center of the CDF Detector.

A typical Run 1A Tevatron store at CDF started with a luminosity of $5 \times 10^{30}\text{cm}^{-2}\text{s}^{-1}$ and lasted about 10 hours. The mean instantaneous luminosity for all of Run 1A was about $3 \times 10^{30}\text{cm}^{-2}\text{s}^{-1}$, and the total integrated luminosity collected during Run 1A, corrected for experimental down time due to detectors critical to this analysis, was 13.2pb^{-1}.

3.2 The CDF Detector

The Collider Detector at Fermilab (CDF) is a particle physics detector used to measure the properties of particles originating from the B0 interaction region at the Tevatron. At B0, the protons enter from the West and antiprotons enter from the East, and the CDF coordinate system defined the proton beam as the positive z axis. The positive y axis is defined as to be vertical and the positive x axis is defined to be pointed away from the center of the Tevatron. Polar coordinates are defined so that the azimuthal angle ϕ is zero along the the positive x axis and increased under a counter-clockwise rotation about the z axis. The polar angle θ was defined as zero relative to the positive z axis. Details of the CDF detector can be found in [19].

Figures 3-2 and 3-3 display the geometry of the subsystems of the CDF Detector. These subsystems were designed, where possible, to lay in a cylindrical fashion about the B0 interaction region. The $p\bar{p}$ collisions were found to be distributed in z about the center of the detector with a width of approximately 30 cm. Viewed from the

nominal collision point, particles in the central region ($|\eta| < 1$) should interact with the beam pipe, a set of time projection chambers (the VTPC), and a wire drift chamber (the CTC). Outside the CTC was a solenoidal magnet field, which provided a 1.41 T field in the z direction. After this solenoidal field, were electromagnetic and hadronic calorimetry and muon chambers, as described in the following sections.

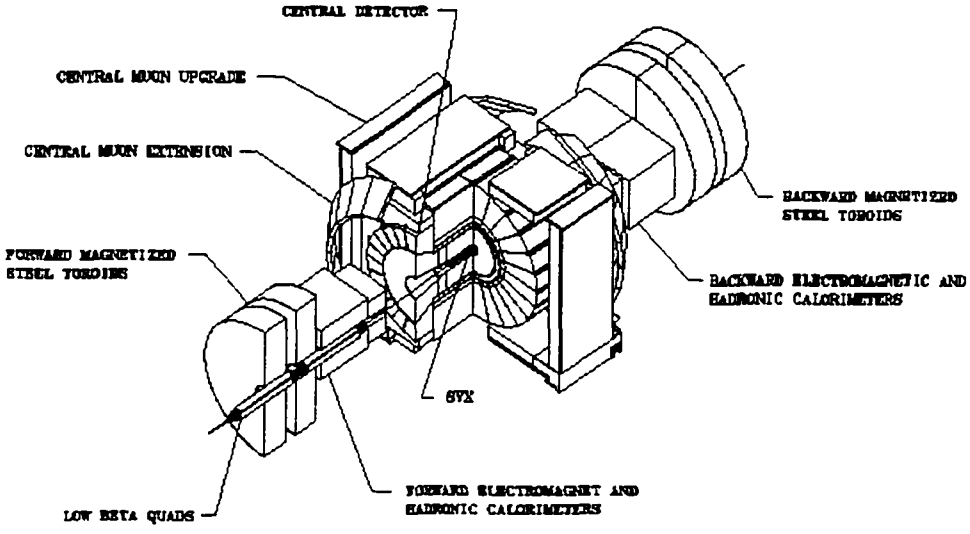

Figure 3-2: A three dimensional perspective of CDF displaying the pertinent muon subsystems.

3.2.1 Vertex Time Projection Chamber

The Vertex Time Projection Chamber (VTPC) is an inner tracking chamber designed to precisely locate charged particles in the $r - z$ plane close to the interaction region [19]. This data is used to determine the location of a given event's interaction point along the z axis - a variable commonly referred to as the "z-vertex" for the event.

The VTPC is a set of 8 individual time projection chambers. Charged particles travelling through the chambers ionize a 50-50 mixture of Argon and Ethane, and the associated electrons and ions drift towards wires and cathode pads, respectively, from

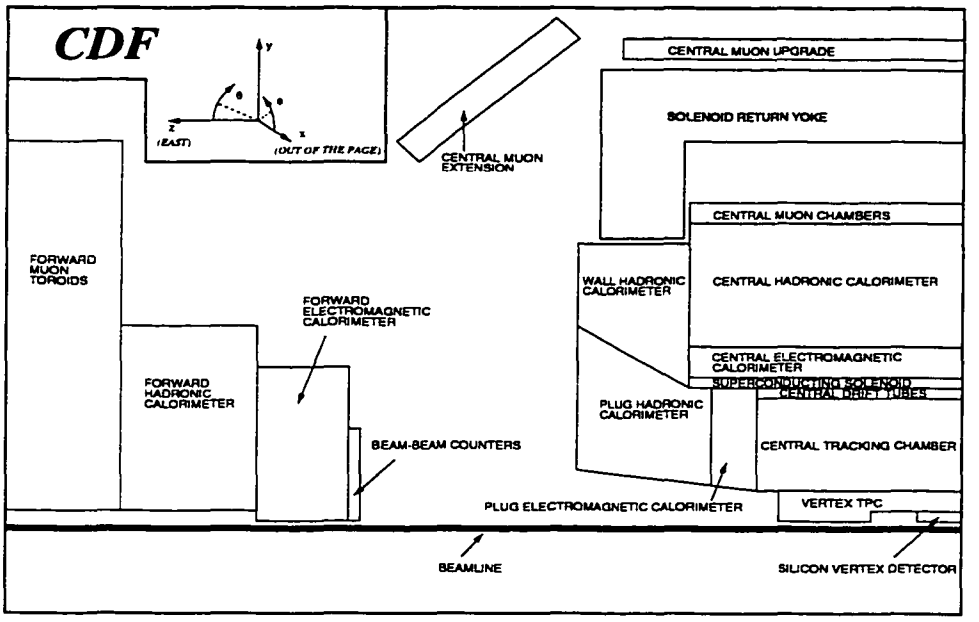

Figure 3-3: A lateral perspective of CDF displaying the relevant muon systems and calorimeter.

which signals are read out. Each individual chamber is subdivided into azimuthal octants. Reconstruction of tracks in the $r - z$ plane is accomplished from precise knowledge of the location of each wire together with the drift time of charge to that wire.

Reconstructed VTPC tracks are parameterized in terms of the polar angle θ and the intercept with the z axis. Primary vertices are determined by identifying clusters of z intercepts from several tracks, and from this information the z vertex of the event is measured. The VTPC resolution for finding a z vertex is about 2 mm, while a gaussian fit to the z vertex distribution yields σ of about 30 cm, thus justifying our event-by-event vertexing.

3.2.2 Central Tracking Chamber

The Central Tracking Chamber (CTC) is a drift chamber which is used to measure the tracks of charged particles in 3 dimensions [19]. The chamber covers the region $|\eta| < 1$ at its outer radius and is cylindrically symmetric, thus allowing full azimuthal coverage. The CTC includes 9 alternating axial and stereo superlayers, where the 5 axial superlayers consist of wires parallel to the z axis, and the 4 stereo superlayers consist of wires with a 3° tilt which provides z information. Within each superlayer the wires are subdivided into cells, and the superlayer structure of the CTC at its endplate is shown in Figure 3-4. The entire CTC is contained within a solenoidal magnetic field, which allows the measurement of the P_T of charged particles.

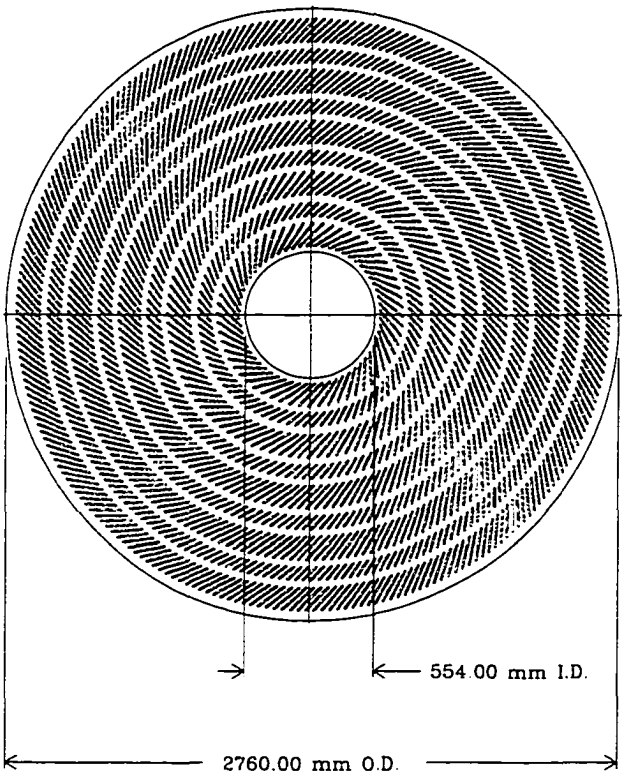

Figure 3-4: The wire layout at the endplate of the Central Tracking Chamber.

Each cell within a superlayer contains field wires, sense wires, potential wires, guard wires and shaper wires. The field wires provide an electrostatic potential of about 1350 V/cm. Charged particles leave ionization trails through the 50-50 Argon Ethane mix used in the chamber, and the resulting electrons drift through the electrostatic and magnetic fields towards the sense wires. The potential wires are used to control the gas gain in the region near the sense wires, while the guard and shaper wires are used to fine–tune the electric field.

Each axial superlayer has twelve sense wires, and each stereo superlayer has six sense wires. The wire planes within a cell are rotated by 45° relative to the radial direction, where the 45° was chosen to ensure that the drift trajectories are approximately azimuthal. This feature ensures that every stiff track crosses each superlayer such that the drift time to at least one wire in the superlayer was less than 40 nsec.

The process of finding tracks in the CTC consisted of three steps, all of which were achieved offline. In the first step, a list of hits and associated drift times was established. Next, a pattern recognition algorithm was applied to attempt to associate hits with a single track. The result of the pattern recognition algorithm was a list of tracks and associated hits, in which individual hits were allowed to be associated with multiple tracks.

The final step was to fit the hits of each track to a helix. This helix is then described by 5 parameters, namely

- z_0 - The z position at the point of closest approach of the helix to the origin.
- d_0 - The distance of closest approach to the origin in the $x - y$ plane.
- ϕ_0 - The azimuthal angle relative to the positive x axis at the point of closest approach to the origin.
- c - The half-radius of curvature of the reconstructed track.
- $\cot\theta$ - The cotangent of the polar angle at the point of closest approach to the origin.

Several different types of track fits are performed on CDF data, including:

- **Unconstrained** - In this type of fit, the only information used is that provided by the hits themselves. This includes the location of the hits and their residuals relative to the fit. The latter were incorporated by performing the fits in an iterative fashion and weighting the hits by the inverse of the residuals.

- **Beam Constrained** - This type of fit constrained the tracks to originate in the $x - y$ plane at the same point as the beam axis.

- **Vertex Constrained** - This type of fit constrained a set of tracks to originate from a common vertex, either in the $x - y$ plane or in all 3 dimensions.

The performance of the CTC has been studied using both cosmic ray data and $p\bar{p}$ data. From the cosmic ray data it has been determined that the spatial resolution of the sense wires is approximately 155 μ and that the P_T resolution of the detector is approximately $\frac{\sigma}{P_T} = 0.002 P_T$. Of course, the track recontruction efficiency is different in cosmic ray data than in $p\bar{p}$ data, since $p\bar{p}$ data has, on average, many more tracks per event. For this reason a study was conducted merging the CTC hits from Monte Carlo pion and kaon simulations with real CDF $p\bar{p}$ data. From this study the track reconstruction efficiency for tracks reaching the radial edge of the chamber was found to be $99\% \pm 0.2\%$ [20].

3.2.3 Calorimetry

CDF has both electromagnetic and hadronic sampling calorimetry covering almost 4π steradians of solid angle [19]. The calorimetry in the central region is divided into four arches, each covering 180° in ϕ. Two arches on the East end of CDF cover $0 < \eta < 1.1$ while those on the West end cover $-1.1 < \eta < 0$. Each arch is composed of twelve wedges, each of which subtends 15° in ϕ . Each wedge is subdivided into towers, each subtending 0.1 units of η. In the central region the electromagnetic

calorimeter (CEM) consists of alternating sheets of lead and scintillator, and light originating in the scintillator is directed to photomultipliers via light pipes, as shown in Figure 3-5. Displayed in Figure 3-6 is a map of a 12 parameter fit to the CEM response as measured by both cosmic ray data and electron test beam data. The CEM has a resolution of $\sigma_E/E = 13.5\%/\sqrt{E}$. The central hadronic calorimeter is constructed in a similar fashion, but uses sheets of steel and scintillator, and has a resolution of $\sigma_E/E = 70\%/\sqrt{E}$.

3.2.4 Central Strip Chambers

The Central Strip Chambers (CES) are used to determine shower position and tranverse development at shower maximum by measuring the charge deposition on orthogonal strips and wires [19]. The chambers themselves are constructed from copper-backed $\frac{1}{16}$ in. PC boards and 0.002 in. gold-plated tungsten wire, with the copper strips and tungsten wires arranged in a perpendicular geometry as shown in Figure 3-7. The chambers flow a 95-5 mixture of Argon-Ethane, and are operated at 1420 V. The chamber high voltage is chosen to give an occasional (few %) channel saturation for 150 GeV test beam electrons near normal incidence. A study of electron test beam data was conducted in order to assign a χ^2 associated with a shower's transverse profile. This CES χ^2 method is used in this dissertation to distinguish photons from neutral mesons, as discussed in Chapter 4.

3.2.5 Muon Systems

The CDF central muon systems consist of three subsystems - namely the Central Muon System (CMU), the Central Muon Upgrade (CMP), and the Central Muon Extension (CMX). The combined acceptance for these subsystems is complicated by the fact that each subsystem has a different geometry. The CMU has a cylindrical symmetry, the CMP has a box geometry, and the CMX has a conical geometry, as shown in Figures 3-2 and 3-3. The effect of these diverse geometries on the muon

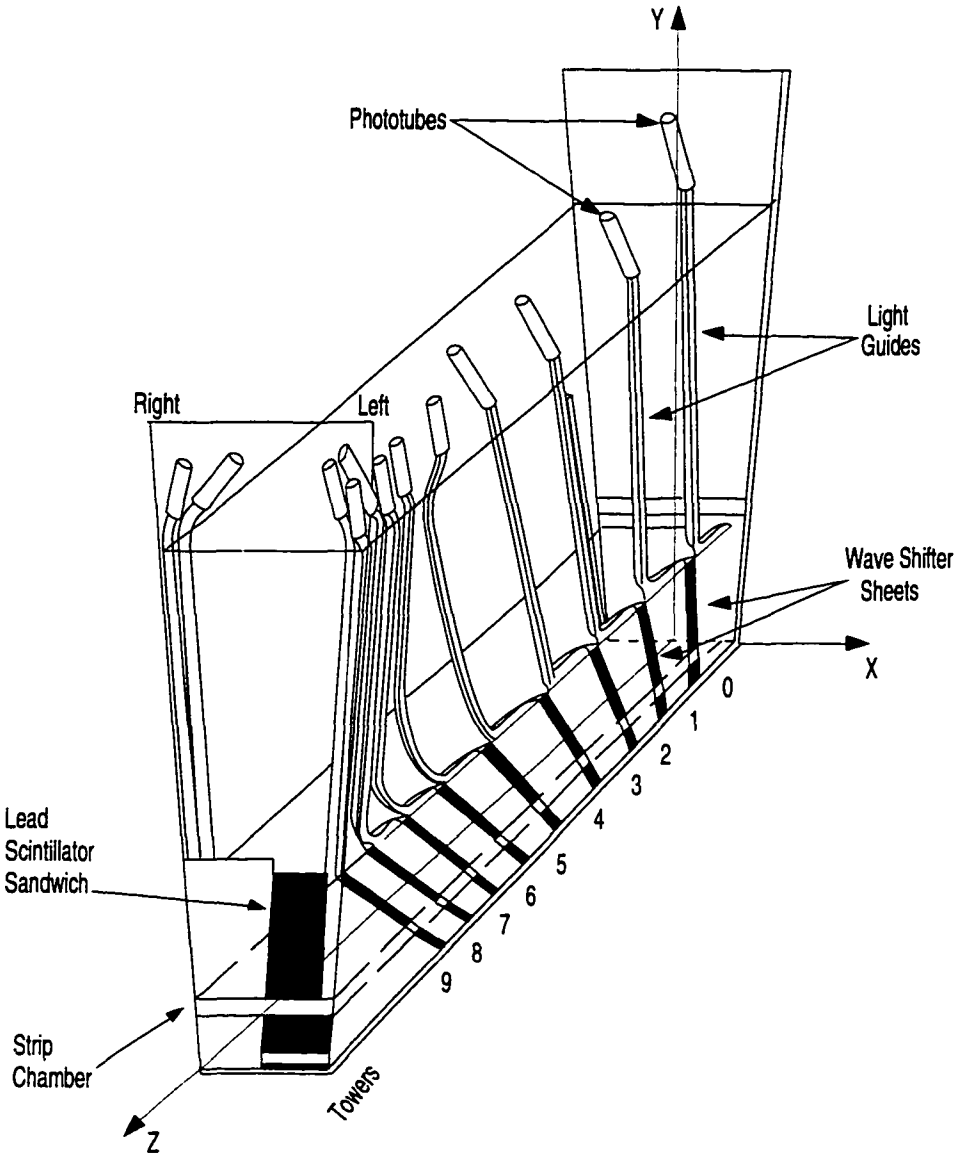

Figure 3-5: Shown above is a 3D perspective of a single wedge of the Central Electromagnetic Calorimeter. Displayed are both the lead–scintillator sandwich of the calorimeter itself, together with the phototube readout, and the position of the shower–max Central Strip chambers.

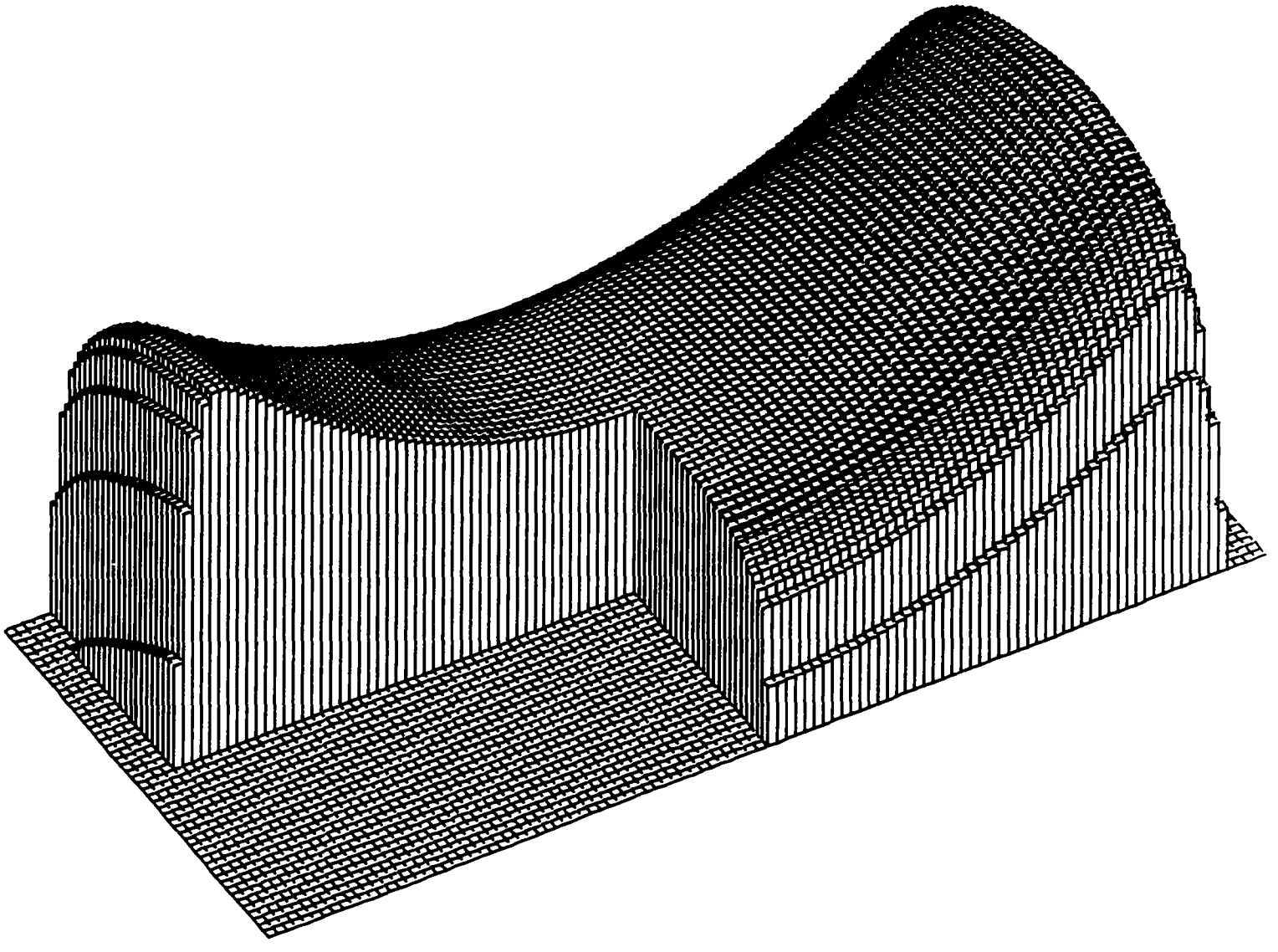

Figure 3-6: Here we display a map of the Central Electro-Magnetic calorimeter response. The vertical axis is a 12 parameter fit to the calorimeter response for minimum ionizing particles, while the horizontal axes are the longitudinal and polar coordinates.

Figure 3-7: Shown above is a schematic description of a CES chamber, displaying the perpendicular cathode and anode construction.

acceptance is shown in Figure 3-8.

Central Muon System

The CMU chambers consist of four layers of drift chambers (Figure 3-10) covering the region $|\eta| < 0.6$, as shown in Figure 3-9 [19]. The drift chamber wires are parallel to the z axis and alternate layers are radially aligned in order to allow a crude momentum measurement. The chambers are subdivided into 24 wedges in ϕ for each half of the detector ($-0.6 < \eta < 0$ and $0 < \eta < 0.6$). Each wedge is further subdivided into three 5° towers, with each tower having the geometry shown in Figure 3-11. Wires in alternating layers were offset by 2 mm in order to resolve the left-right ambiguity.

Muon tracks in the CMU are reconstructed using time-to-distance relationships in the drift direction (ϕ), and charge division in the longitudinal direction (z). Cosmic ray studies have determined the resolutions to be 250 μm in the drift direction and 1.2 mm in the longitudinal direction. Clusters of hits in at least three layers are found separately in the $r - \phi$ and $r - z$ planes, and these two sets of clusters are merged. Then, a linear fit is performed to generate a three dimensional track segment.

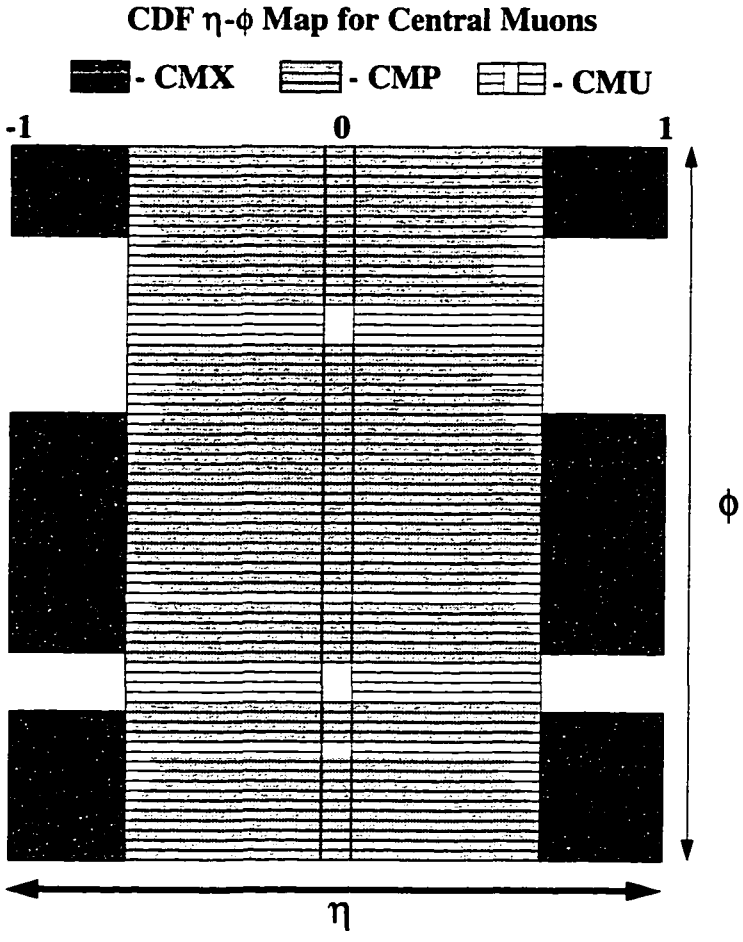

Figure 3-8: An $\eta - \phi$ plot of the central muon coverage at CDF. Note the effect of the CMP's box geometry on its acceptance, and the gaps in the CMX acceptance at the top and bottom of the detector.

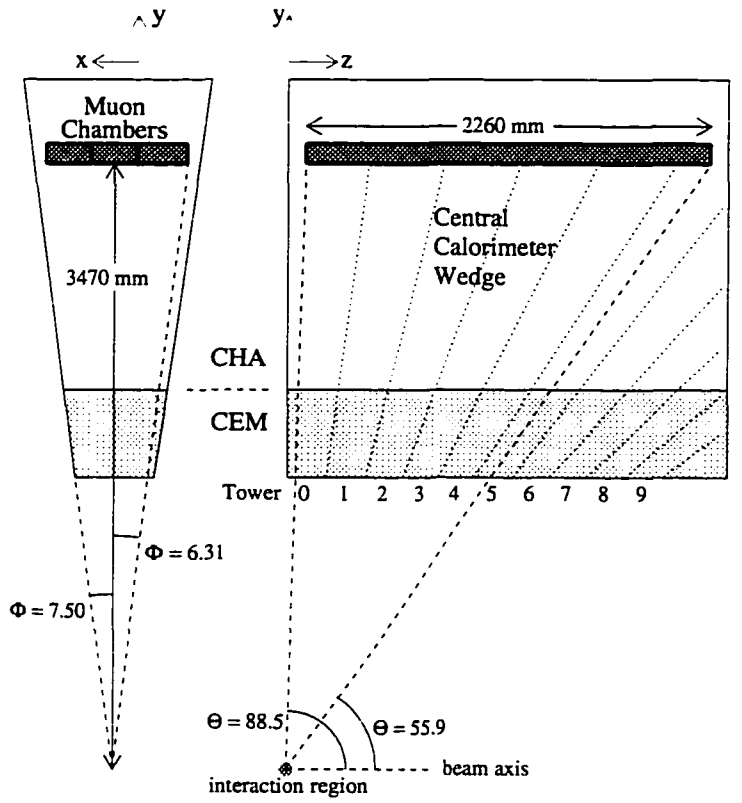

Figure 3-9: Here we display the organization of drift chambers of the CMU, in both η and ϕ space, superimposed on the structure of the CEM.

Figure 3-11: Above we display the geometry of the 16 chambers of a single CMU tower.

The CMU, operating as an independent muon detector, suffers from two serious defects. The first is that the CMU has an average of only 5.4 pion interaction lengths between it and the event vertex. This results in very high backgrounds due to mesons punching through the calorimetry and leaving a stub in the CMU. The CMP was constructed to address this flaw, and Figure 3-12 shows the CHA energy deposition for CMU only muons compared to CMU-CMP coincidence muons, demonstrating the noise reduction accomplished by requiring CMU-CMP coincidence. The number of interaction lengths presented to each of the muon subsystems is displayed in Figure 3-13. The second defect is that the CMU only covers a range of $-0.6 < \eta < 0.6$. The CMX was constructed in order to expand the muon coverage to $-1.0 < \eta < 1.0$.

Central Muon Upgrade

The CMP also consists of four layers of drift cells, but in a staggered geometry. The chambers are assembled in a box geometry outside the solenoid magnet, and behind 60 cm of additional steel in the region $55° \leq \theta \leq 90°$. The return yoke of the CDF solenoid provides the necessary steel above and below the central detector, and as a result it was only necessary to add steel on the two sides of the detector in the form of non-magnetized retractible walls. The CMP chambers, like the CMX chambers, are 2.5 cm $\times$ 15 cm in cross section, and are operated in proportional mode with a maximum drift time of approximately 1.4 μs. The design of a CMP/CMX chamber is shown in Figure 3-14.

The η coverage of the CMP roughly corresponds to that of the CMU, except where limited by the box geometry, as displayed in Figure 3-8. The additional interaction lengths in front of the CMP allow one to dramatically reduce the central muon backgrounds by requiring a CMU-CMP coincidence. The reduction of acceptance is more than compensated by the reduction in background. The Level 2 muon trigger rates for CMU only and CMU-CMP coincidence muon candidates are shown in Figure 3-15.

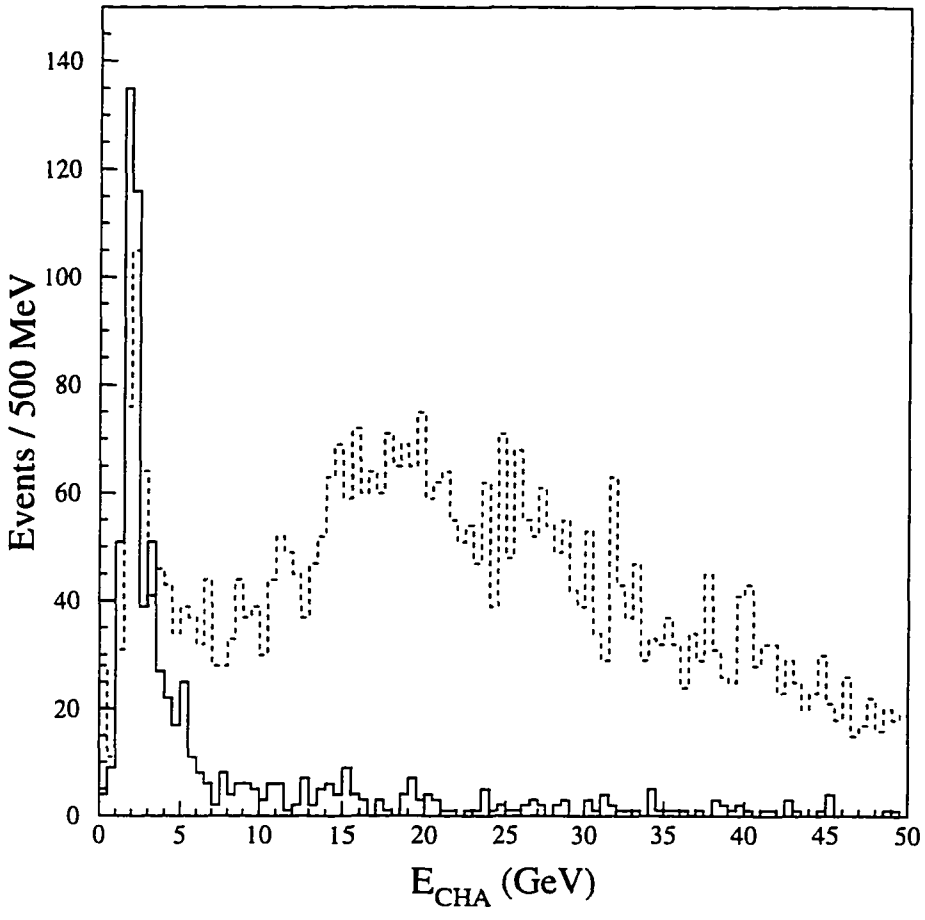

Figure 3-12: The effect of the CMP at reducing hadronic punch-through is demonstrated by the distribution of energy observed in the CHA towers traversed by muon candidates with $P_T > 15$GeV observed with CMU only stubs (dashed) and with CMU-CMP coincidence (solid). Note the strong minimum-ionizing particle peak observed for the CMU-CMP coincidence candidates.

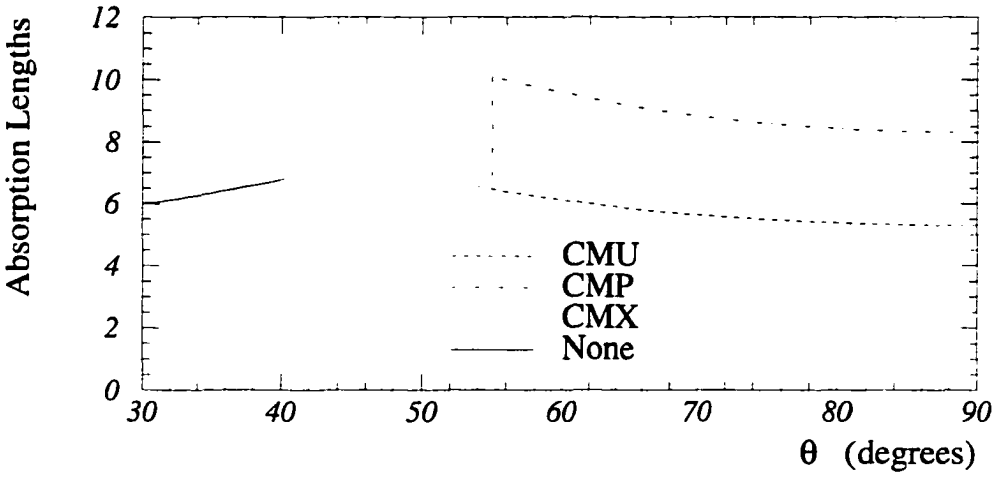

Figure 3-13: The number of interaction lengths of matter traversed by a particle en route to each of the muon detectors, as a function of the polar angle θ.

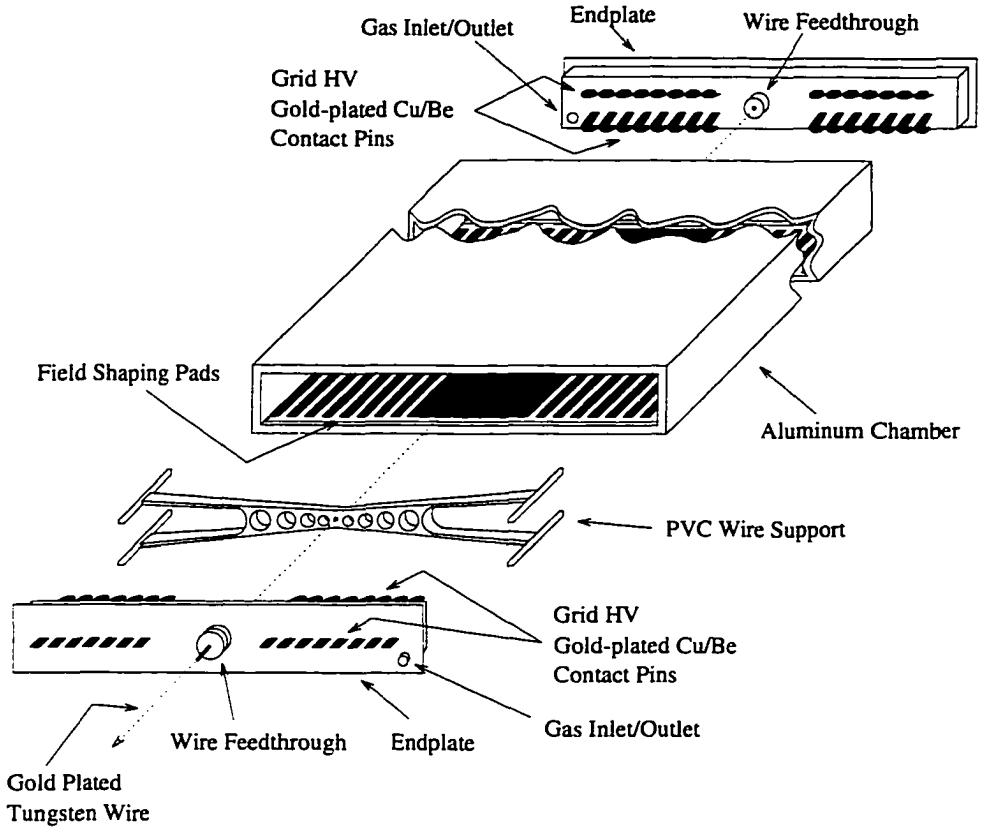

Figure 3-14: Here we show the mechanical layout of a drift chamber for the CMP or CMX.

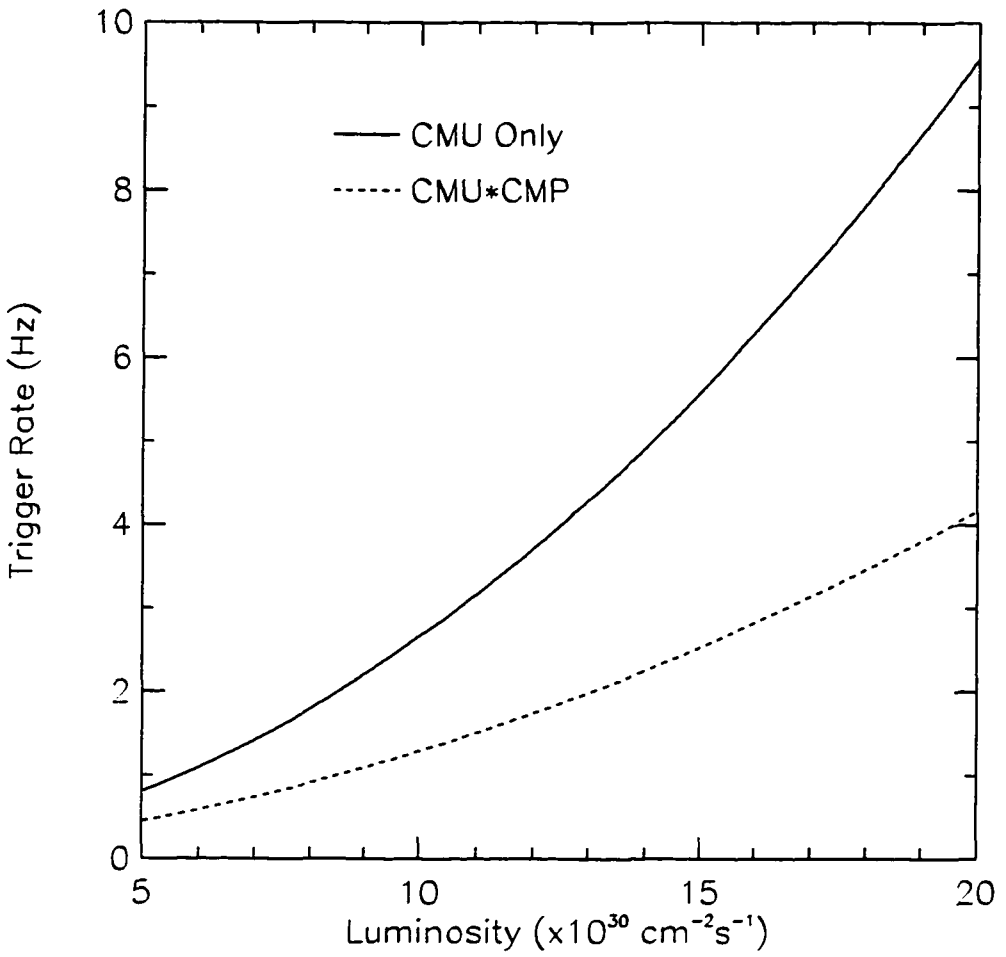

Figure 3-15: Level 2 muon trigger rates from the 1995 run for CMU only and CMU-CMP coincidence muon candidates with a 12 GeV threshold.

Central Muon Extension

The CMX consists of conical sections of four layers of drift tubes at each end of the CDF detector covering a pseudorapidity range of $0.65 < |\eta| < 1.0$. The drift tube layout for a 15° wedge of the CMX is shown in Figure 3-16. There is a 30° gap in ϕ at the top of the detector for the Tevatron Main Ring, and there's a 90° gap at the bottom, where the conical sections are interrupted by the floor of the collision hall. Both of these gaps are visible in Figure 3-8.The four layers of drift tubes are arranged into groups of twelve for each 15° ϕ sector, and successive layers are half-cell offset to eliminate ambiguities. No additional steel was added for this detector, since the large angle through the hadron calorimeter and magnet yoke means that particles reaching the CMX traverse more interaction lengths than those projecting to the CMU, as shown in Figure 3-13.

Figure 3-16: Above is displayed the geometry of the drift tube layout for a 15° CMX wedge.

There is an additional background found in the CMX that is not found in the CMU/CMP, which is due to secondary particles generated from far forward particles scattering off the beam pipe. This is addressed in Section 4.6.1.

3.3 The CDF Data Aquisition System

One of the greatest challenges in experimental $p\bar{p}$ collider physics is the enormous total cross section for $p\bar{p}$ interactions. The bulk of these interactions consist of elastic small angle scattering, so, in a high luminosity environment (like that at CDF), high P_T physics can only be studied by means of a complicated trigger system designed to extract the interesting physics from the chaff of elastic scattering. The CDF trigger system is designed in three levels, each level making a more sophisticated decision based on more detailed information, while each level consequently takes more time to reach its decision. Here we will give a general overview of the CDF trigger system, while in Section 3.4 we will discuss the details of the photon trigger pertinent to this dissertation.

3.3.1 Level 1

The Level 1 trigger is designed to make a trigger decision between successive 3.5 μ sec beam crossings in order to incur no dead time to the system. The Level 1 trigger system consists of three components:

- Coincidence hits in the East and West Beam-Beam Counters;
- Single calorimeter towers over transverse energy threshold; and
- Muon chamber track stubs over transverse momentum threshold.

A coincidence in at least one of the BBC scintillators on both sides of the CDF detector forms the minimum bias trigger used for background studies at CDF.

The Level 1 calorimeter trigger pertinent to this thesis is generated by analog signals coming from the central scintillator phototubes. The trigger is segmented in the η-ϕ plane by $\Delta\phi = 15°$ and $\Delta\eta = 0.2$, while the actual segmentation provided by the calorimeter is reduced by fast analog signal summation in order to reduce the absolute trigger rate. The analog calorimeter signals are corrected for pedestal offsets and gain variations. The tower signals are also weighted by sin θ, where θ is the polar angle, so that trigger thresholds can be set on transverse energy.

3.3.2 Level 2

After the receipt of a Level 1 accept, the beam crossing clock is inhibited from clearing the detector signals, and all detector signal gates are held while the Level 2 trigger system makes its decision. At Level 2, the following, more detailed information is available for the trigger system:

- Fast CTC track pattern recognition (CFT);
- Hadronic and electromagnetic calorimetry clustering;
- Matching CFT tracks to muon stubs;
- Matching CFT tracks to calorimeter clusters; and
- Global energy sums (total, transverse, missing transverse).

The Central Fast Tracker (CFT) makes use of fast hit information from the five axial superlayers. Using this information, the transverse momentum of individual tracks is measured with a resolution of $\delta P_T / P_T^2 \sim 3.5\%$. The CFT then generates a list of tracks in eight P_T bins with nominal central values of 3.3,4.0,5.0,6.5,10.0,15.0,20.0, and 30.0 GeV. This list of tracks is then matched to Level 2 muon hits and calorimetry clusters.

The Level 2 trigger system also performs calorimeter clustering. Two sets of thresholds are applied to all calorimeter trigger towers, seed and shoulder. When a

trigger tower is found passing the seed threshold, then the eight adjacent towers are checked to see if they pass either the seed or shoulder threshold - and if a tower does pass, it is added to the cluster. This process is repeated until all new adjacent towers have been rejected. Once the clusters have been identified, quantities like E_x, E_y, E_T, η, and ϕ are calculated for each cluster.

3.3.3 Level 3

On the receipt of Level 2 accept, all channels of the CDF detector are digitized and sent to the Level 3 trigger system, which takes typically 2 - 3 $m$sec. The Level 3 trigger system consists of 48 Silicon Graphics computers, each containing two event buffers. With each event being sent to a single buffer, the Level 3 system can process 48 separate events in parallel, while another 48 events are being loaded into the secondary buffers. Level 3 processing allows roughly 1-2 seconds.

At Level 3, all of the quantities in the offline data are available to make trigger decisions. At this point a wide variety of triggers and data streams are defined in order to facilitate the analysis of the CDF data. In the next section we limit ourselves to the trigger pertinent to this thesis.

3.4 The CDF Run 1A Photon Trigger

As described in Section 3.3, the CDF photon trigger has three levels [21]. At Level 1 a single CEM tower is required to be above a threshold of 6 GeV. The Level 2 trigger requires that 89% of the cluster's transverse energy be in the the EM compartment of the calorimeter, and that the cluster be *isolated* as determined by neural net based isolation boards. These isolation boards require that at Level 2 the transverse energy in the 5×5 grid of towers surrounding the candidate cluster (equivalent to a radius of $R = \sqrt{(\Delta\eta)^2 + (\Delta\phi)^2} = 0.65$) is less than 5 GeV. For the data analyzed in this thesis, a transverse energy threshold of 16 GeV is also applied at the Level 2. Without this

Level 2 isolation requirement, a prescale of approximately 100 would be required for the 16-30 GeV range, due to trigger rate limitations. At Level 3, software algorithms apply fiducial cuts to the photon candidates and the isolation cut is stiffened to 4 GeV in a cone of radius 0.7.

Chapter 4

Analysis

In this chapter we discuss the analysis of the Run 1A photon-muon data sample. In the first section we describe the initial event selection and the loose muon cuts used to assemble a dataset of photon triggered events which also have muon candidates, and also the more stringent cuts applied to reject backgrounds in the photon and the muon legs. In Sections 4.2 and 4.3 we describe the photon trigger efficiency and acceptance and the various photon background estimate methods that we have studied. Section 4.4 describes, motivates, and studies the matching variables that we have found useful for CMX muons, while Section 4.5 describes the reconstruction efficiency and acceptance for muons at the CDF detector. In Section 4.6 we discuss and compare our various methods of estimating the muon backgrounds in our sample, and in Section 4.7 we introduce a variable that allows us to descriminate between muons resulting from the semi-leptonic decays of charm and bottom quarks. Finally, after this discussion of the event rates, the efficiencies and acceptances, and the background rates, we discuss the systematic errors, our measurement of the photon-muon cross section, and our comparison of our result with both the PYTHIA Monte Carlo prediction and a NLO calculation.

4.1 Event Selection

The data analyzed in this thesis was collected during the 1992-1993 Fermilab Tevatron Run 1A. The only trigger requirement placed on the data was that the events pass the 16 GeV isolated photon trigger. This trigger, as discussed in Section 3.4, required that the event have a Level 2 central EM cluster with E_T greater then 16 GeV, that the cluster have no associated CFT track greater than 3.3 GeV pointing at it, and that the cluster satisfy the isolation requirement that there be less than 5 GeV additional transverse energy in a cone of $R = 0.65$ around it. No other trigger requirements were made, and, in particular, no muon trigger requirement was made. Also, runs for which the Level 2 isolated photon trigger was malfunctioning were rejected.

We searched this photon sample for muon candidates reconstructed offline, where a muon candidate is defined as a match between an offline 3D CTC track and an offline muon stub found in any of the CMU, CMP, or CMX muon detectors. For this piece of the analysis we reprocessed the data with Version 7.12 of the CDF offline code in order to incorporate the final Run 1A CMX calibration and alignment constants and the CMX stub finding algorithm described in [25]. Finally, events were rejected when the muon stub was found in a muon system known to be malfunctioning during that run.

In processing the photon data our initial event selection criteria were kept very loose in order that appropriate cross checks and background studies could be performed on the final subset of events selected. We required the photon to pass the standard CDF photon filter - the same filter used for the CDF Run 1A inclusive photon analysis [21] as discussed below. We also required the muon to pass the loose muon cuts described in [27]. These cuts were found to be $98-99\%$ efficient for muons derived from the decay of ψ's:

Photon Requirements:

- Pass the PHO92 filter [21].

The PHO92 filter was designed to identify photon candidates for the CDF Run 1A inclusive photon analysis. It takes as input the EM calorimeter clusters and CES clusters identified by the offline code, and then only accepts as candidates EM clusters found in the central calorimeter that also had an associated CES cluster. It then requires that the associated CES cluster pass fiducial cuts, which ensure the efficiency of photon detection, that there be no other CES cluster greater than 1 GeV, and it makes an isolation cut by requiring that the additional transverse energy found in a cone of $R = 0.7$ around the EM cluster be less than 4 GeV. The cluster is also required to have an offline transverse energy greater than 10 GeV and to have no reconstructed 3D track pointing at it.

The selection of muons in the data set was accomplished by cutting on the various track–stub χ^2s of the muon candidates. These χ^2s refer to the match of the CTC track to the muon chamber stub. The x-direction corresponds to $R-\phi$, where ϕ is the polar angle, while the z-direction corresponds to $R-\theta$ where θ is the azimuthal angle.

Muon Requirements:

- CMU χ^2 in the x-direction < 9;
- CMU χ^2 in the z-direction < 12;
- CMP χ^2 in the x-direction < 9;
- CMX χ^2 in the x-direction < 9; and
- $P_T^{\mu} > 4.0$GeV.

With these cuts we ran on $\sim$ 1.2 million events corresponding to 13.2pb^{-1}, and found 292,112 passing both PHO92 and the routine BADRUN, which removes events corresponding to data runs defined as bad for various CDF subdetectors. Of these events, 11,932 had muon candidates passing the above cuts. These candidates, however, comprise real muons together with various muon backgrounds as discussed below. We note here that although the additional cuts described in this section reduce these backgrounds, it is still necessary to subtract the remaining backgrounds using the techniques discussed in Section 4.6.

In addition to the above selection criteria, we impose a number of cuts which purify the sample and simplify our analysis. We impose upper cuts on the CES χ^2 and the photon E_T. The CES χ^2 is a measure of how well the EM cluster's transverse profile agrees with that of a true photon as determined from test beam data. Thus, an upper cut on this variable rejects the neutral meson backgrounds. The upper cut on the photon E_T is necessary because at high E_T the decay products of *e.g.* a π^0 merge into a single cluster and are thus indistinguishable from a prompt photon. These cuts ensure that the CES weighting routine, which is used to distinguish prompt photons from neutral mesons (as described in Section 4.3) will properly reflect the prompt photon content of the data. We also impose a lower cut on the photon E_T of 17 GeV, which ensures that sufficient statistics are maintained across the photon spectrum that the CES weighting routine operates correctly. For $|\eta_\mu| < 0.6$, charged mesons punching through the calorimetry and leaving a track stub in the CMU are rejected by requiring a CMU-CMP coincidence, where the steel wall in front of the CMP provides enough additional interaction lengths to drastically reduce the chance of punch-through. For $0.6 < |\eta_\mu| < 1.0$ (where meson punch-through is not a problem), the CMX accidental track-stub matches discussed in Section 4.6.1 are rejected by cutting on the variable W discussed in Section 4.4. Finally, additional rejection of neutral mesons mimicking photons is accomplished by placing an isolation cut on the photon, requiring that the extra energy in a cone of R=0.7 be less than 2 GeV.

These cuts are summarized below:

Photon Requirements:

- CES $\chi^2 < 20$;
- $E_T > 17$GeV;
- $E_T < 40$GeV; and
- isolation (R=0.7)$<$ 2GeV.

Muon Requirements:

- CMU-CMP coincidence; and
- $P_T^\mu > 4.0$GeV;

  or
- CMX muon;
- $|W| < 0.09$;
- $|\Delta z| < 33$cm; and
- $P_T^\mu > 4.0$GeV.

As mentioned before, there are additional backgrounds in the CMX not encountered in the CMP. The above CMX cuts are necessary for our method of controlling and estimating these CMX backgrounds, which will be discussed in Section 4.6.1. We note here, however, that in the above cuts the variable Δz is the $\Delta R - \theta$ of the track-stub position match, while the variable W is a linear combination of the Δx and $\Delta\phi$ of the track-stub position match, which is discussed in Section 4.4.

Applying the final photon cuts left 459 events in the Run 1A data. Then, applying the muon cuts left us with 222 events – 135 in the CMP and 87 in the CMX. After our rejection of runs for which the photon trigger was malfinctioning and runs for which the various muon detectors were malfunctioning, we find our data sample corresponds to 13.2pb^{-1} of luminosity.

4.2 CDF Photon Trigger Efficiency and Acceptance

In this section we discuss the product of the acceptance and efficiency for a photon to be detected at CDF. There are two pieces to the acceptance and efficiency estimate necessary for the photon – muon cross section measurement, where by 'acceptance' we mean the geometrical acceptance for a particle in our $\eta - \phi$ fiducial volume, and by 'efficiency' we mean the efficiency for trigger and reconstruction in our P_T fiducial volume. The first is the acceptance and efficiency for the photon, and the second is the acceptance and efficiency for the muon to be reconstructed as either a CMU - CMP coincidence stub or a CMX stub. The former will be discussed here, while the latter will be discussed in Section 4.5.

We note here that, for the data discussed in this dissertation, the photon and muon legs of the analysis must be treated differently, since the data set analyzed here required only a photon trigger. Thus, the acceptance and efficiency of the photon leg requires a correction due to the trigger turn-on curve for the CDF Run 1A isolated photon trigger, while the acceptance and efficiency of the muon leg can be determined from an unbiased data set.

The acceptance and efficiency for the photon we take from the CDF inclusive photon analysis [21]. The no track cut was studied with minimum-bias data and found to be 93% efficient. The CES fiducial cuts were found to cover 64% of the solid angle for $|\eta| < 0.9$ and the requirement that there be no additional CES cluster greater than 1 GeV was studied with electron test beam data, and found to be 90%

efficient. The 2 GeV isolation cut on the photon was studied using minimum-bias data, and found to be 78% efficient. The combination of these numbers yields an overall acceptance and efficiency for photon detection of:

$$A * \epsilon(\gamma) = 0.336 \pm 0.034. \tag{4.1}$$

This is valid for photons in $-0.9 < \eta < 0.9$. One must also consider the efficiency for a 17 GeV or higher photon to fire the 16 GeV neural net isolated photon trigger. This has been studied using prescaled lower E_T electron triggers, and found to be

$$A * \epsilon_{trigger}(\gamma) = 0.92. \tag{4.2}$$

4.3 Photon Background Estimates

Due to the limited statistics of the data sample studied here, we investigated two different approaches to estimating our photon backgrounds - a high statistics method and a low statistics method. The high statistics method discussed in Section 4.3.1 is simple, but suffers from the fact that the weights applied to the events are exclusive of the [0,1] interval (*i.e.* the weight for each event is either less than 0 or greater than 1), and thus statistical fluctuations in the CES χ^2 distribution can result in a negative number of real photon events when the statistics are low. The low statistics method discussed in Section 4.3.2 calculates a probability per event, which is inclusive of the [0,1] interval, and thus the estimated number of real photons is positive definite. This method, however, suffers from being awkward and computing intensive.

In the end, we use only the high statistics method to calculate our final measurement. However, we include here a discussion of the low statistics method as a cross check, and as a reference for future analyses.

4.3.1 High Statistics Case

For the high statistics case we studied the photon background subtraction method used in the CDF Run 1A inclusive photon analysis. In this analysis the separation of real photons from background neutral mesons was accomplished by means of a statistical CES weighting routine, which discriminates photons and neutral mesons on the basis of their transverse shower profile, as discussed below and in [21]. When this routine is used to weight events, and statistics are sufficiently high, one obtains results corresponding to a pure photon sample.

The CES weighting routine uses the efficiencies for photons and neutral mesons to have a CES-measured transverse shower profile χ^2 of less then 4. The efficiency for photons to pass this cut was determined using test beam data for electrons, with the difference between photon showers and electron showers being compensated for by noting that photons shower later in the calorimeter than electrons, and thus the CES occupancy for a photon shower should be lower than that for an electron shower. With this in mind, the calculation of the CES χ^2 allowed the CES occupancy to fluctuate greater than in the electron test beam data. The efficiency for neutral mesons was determined with a Monte Carlo study using a detector simulation package, and the mix of neutral measons (π^0's, η's, ρ's, etc.) was varied to calculate the systematic error, as discussed in Section 4.8.

From these efficiencies, a matrix equation can be constructed relating the number of true photons and neutral mesons to the number of EM clusters with CES χ^2's less than and greater than 4. Inverting this matrix equation allows one to extract the number of true photons from the data, via the relation

$$N_\gamma = \left(\frac{\epsilon - \epsilon_b}{\epsilon_\gamma - \epsilon_b}\right) N, \tag{4.3}$$

where N_γ is the number of photons, N is the number of photon candidates, and ϵ is the fraction of photon candidates passing the cuts, while ϵ_γ and ϵ_b are the corresponding fractions for true photons and neutral mesons. We note here that this calculation

assumes that the pertinent quantities have Gaussian errors, and as a consequence the weight returned is greater than one for clusters with a CES χ^2 less than 4, and less than zero for those with CES a χ^2 greater then 4.

During Run 1A, in addition to the CES a new detector was available to study central photons at CDF. A set of multiwire proportional chambers was installed on the face of the CEM in order to study photon conversions in the CDF solenoid magnet material - the Central Preshower, or CPR. Using the CPR, a statistical background subtraction method directly analogous to that of the CES has been developed. This method, however, is most appropriate for photons with E_T greater then 40 GeV, a kinematic regime where this analysis lacks statistics. In the kinematic regime where the two methods overlap, a very good agreement has been found between both methods of predicting the number of true photons in a given sample of candidates. We show in Figure 4-1 the efficiencies for the identification of both photons and background, for both methods, and in Figure 4-2 we show the ratio of the Profile Method to the Conversion Method, as a function of E_T^{γ}, for the overlap region. The agreement is apparent.

Finally, we note that as mentioned in Section 4.3, the use of the CES weighting technique allows negative fluctuations when the statistics are low. For this reason we have also studied the low statistics technique described below.

4.3.2 Low Statistics Case

In the limit of low statistics, the assumption of Gaussian errors implicit in the previous section becomes questionable. Thus, for the low statistics case, an algorithm was devised which used the same data for photon χ^2 efficiencies as the standard CES weighting routine in order to calculate the number of true photons in a photon-candidate sample. Instead of assuming Gaussian errors, however, our code calculated the maximum log likelihood probability for the number of real photons based on Poisson statistics. This approach ensured by construction that the estimated number of

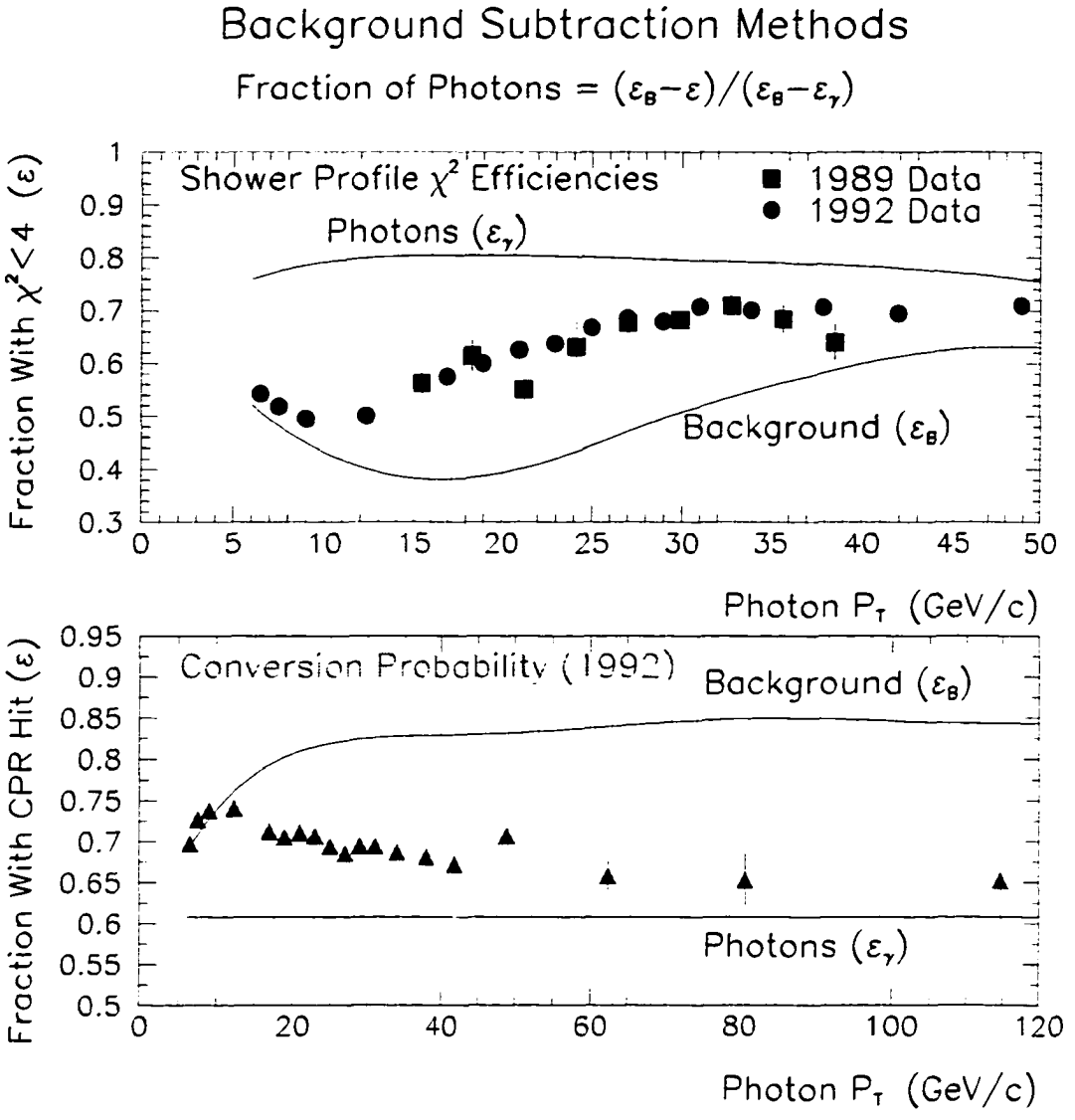

Figure 4-1: The efficiency for the high statistics CES weighting routine to identify a CES cluster as a photon or a neutral meson, as a function of candidate E_T. Displayed are the results for both the CES method (top) and the CPR (bottom).

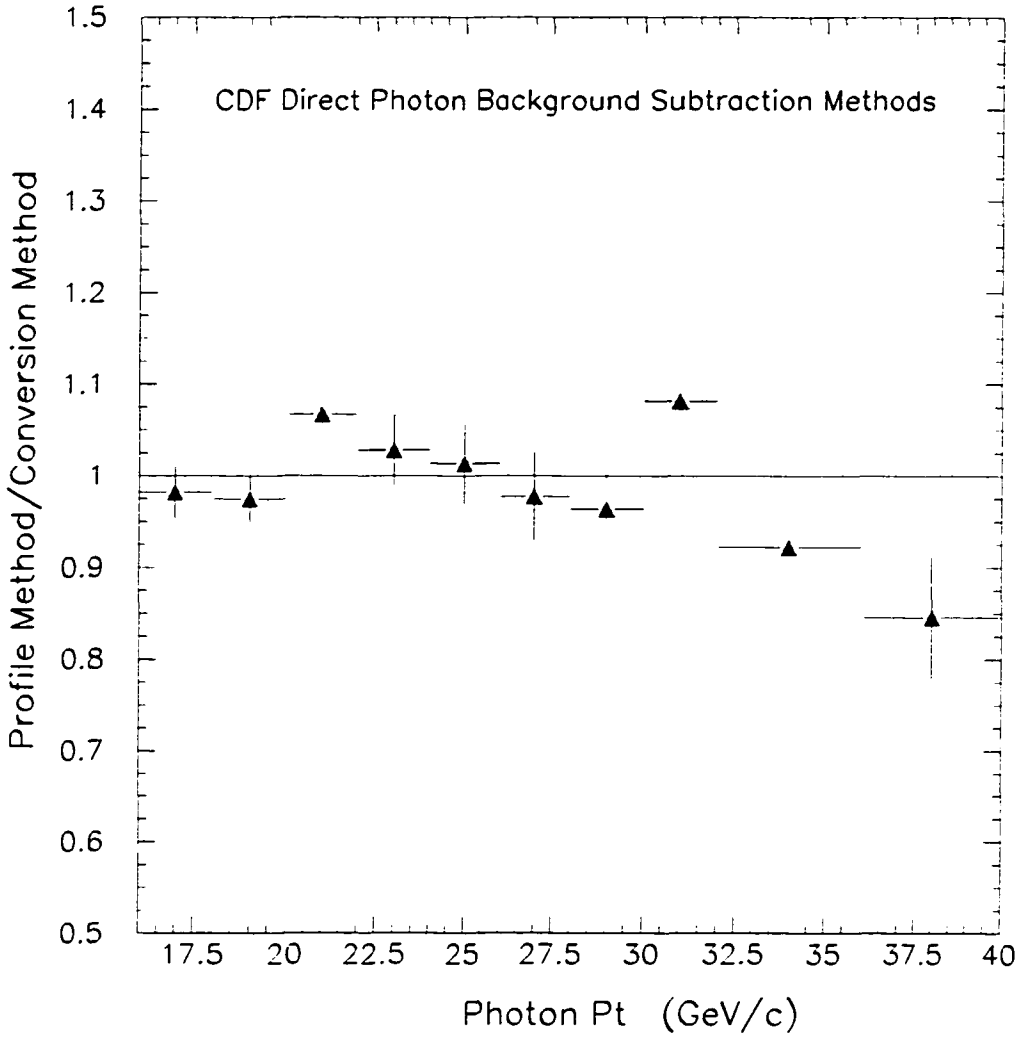

Figure 4-2: The ratio of the photon background subtraction methods, CES over CPR, for photon E_T region in which both apply. It is apparent that there is good agreement between two methods.

true photons was positive definite. Our likelihood calculation is described in some detail in Appendix A, and at this point we merely note that Figure A-1 displays the fractional difference between our likelihood calculation and the standard photon weighting method, as a function of the number of photon candidates. The two methods agree when the statistics are high, and as the statistics decrease, the results of the two methods begin to diverge, as one would expect.

We attempted to use this low statistics method to bin our data in photon E_T, and thus measure the differential cross section. Unfortunately, we found that the statistics of the Run 1A sample were sufficiently limited that statistical fluctuations became large, and the measurement had very large errors. In the end, we restricted ourselves to measuring the integrated cross section using the high statistics method. We include here the details of our low statistics analysis in order to record the method for use in the Run 1B analysis, where with larger integrated luminosity and a dedicated photon-muon trigger with a lower photon trigger threshold ($E_T^\gamma > 10$ GeV), one will have greatly enhanced statistics.

4.4 CMX Muon Variables

Understanding and estimating the additional muon backgrounds found in the CMX requires a careful study of the track-stub matching variables. Here we discuss our detailed study of $\psi \rightarrow \mu\mu$ events, where one muon leg is in the CMX. From this study we have determined the most appropriate variables to cut on in the CMX, the values of cuts to impose, and the efficiencies of these cuts.

As a motivation for including the CMX in this analysis, we first show in Figure 4-3 the pseudorapidity distribution for charm produced from the $\gamma - c$ Compton process as predicted by PYTHIA, with the η acceptance of the CMX and CMU-CMP superimposed. As can be seen, inclusion of the CMX analysis allows the possibility of measuring the η distribution of charm in the process at hand. Future data at CDF

should be able to complete this measurement.

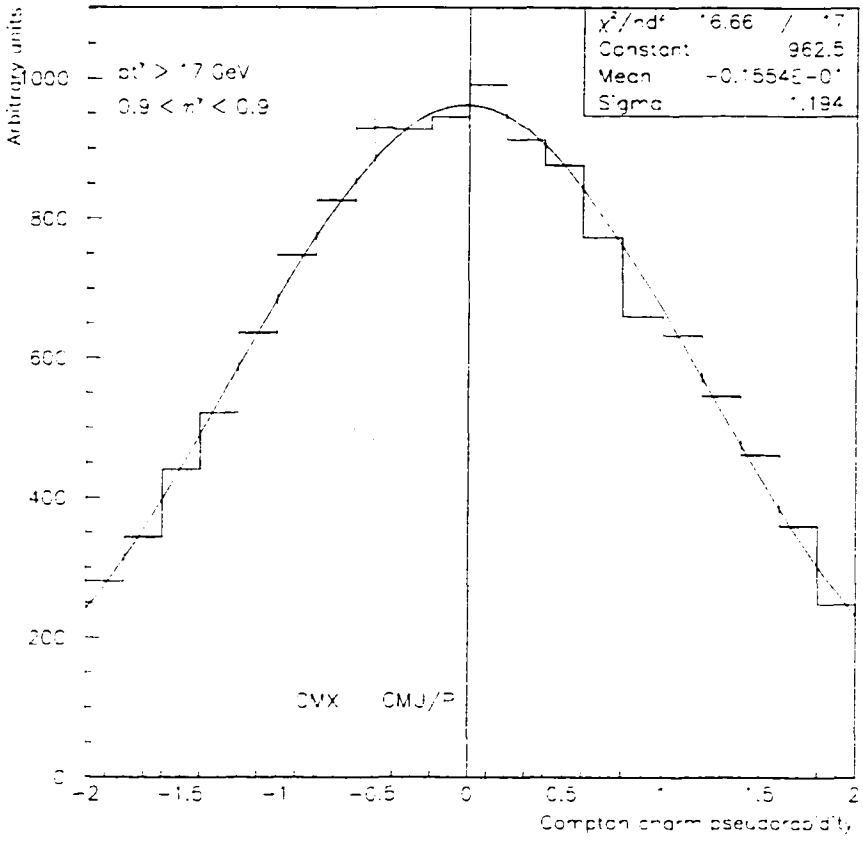

Figure 4-3: PYTHIA prediction of the charm η distribution for the charm Compton process with photons in our fiducial volume, with the approximate CMP and CMX coverage superimposed.

The most useful variables for studying CMX muons are Δx and $\Delta\phi$, where Δx is the CTC track-CMX stub position mismatch and $\Delta\phi$ is the track-stub angle mismatch, both measured in the transverse $R-\phi$ plane. Due to multiple scattering in the calorimeter, the variables Δx and $\Delta\phi$ are correlated. This correlation is due to the fact that a particle that scatters far from its extrapolated position match (Δx) also tends to deviate from its extrapolated angle match ($\Delta\phi$). In Figure 4-4 we display

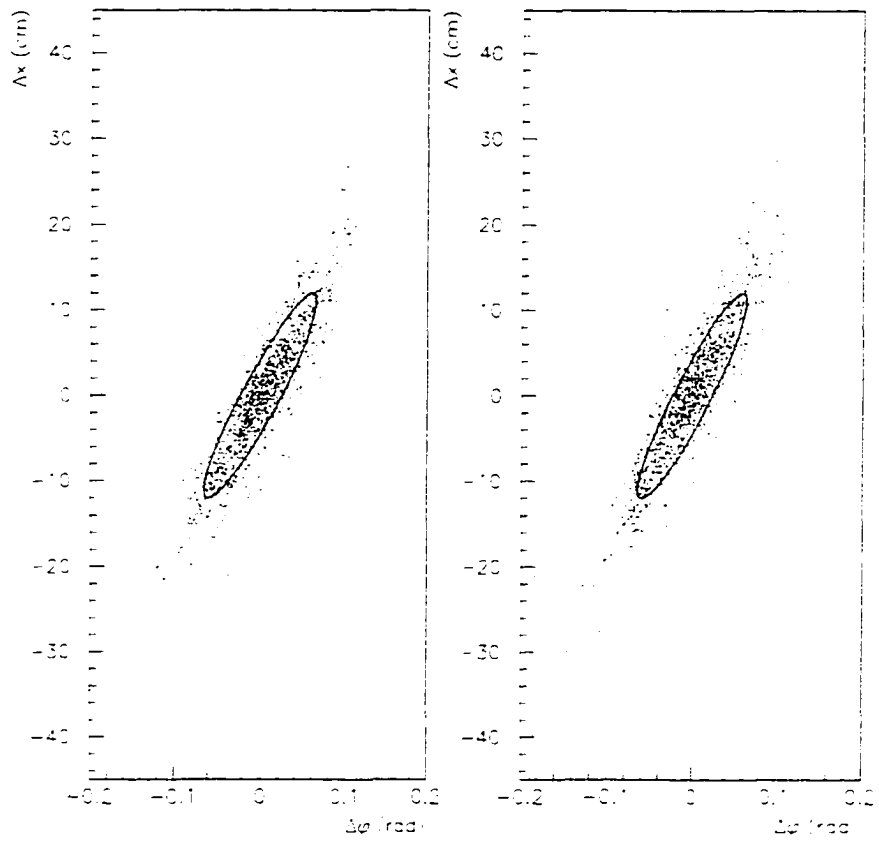

Figure 4-4: Scatter plot of the differences in slope and intercept in the transverse plane for CMX J/ψ decay tracks. The ellipse is the $\chi^2 = 1$ contour for a 2D Gaussian fit to a Monte-Carlo study of multiple scattering in the CDF detector. The left distribution corresponds to positively charged muons, the right plot to negative ones.

the $\chi^2 = 1$ limits from a fit to Monte Carlo data superimposed on scatter plots of the $\psi \rightarrow \mu\mu$ sample discussed below, where the Monte Carlo data is generated using a two-dimensional multiple scattering simulation. If we model the multiple scattering as a single scatter in the calorimeter at a distance ΔR from the CMX detector, the correlation constant between $\Delta\phi$ and Δx is:

$$\Delta x = \Delta R \Delta \phi. \tag{4.4}$$

If one further assumes that the scatter occurs in the middle of the calorimeter, *i.e.*, at $R \sim 2.5$m, and takes the average distance to the CMX, $R \sim 4.5$m, then $\Delta R \sim 200$cm, as shown in Figure 4-5. The fit to Monte Carlo data for multiple scattering displayed in Figure 4-4 yields $\Delta R \sim 250$cm, which is only a reflection of the fact that the conic geometry of the CMX is more complicated than the approximation shown in Figure 4-5.

In order to compensate for the multiple scattering, we define a single variable W

$$W = \Delta\phi - \frac{1}{250\text{cm}}\Delta x(\text{cm}) = \Delta\phi - 0.004\Delta x(\text{cm}), \tag{4.5}$$

where we use the measured average value of ΔR. We require $W < 0.09$, a 3 σ cut if we assume a Gaussian distribution in this variable. We also make a 3 σ cut in Δz, $|\Delta z| < 33$cm. Our CMX background subtraction method is based on the $W - \Delta z$ plane, as will be discussed in Section 4.6.1.

The general characteristics of the Run 1A $\psi \rightarrow \mu\mu$ sample used to study these variables are shown in Figure 4-6. We defined our ψ sample by cutting on the invariant mass region 3.02 GeV $\leq M_{\mu\mu} \leq$ 3.16 GeV, while for background subtraction purposes we used the invariant mass sidebands 2.87(3.24) GeV $\leq M_{\mu\mu} \leq$ 2.94(3.31) GeV. We estimate a signal of 4700 ± 100 events with a background at the 20% level (before any cut in the matching variables). The mean P_T of the muons in this sample is about 4 GeV, and the majority of these muons have six hit stubs as expected from the CMX geometry. 88% of the events correspond to candidates with only one leg in the CMX. We plot the mismatch variables $\Delta\phi$, Δx, $\Delta\theta$, and Δz in Figure 4-7.

$$W = \Delta\phi - 0.004\,\Delta x$$

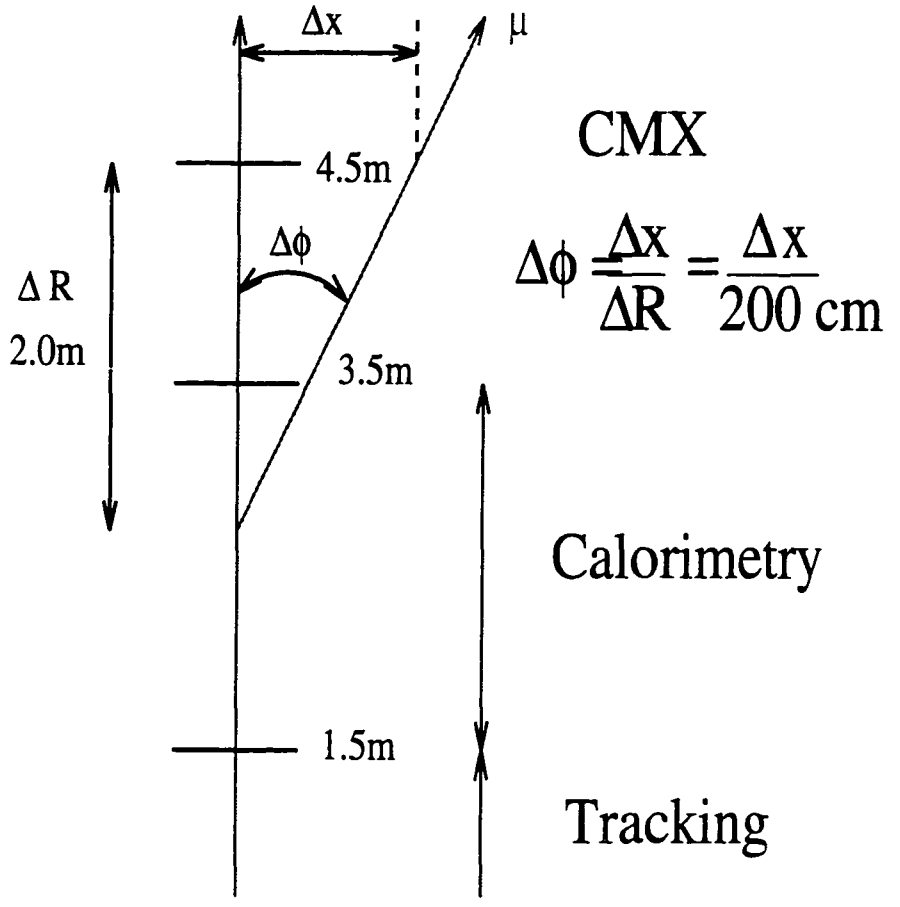

Figure 4-5: This figure displays the geometry of multiple scattering in the calorimetry in front of the CMX, and justifies our definition of the variable W.

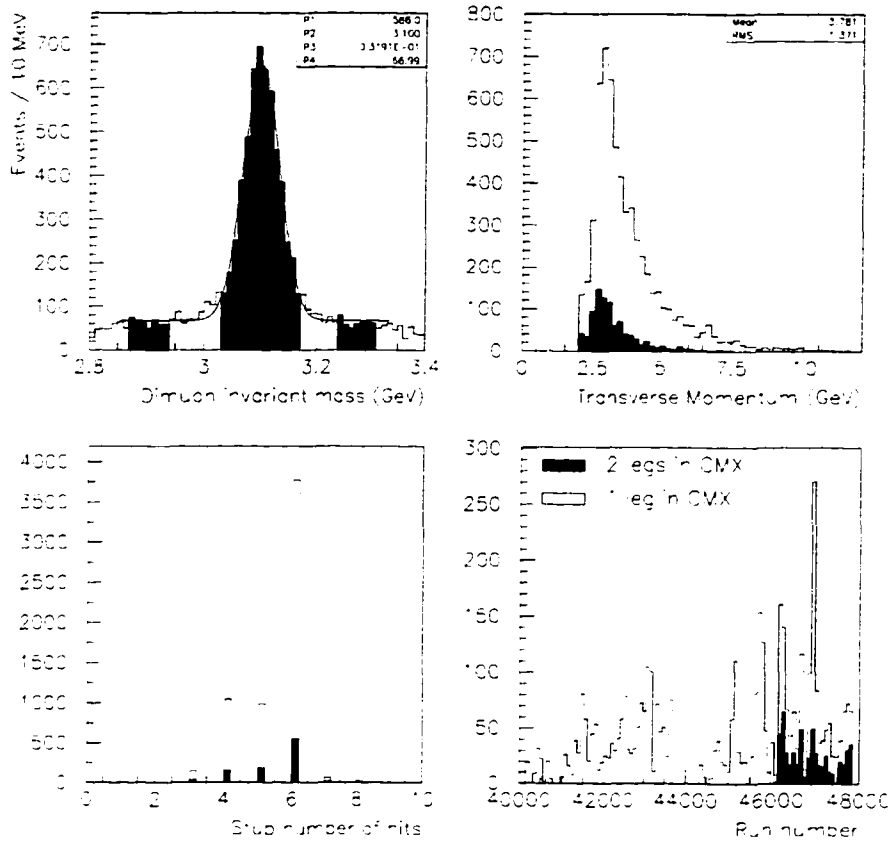

Figure 4-6: Here the general characteristics of the ψ sample are displayed. The mass spectrum is presented with peak and sideband regions marked. The transverse momentum distribution is shown for signal (open) and background (dark) ,and the distribution of the number of stub hits is shown with the estimated background fraction darkened. The number of ψ candidates recorded is shown as a function of run number over the course of Run 1A.

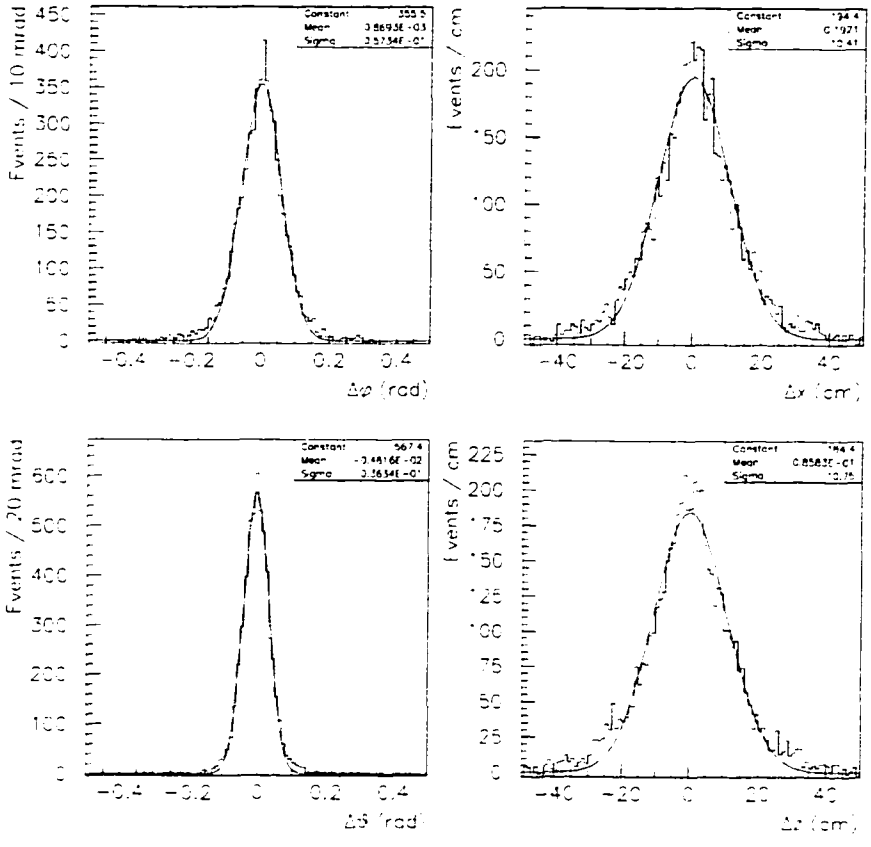

Figure 4-7: The CTC-CMX track-stub mismatch resolution for the ψ sample discussed. The curves are Gaussian fits.

Cutting at $P_T^\mu \geq 4.0$ GeV, we measure the efficiency of the selection cut $\chi_x^2 \leq 9$ to be $99.6 \pm 0.3\%$, where here χ_x^2 refers to the CTC track – CMX stub position match χ^2 in the transverse direction. For $P_T^\mu \geq 4.0$ GeV and $\chi_x^2 \leq 9$, we show the muon mismatch variables in Figure 4-8. The efficiency of requiring $|W| \leq 0.09$ is $98.9 \pm 0.4\%$. $98.4 \pm 0.6\%$ of these events satisfy $|\Delta z| \leq 33$ cm and, finally, $97.9 \pm 0.6\%$ satisfy both cuts.

4.5 CDF Muon Reconstruction Efficiency and Acceptance

The acceptance and efficiency for muon reconstruction in this analysis are complicated by the fact that muon candidates satisfy fiducial requirements in the CMU, CMP, and CMX. As discussed in Chapter 3, these detectors respect a cylindrical, box, and conical geometry respectively. The geometrical acceptance alone for these various detectors defies any simple analytic estimate, so a more sophisticated method was necessary.

We used a Monte Carlo technique to measure the CDF muon reconstruction efficiency and acceptance. We took the measured charged particle spectrum from an inclusive photon sample of known luminosity, and simulated every track as muon using the CDF detector simulation package CDFSIM, both for the CMU/CMP and the CMX.

We determined the acceptance times efficiency for a muon with $P_T^\mu > 4$ GeV and $|\eta| < 0.6$ to be reconstructed as a CMU - CMP coincidence to be

$$A * \epsilon(\mu)_{CMP} = 0.56 \pm 0.01. \tag{4.6}$$

For comparison, we note that that the purely geometrical acceptance for the CMP has been estimated in [40] and [41]. They determine the acceptance of the CMP relative to the CMU is 87% in η and 72% in ϕ. These acceptances, combined with the 84%

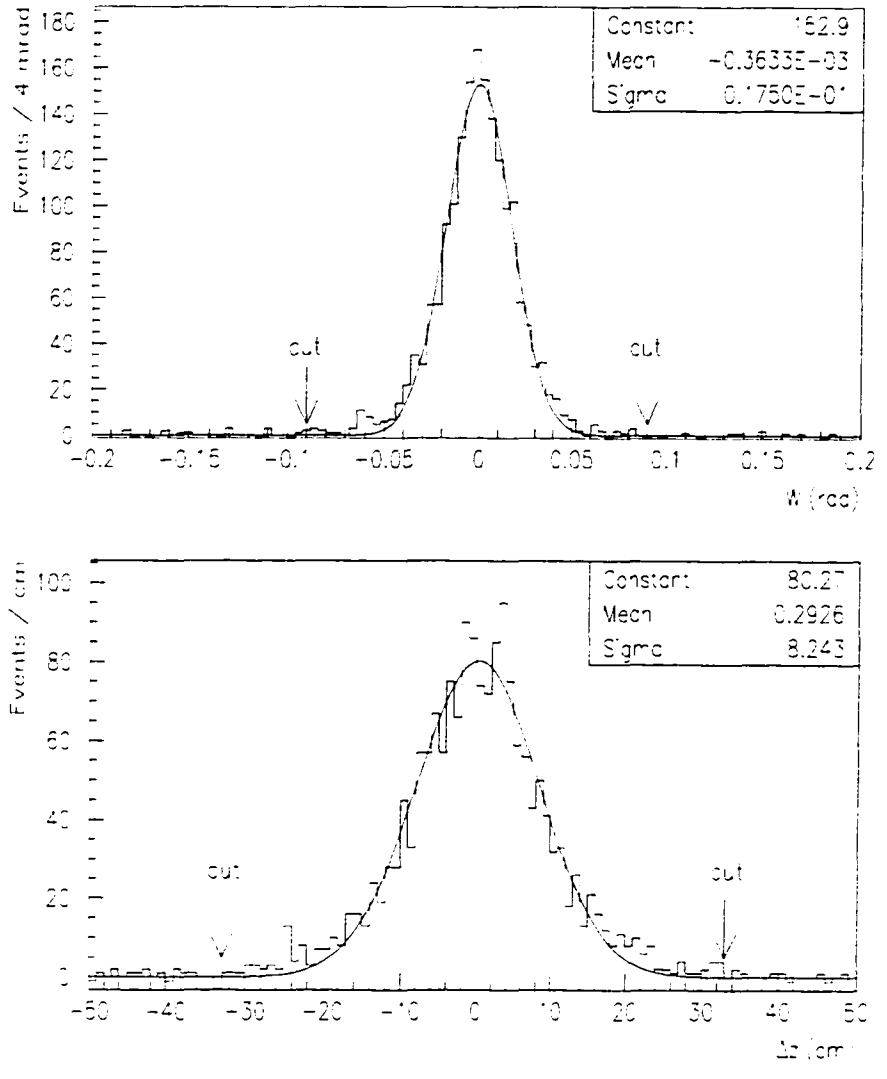

Figure 4-8: Mismatch variable distributions for muons passing the gamma-muon analysis selection cuts $p_T \geq 4$ GeV and $\chi^2_r \leq 9$. The applied cuts to separate signal and background are indicated.

absolute acceptance for the CMU (due to 2.4° gaps every 15°), yield a geometrical acceptance for CMU-CMP coincidence of 53%.

We performed the same Monte Carlo study for muons with a $P_T^\mu > 4$ GeV and $|\eta| < 1.0$ in the CMP and found:

$$A * \epsilon(\mu)_{CMP} = 0.34 \pm 0.01. \tag{4.7}$$

The corresponding number for the CMX, with the same P_T and η cuts, was found to be:

$$A * \epsilon(\mu)_{CMX} = 0.23 \pm 0.01. \tag{4.8}$$

Combining these results, we found that the total CDF acceptance and efficiency for muons with $P_T^\mu > 4$ GeV and $|\eta^\mu| < 1.0$ was:

$$A * \epsilon(\mu)_{CMP-CMX} = 0.57 \pm 0.01. \tag{4.9}$$

There is one additional acceptance that is needed in order to make the connection to a photon - heavy quark cross section, namely, the acceptance for a heavy quark in a given pseudorapidity interval to decay into a muon in our fiducial volume ($|\eta| < 1.0$). We note that this number is potentially strongly process and fragmentation dependent. Consequently, we do not apply this acceptance to the data to obtain a photon charm cross section. Instead, in Section 4.10 we compare our data to the PYTHIA prediction for the $\gamma - c$ contribution to the $\gamma - \mu$ cross section by studying the Monte Carlo with the charm forced to decay to muons. We then also compare our data to a NLO calculation, where we convolute the NLO differential cross section $\frac{d\sigma}{dE_T^c}$ with the PYTHIA prediction for the charm turn-on.

4.6 Muon Background Estimates

The muon backgrounds in this analysis are complicated by the fact that we require CMU-CMP coincidence in the CMP fiducial volume, and by the fact that we accept

CMX muons, when the CMX accidental CTC–stub match rate is known to be non-negligible. The CMX accidental CTC–stub background will be discussed in 4.6.1, and found to be controllable, and the corresponding CMP background has been determined to be negligible. Thus, one is left with the usual muon backgrounds of punch-through and decays-in-flight of pions and kaons.

In addition to the standard muon background of decay-in-flight in the CTC, in the CMP fiducial volume one can have a punch-through in the CMU that decays to a real muon en route to the CMP, or double punch-through in the CMU and CMP. For conciseness, we lump the latter two categories together and refer to them as "punch-through". In the CMX things are simpler, and the backgrounds are more like the CMU only muons, except that the CMX suffers from accidental track-stub matches, as discussed below.

We estimate the number of decay-in-flight and punch-through muons in our sample by following several approaches. One is an approach discussed in [28], which uses an analytical method for estimating the background. We also used a Monte Carlo approach described in [28], and as a cross-check we invoked the data-motivated method described in [29].

We find all background estimates to be in good agreement, but we chose the Monte Carlo method as our final estimate because it is the most rigorous.

4.6.1 CMX Accidental Background

The background to real muons is higher in CMX than in CMP, due to the accidental match of a CTC track to a background stub created by a secondary particle scattering off of the beam pipe. To estimate this background, we divide the $W-\Delta z$ plane into signal and background regions at $|W| = 0.09$ and $|\Delta z| = 33$, as shown in Figure 4-9. One expects that the muon events found in the CMX are a sum of two distributions in the matching variables - a narrow Gaussian distribution due to prompt muons (with 3 σ limits determined from ψ's as discussed in Section 4.4), and a broader distribution

due to the accidental track-stub matches. One might worry that the background estimate is sensitive to the placement of the background cuts in the $W-\Delta z$ plane. In order to study the possibility of the signal distribution leaking into the background regions, we varied the background region cuts as shown in Figures 4-10 and 4-11. The final values chosen here for the background region cuts, $|W| \geq 0.15$ and $|\Delta z| \geq 50$, yield good statistics in the background regions, while for cuts much closer to the signal region the background estimate becomes unstable.

If one refers to the populations of the regions labeled as 1, 2, 3, and 4 in Figure 4-9 as A, B, C, and D, respectively, then, assuming the populations are symmetric in the $W - \Delta z$ plane, one can extrapolate the background into region 1 (the signal region) from the various background regions. One can estimate the background under the signal region by taking the population in region 2, and scaling it by normalizing one half of the population of region 4 to the population of region 3 (the factor of one half coming in because one is normalizing four boxes to two). The background estimate is:

$$\#BackgroundEvents = \frac{1}{2}B\frac{C}{\frac{1}{2}D} = B\frac{C}{D}. \tag{4.10}$$

As mentioned above, we have here assumed the background signal is symmetric in the variables chosen. One might worry that the above relation is sensitive to asymmetry in the $W-\Delta z$ plane. However, we have examined the populations of the 4 boxes in region 4, and found them to be similar, as shown in Table 4.1, along with the results of the background estimate. The numerical results of the background estimates for the various choices of background cuts are displayed in Table 4.2. We find a total of 87 events in the signal region, with a background estimate of 11.7 ± 2.7 events.

4.6.2 Analytic Decay-in-Flight Estimate

The first approach we used to estimate the decay-in-flight and punch–through muon backgrounds in our data was an analytic method. The P_T distribution for decay-in-

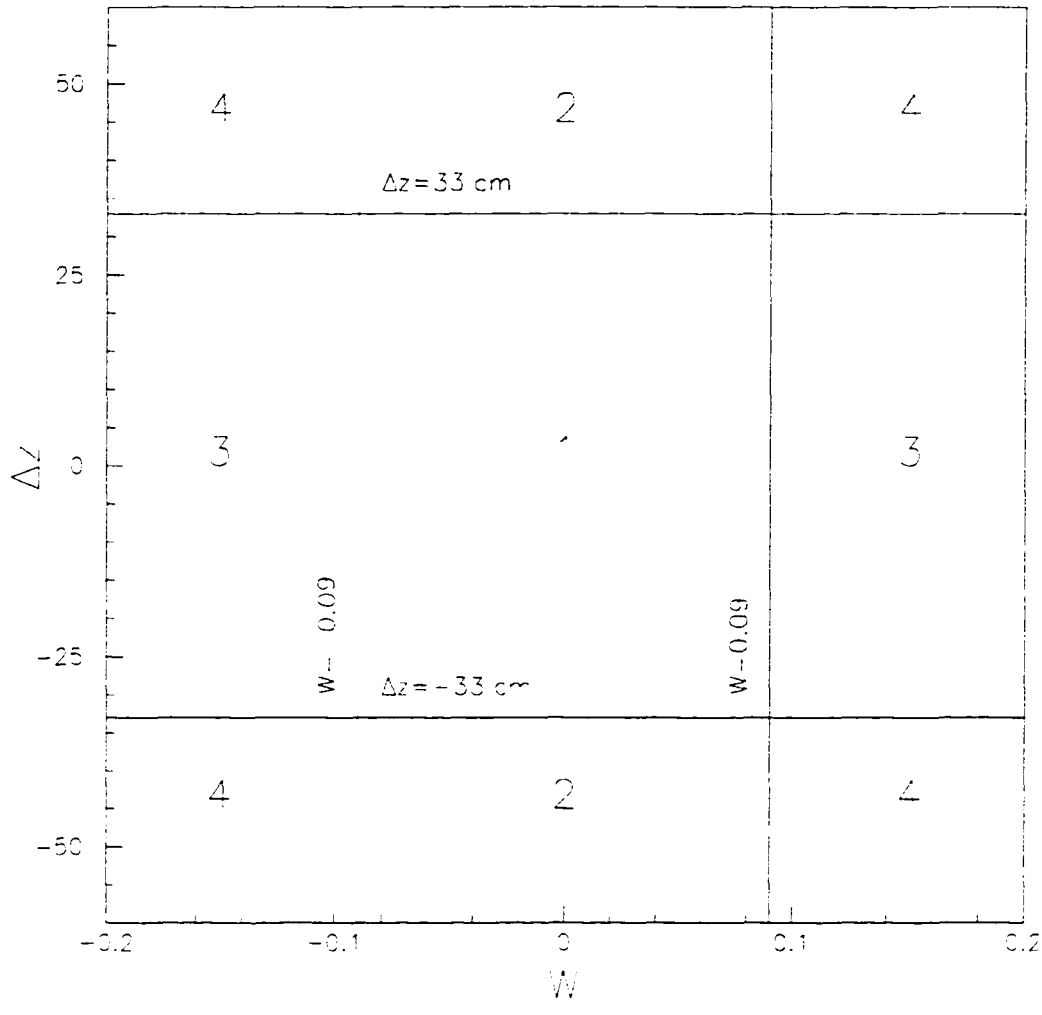

Figure 4-9: Cuts used in the $W-\Delta z$ plane. The regions labeled as 2, 3, and 4 correspond to background, while region 1 corresponds to signal. The 4 boxes labeled as region 4 were checked and found to have a similar population.

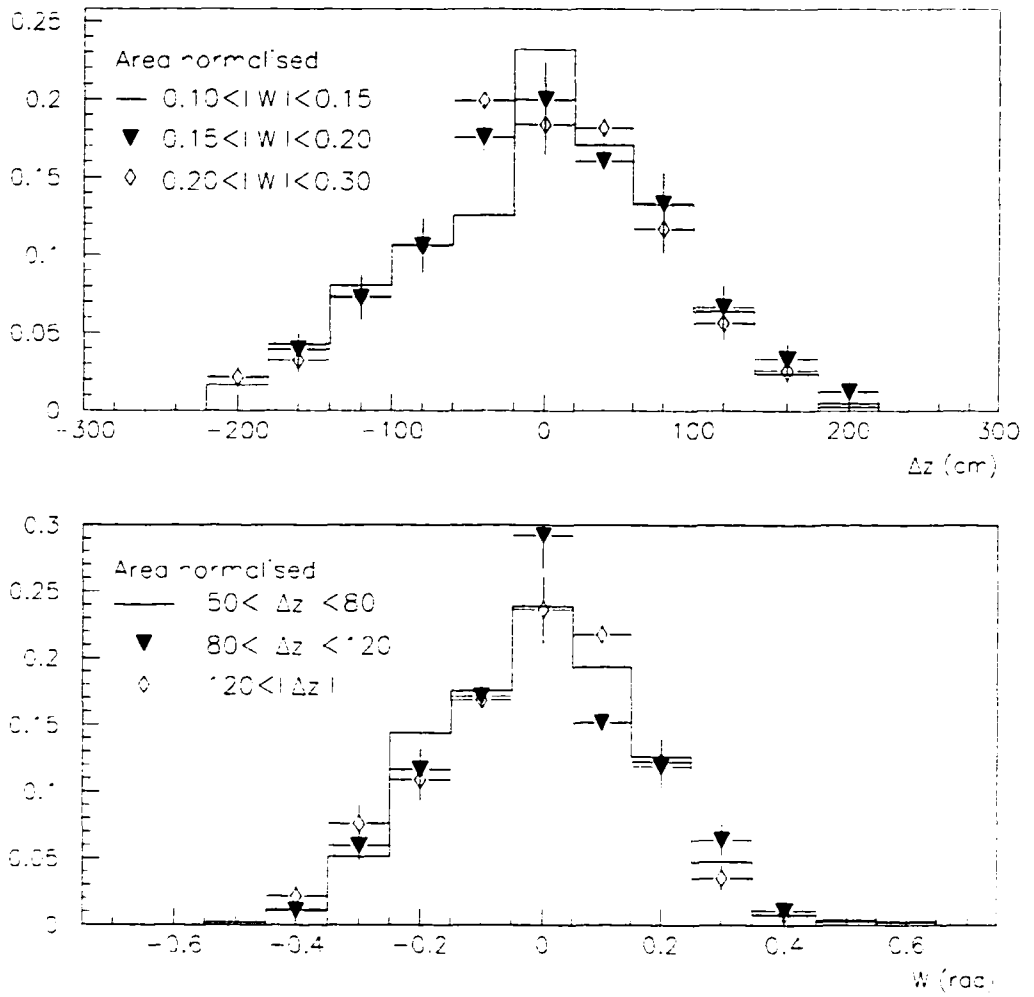

Figure 4-10: Δz plotted in slices of W (top), and W plotted in slices of Δz (bottom).

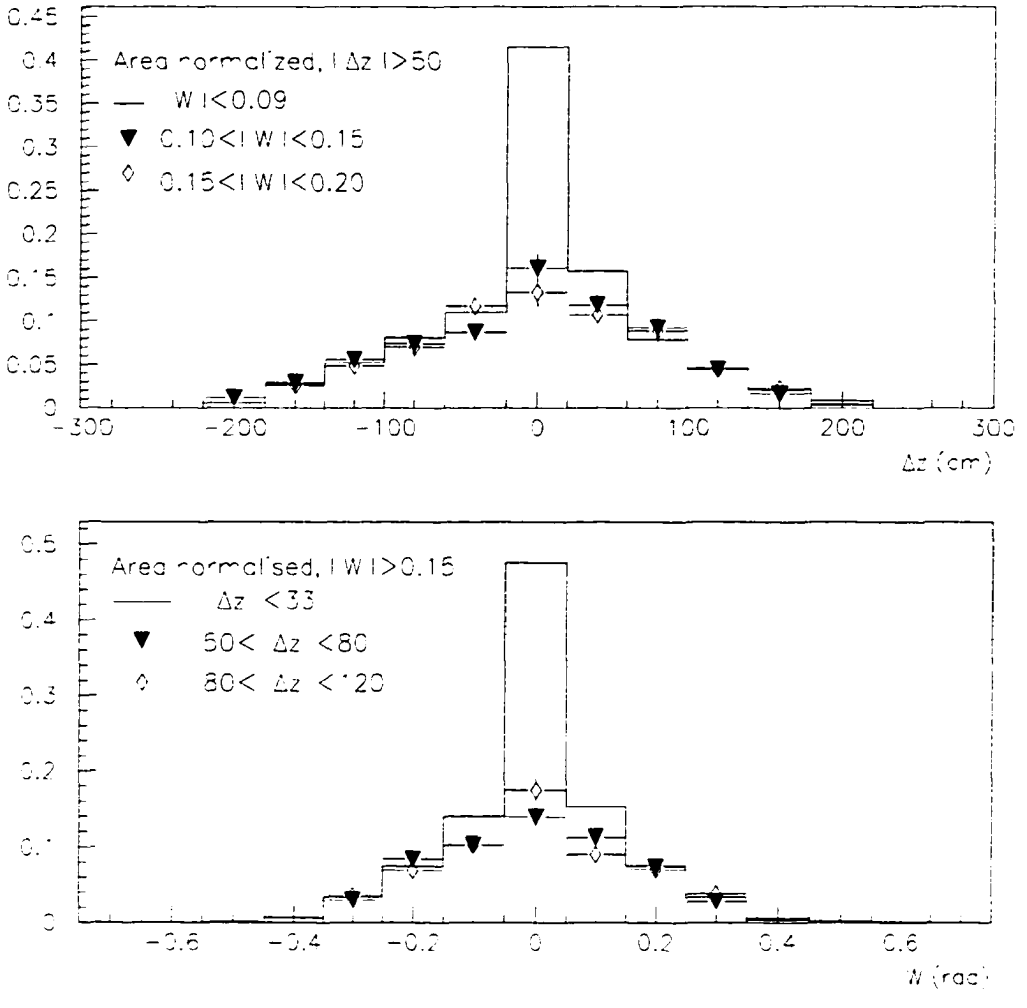

Figure 4-11: Δz plotted in slices of W (top), and W plotted in slices of Δz (bottom), but with the signal region included.

Region	Number of events
$\|W\| < 0.09, \|\Delta z\| < 33$cm	87
$\|W\| < 0.09, \|\Delta z\| > 50$cm	35
$\|W\| > 0.15, \|\Delta z\| < 33$cm	9
$\|W\| > 0.15, \|\Delta z\| > 50$cm	27
$\|W\| > 0.15, \Delta z > 50$cm	14
$\|W\| > 0.15, \Delta z < -50$cm	13
$W > 0.15, \|\Delta z\| > 50$cm	12
$W < -0.15, \|\Delta z\| > 50$cm	15
Background Estimate	11.7 ± 2.7

Table 4.1: Number of events found in the various regions of the $W - \Delta z$ plane.

flight muons can be related to the P_T distribution for charged tracks via the following equation:

$$\frac{dN_{DiF}}{dp_{t\mu}} = f\int_{p_{t\mu}}^{1.742p_{t\mu}} \frac{dN_{Tracks}}{dp_{t\pi}}(1 - exp(-\frac{\alpha}{p_{t\pi}}))\frac{1}{.426p_{t\pi}}dp_{t\pi} \qquad (4.11)$$
$$+f\frac{K}{\pi}BR\int_{p_{t\mu}}^{21.93p_{t\mu}} \frac{dN_{Tracks}}{dp_{tK}}(1 - exp(-\frac{\beta}{p_{tK}}))\frac{1}{.954p_{tK}}dp_{tK},$$

where $\alpha = 1.79 \times 10^{-4}R$,$\beta = 1.33 \times 10^{-3}R$,BR is the $K \rightarrow \mu\nu$ branching ratio, f is the fraction of charged particles that are pions, and $\frac{K}{\pi}$ is the ratio of charged kaons to pions. (R is the radius over which one is allowing the mesons to travel. Naively, one would take this to be the CTC radius (150cm), but as shown in [28] it is, in fact, better to take R = 200cm, which takes into account mesons which enter the calorimeter, but decay before showering.)

The above equation was evaluated for five bins in muon P_T from 0 to 20GeV in a discrete approximation. The charged particle distribution was measured in bins of 1GeV for a photon sample of known luminosity passing our photon cuts, and is shown in Figure 4-12. (Note that since we are subtracting decay-in-flight muons

Region	Number of events
$\|W\| \geq 0.10$, $\|\Delta z\| < 33$cm	17 ± 4.12
$\|W\| < 0.09$, $\|\Delta z\| \geq 50$cm	35 ± 5.92
$\|W\| \geq 0.10$, $\|\Delta z\| \geq 50$cm	35 ± 5.92
Background Estimate	17 ± 10.10
$\|W\| \geq 0.15$, $\|\Delta z\| < 33$cm	9 ± 3.00
$\|W\| < 0.09$, $\|\Delta z\| \geq 80$cm	22 ± 4.69
$\|W\| \geq 0.15$, $\|\Delta z\| \geq 80$cm	18 ± 4.24
Background Estimate	11 ± 10.61
$\|W\| \geq 0.20$, $\|\Delta z\| < 33$cm	6 ± 2.45
$\|W\| < 0.09$, $\|\Delta z\| \geq 120$cm	9 ± 3.00
$\|W\| \geq 0.20$, $\|\Delta z\| \geq 120$cm	4 ± 2.00
Background Estimate	13.5 ± 13.53

Table 4.2: Numerical results of the background estimate method varying the background cuts in the $W-\Delta z$ plane.

from a sample that is already photon background subtracted, the charged particle distribution used for the integral is also photon background subtracted.) The integral over pion/kaon momenta was performed numerically over this measured distribution. This sum was then scaled for the difference in luminosities between the sample used to obtain the charged track distribution and the full photon sample.

In addition, we estimate analytically the number of punch-throughs by noting first that by counting the number of interaction lengths traversed by a particle fiducial to the various CDF muon systems one finds that the probability of a double punchthrough in both the CMU and the CMP is about e^{-8}, as can be seen in Figure 4-15. (This is in fact a negligible contribution to our sample, but we include it for completeness.) Similarly, by counting the number of interaction lengths before the CMU, we estimate the probability of a pion CMU punchthrough followed by a decay before the CMP to be:

$$e^{-4.5}\frac{28\%}{P_T(\mathrm{GeV})}, \tag{4.12}$$

and the corresponding probability for a kaon to be:

$$e^{-4.5}\frac{4.1\%}{P_T(\mathrm{GeV})}. \tag{4.13}$$

So with reasonable assumptions about $\frac{\pi}{K}$, etc., we find:

$$N_{CMP} = N_{track}(e^{-8} + \frac{1}{5}e^{-4.5}\frac{0.28}{P_T} + \frac{3}{5}e^{-4.5}\frac{0.041}{P_T}). \tag{4.14}$$

where N_{CMP} is the number of punch-throughs expected in the CMP. A similar analysis of the CMX, where punchthrough followed by decay is not an issue, yields the simple relation

$$N_{CMX} = N_{track}e^{-7}, \tag{4.15}$$

where the value of the exponent can be extracted from Figure 4-15.

This background estimation method, while satisfying for its analytic nature, nonetheless neglects all tracking reconstruction effects. Thus, though we find this method a useful cross check, we ultimately invoke the Monte Carlo decay-in-flight and punchthrough estimate described in Section 4.6.3.

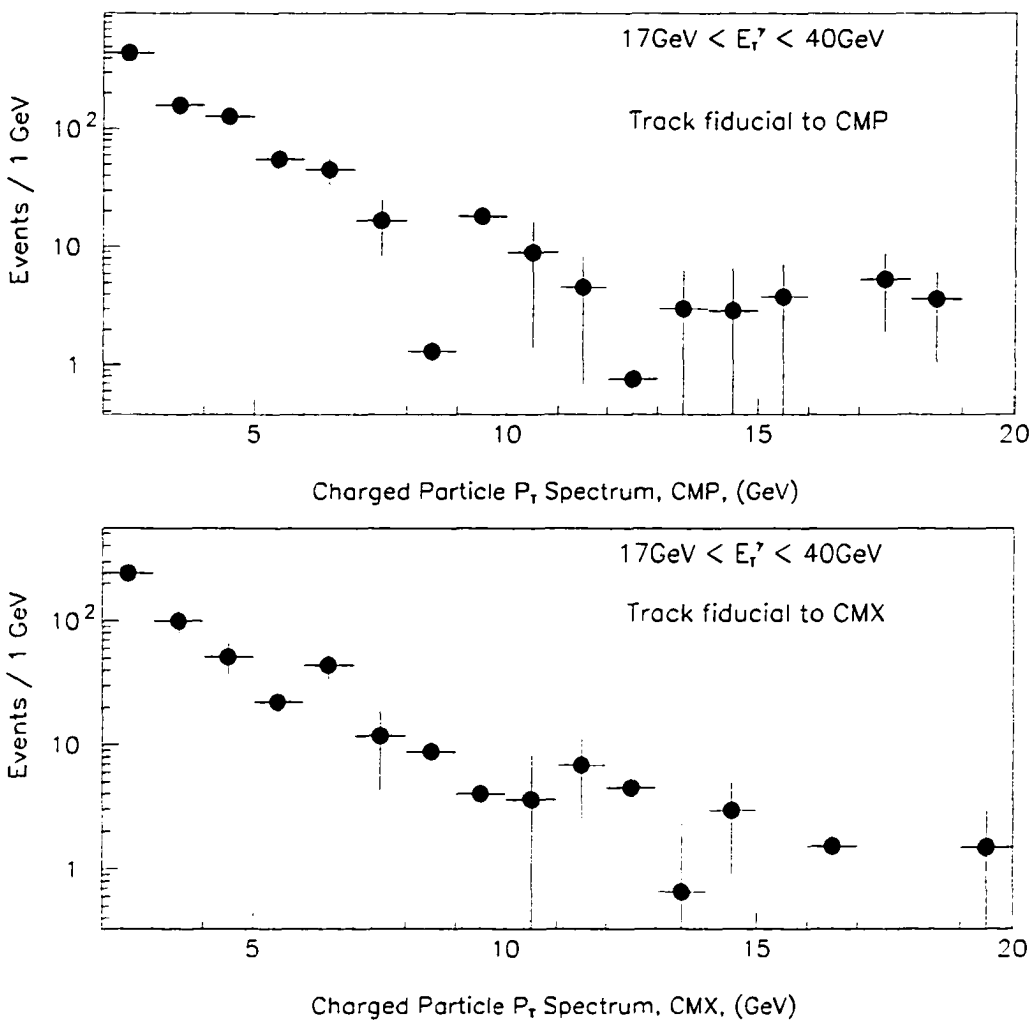

Figure 4-12: P_T distribution for charged tracks fiducial to the CMP and CMX muon detectors in the 16GeV photon sample.

4.6.3 Monte Carlo Decay-in-Flight Estimate

There are a number of important effects that are neglected in the analytical decay-in-flight calculation. The most important are the assumed 100% efficiency of track reconstruction and offline cuts for decays in the CTC, the assumption that the reconstructed momentum was always the muon's and not the meson's, and the assumption that mesons that enter the calorimeter never decay before showering. These effects are shown schematically in Figure 4-13. The first effect decreases the final result.

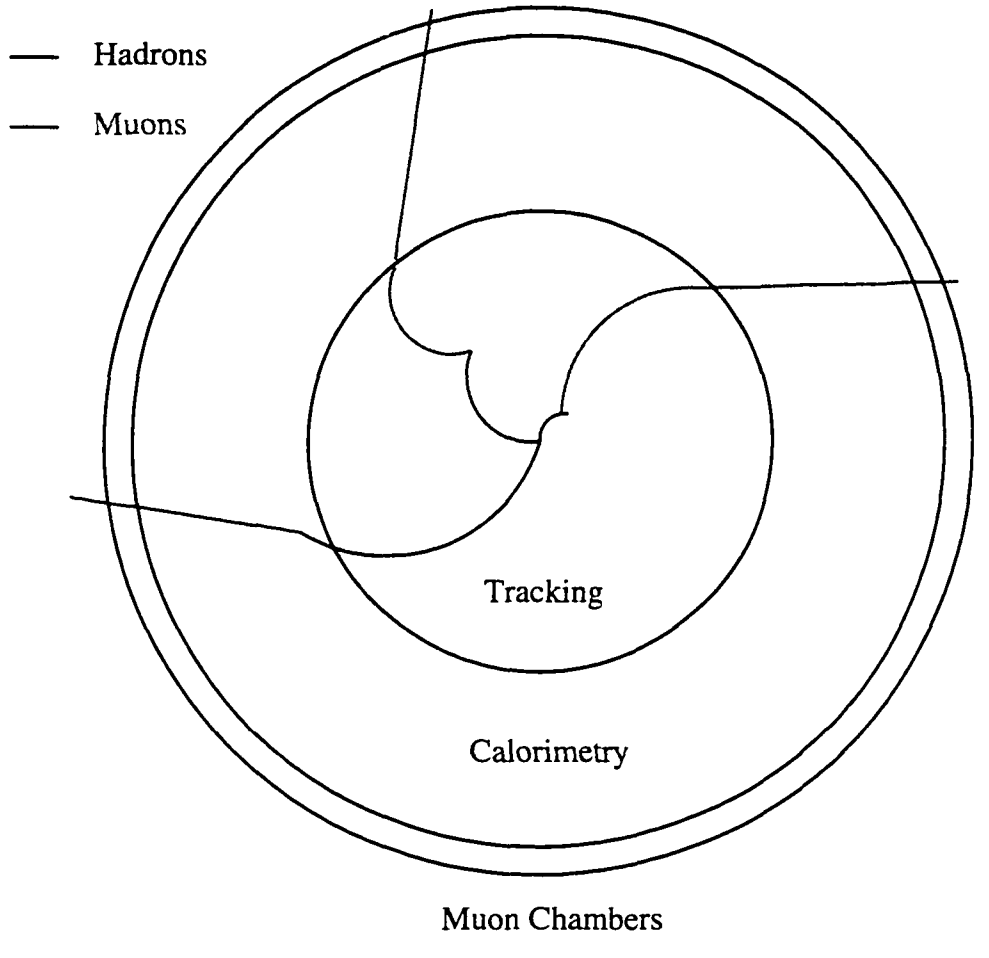

Figure 4-13: Shown here are the possible reconstruction pathologies that can occur when a charged meson decays in flight to a muon before traversing the muon chambers.

The other two cause an increase in the background. In order to take these effects

into account we used a Monte Carlo simulation approach. The ingredients of this simulation that are relevant to our results are the following:

- The lifetimes of kaons and pions;
- The relative fractions of kaons and pions;
- The number of interaction lengths in the CDF calorimeters, CMP walls and return yoke; and
- Realistic tracking pattern recognition in the CTC.

The input to the Monte Carlo was the charged particle spectrum measured for events passing the photon cuts in a sample with an integrated luminosity of 0.55 pb^{-1}. We performed the Monte Carlo study twice, once assuming all the particles were kaons and a second time assuming they were pions. After investigating published measurements of the $\frac{K}{\pi}$ and $\frac{p}{\pi}$ ratios at the energies probed by CDF, the two results could be combined easily.

Figure 4-14 shows the decay radius distribution of kaons (pions) for reconstructed muons in the CMU-CMP with $P_T \geq 2$ (4) GeV and passing all the other muon cuts. One can see that a significant fraction of the kaons decaying inside the CTC volume do not pass the cuts. This due to the fact that the mass difference between kaons and muons produces a kink in the track trajectory that causes the tracking reconstruction code to fail to reconstruct a high quality track. Furthermore, the requirement that the reconstructed track point at both the interaction point and the muon chamber stub rejects a significant fraction of the decay-in-flight candidates.

The results of the Monte Carlo calculation are shown as a function of P_T^{μ} in Table 4.3, and, as a function of the particle fractions, in Table 4.4. 15% (40%) of the total decay-in-flight estimate is due to kaons (pions) that decay before the calorimeter, and 45% are hadrons that decay in the calorimeter volume. It is interesting to note that the background levels of the CMU-P coincidences and CMX are very similar. As

shown in Figure 4-15, the number of interaction lengths seen by a pion travelling to the CMU-P is 8-9. For the CMX this number is between 6 and 9 interaction lengths, depending of the azimuthal and polar angles.

In order to estimate the fractions of kaons and pions in CDF data, we examined the literature for measurements of the charged particle fractions at energies probed by CDF. From hadronic collisions, the majority of the data come from low energy experiments. E605 [31] studied protons impinging on either beryllium or tungsten target for $\sqrt{s} = 38.8$ GeV, and measured the charged particle fractions up to $P_T = 10$ GeV. Their numbers agree well up to 6 GeV with the data collected by the Chicago - Princeton collaboration at $\sqrt{s} = 27.4$ GeV [32]. E735 at the Tevatron C0 interaction region measured the charged particle fractions at our energies, but only up to $P_T = 1.4$ GeV [33]. Finally, CDF [34] has measured the inclusive K_s^0 spectrum up to 7 GeV. This can be translated into a $K^{\pm}$ fraction, but, unfortunately, nothing more can be said about the number of pions.

One reason for concern about using the inclusive numbers coming from hadronic collisions is that they are dominated by minimum bias events. For example, in the E605 and the CP data, there is a large difference between the particle and antiparticle fractions. These data are thus dominated by the valence quark structure of the hadrons colliding. As is shown in [35], the particles in their data with $P_T \geq 4$ GeV are just the tail of an exponential distribution with a mean value of about 400 MeV. The contribution to this spectrum due to hard scattering processes producing jets is very small. The CDF Run 1A spectrum follows the same exponential up to $P_T \approx 1$ GeV, but for larger values the data develops a tail. For $P_T \approx 4$ GeV, the cross section is more than two orders of magnitude larger than the CP data, and our interpretation is that the excess is produced by a much larger component of hard parton-parton scattering producing jets in the final state. However, if one still wanted to use the hadronic collision data, the fractions we estimated from the E735 data were $\pi/K/p = 0.60/0.20/0.20$.

Since we are triggering with a photon of 16 GeV, we expect that the high P_T piece of the charged particle spectrum for our events is formed by the tracks belonging to the jet that recoils against the photon. We thus decided that the CDF Run 1A particle fractions would be better modeled by the fractions measured in $e^+ - e^-$ colliders, such as the data published from PEP, PETRA and LEP. In Table 4.4 we show the numbers obtained using TASSO [36], OPAL[37], and ALEPH [38] data. The fractions obtained in this way are very close to each other. *A posteriori*, it is also interesting to see that the LEP numbers are not very different from the low energy hadron collision results.

In Table 4.4 we show the number of decay-in-flight events expected in our data for different assumed particle fractions. The spread of the numbers is 6% if we restrict ourselves to the $e^+ - e^-$ experiments, while if we accept as a realistic possibility the E735 fractions the systematic variation is 13%. The errors in the table correspond to the finite statistics of the simulated sample. Additional systematic errors in this estimate are 3% from our limited knowledge of the charged particle spectrum in events with a photon and another 3% obtained when we changed the number of absorption lengths seen by a meson by $\pm 10\%$.

4.6.4 Background Estimate from the Data

The muon backgrounds found amongst CMU-CMP candidates can also be determined directly from the data. As shown in [29], the probability for a real CMU muon to result in a CMU-CMP reconstruction can be determined by studying $\psi \rightarrow \mu^+\mu^-$ events, while the probability for a CMU punch-through meson to result in a CMU-CMP reconstruction can be determined by studying $K_s^0 \rightarrow \pi^+\pi^-$ events. Given the assumption that all CMU stubs are background (an assumption justified by the relative number of interaction lengths before the CMU and CMP), one can treat these two samples, the μs and πs, as samples of pure signal and background.

In this way it has been determined that the probability for a CMU muon candidate in the CMU-CMP fiducial region to actually form a stub in the CMP is flat for $P_T \geq 3$

CMP P_T^μ Bin	Decay-in-Flight and Punch–Through	Muon Events	Photon-Muon Events	Photon-Prompt Muon
4.0GeV $< p_t^\mu <$ 8.0GeV	35±0.82	104	86±15	51±15
8.0GeV $< p_t^\mu <$ 12.0GeV	4.0±0.23	25	17±7	13±7
12.0GeV $< p_t^\mu <$ 16.0GeV	0.7±0.1	4	6±3	5.3±3
16.0GeV $< p_t^\mu <$ 20.0GeV	0.3±0.05	2	0±2.7	0±2.7
CMX P_T^μ Bin	Decay-in-Flight and Punch–Through	Muon Events	Photon-Muon Events	Photon-Prompt Muon
4.0GeV $< p_t^\mu <$ 8.0GeV	27±0.75	73	22±12	-5.0±12
8.0GeV $< p_t^\mu <$ 12.0GeV	2.5±0.2	12	10±5	7.5±5
12.0GeV $< p_t^\mu <$ 16.0GeV	0.7±0.1	2	3±2	2.3±2
16.0GeV $< p_t^\mu <$ 20.0GeV	0.3±0.1	0	0±0	0±0

Table 4.3: Decay-in-Flight and Punch-Through Results: The first column is the decay-in-flight and punch–through estimate for the bin, the second is the number of events in the raw photon sample with muons, and the third is the number of events with real photons and muons. The final column is the number of events with real photons and prompt muons (*i.e.*, not decay-in-flight). The negative entry in the first P_T bin of the CMX results is due to the high statistics background subtraction method discussed in Section 4.3. The errors on the last two columns are statistical only, and properly include the effects of the CES weighting.

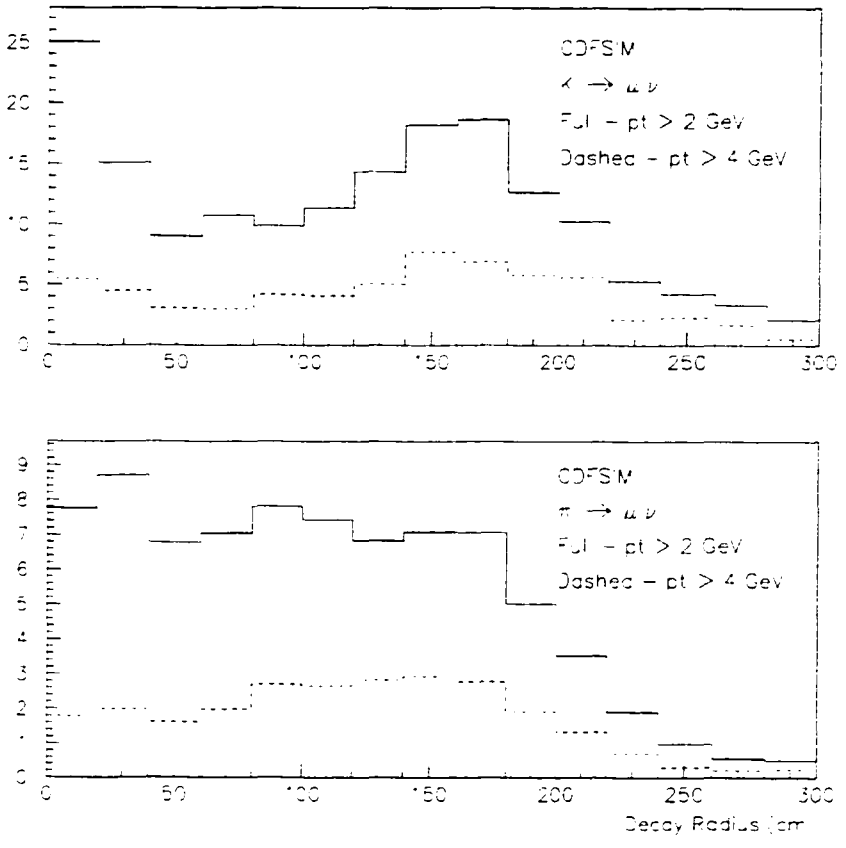

Figure 4-14: The decay radius for kaons and pions decaying in flight, and producing a muon candidate passing the cuts. The full histogram is for $P_T^{\mu} \geq 2$ GeV, and the dashed plot is for $P_T^{\mu} \geq 4$ GeV. Note the dip at roughly 75 cm in the kaon plot, which corresponds to the center of the CTC. The kinematic energy freed up in the kaon decay can result in a kink in the reconstructed track, which in turn gives rise to a reconstruction inefficiency, as displayed above.

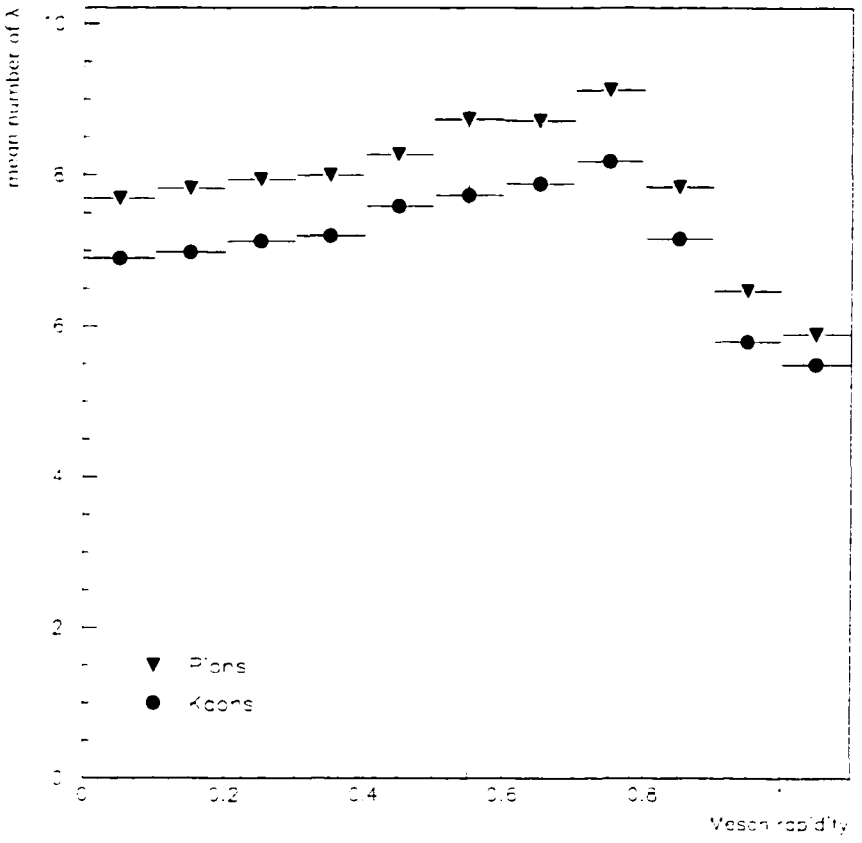

Figure 4-15: The average number of interaction lengths a meson should punch-through to reach the CMU-CMP or the CMX, and produce a muon candidate passing our cuts, as a function of rapidity. The triangles are for pions and the circles are for kaons.

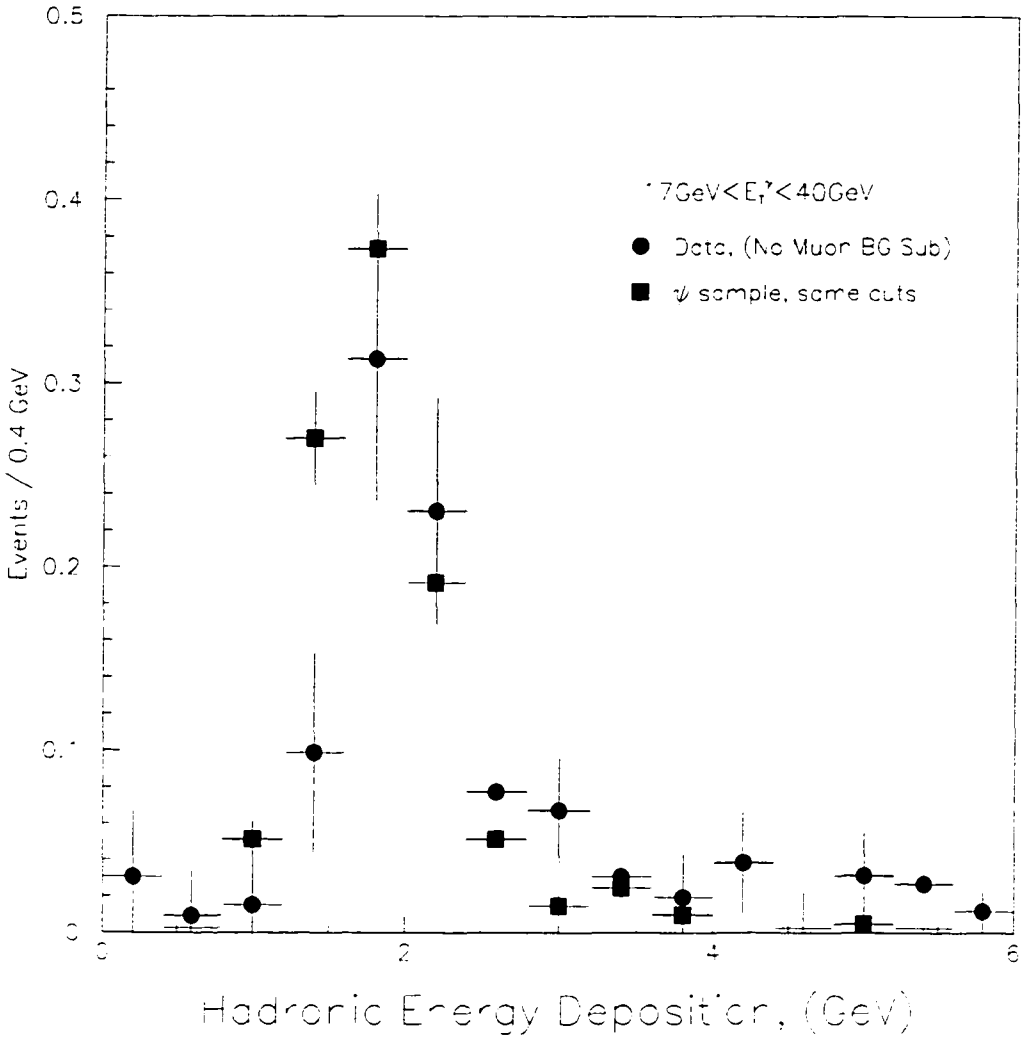

Figure 4-16: CHA energy deposition for muons satisfying our cuts, compared with ψ's. The data points are photon-weighted, and include both CMX and CMP muons.

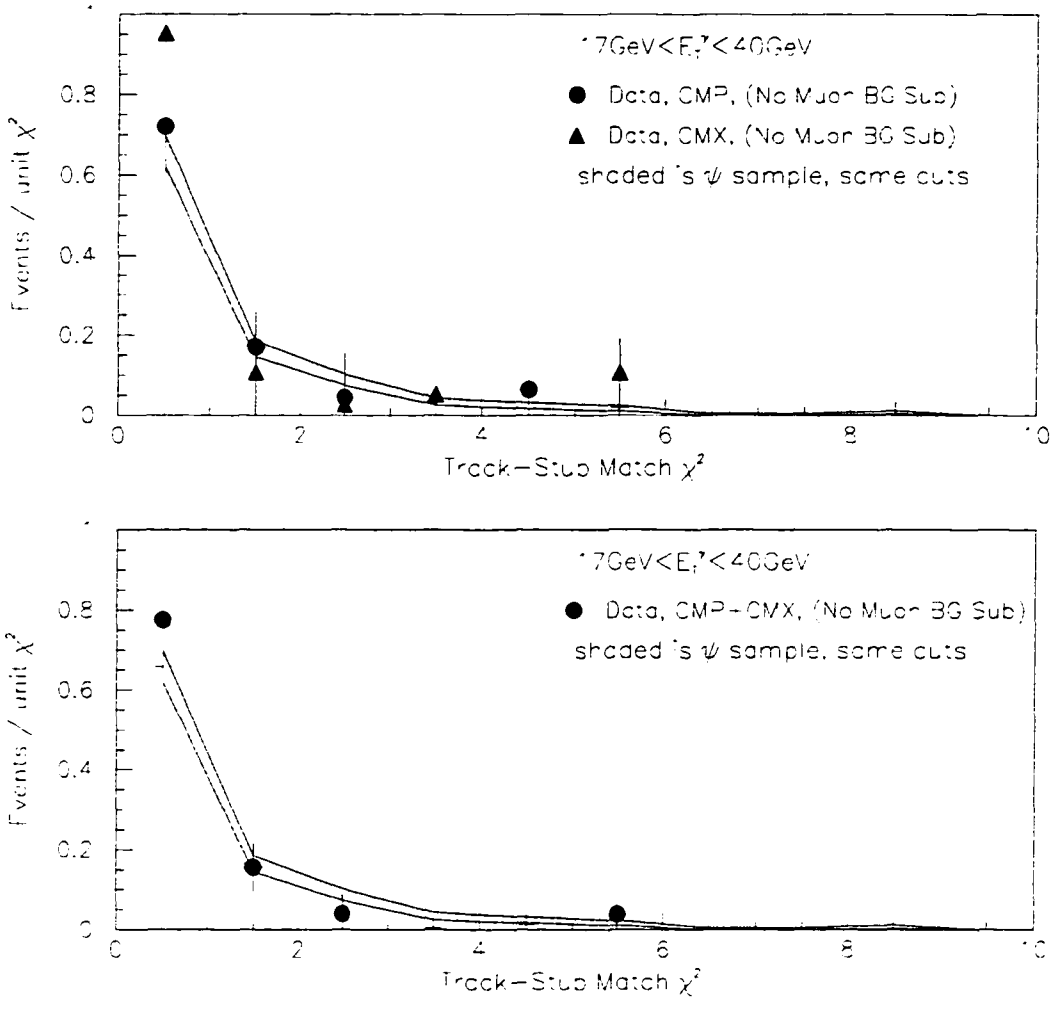

Figure 4-17: Track-stub match χ^2 for muons satisfying our cuts, compared with ψ's. All histograms are normalized to unit area, and CES-weighted.

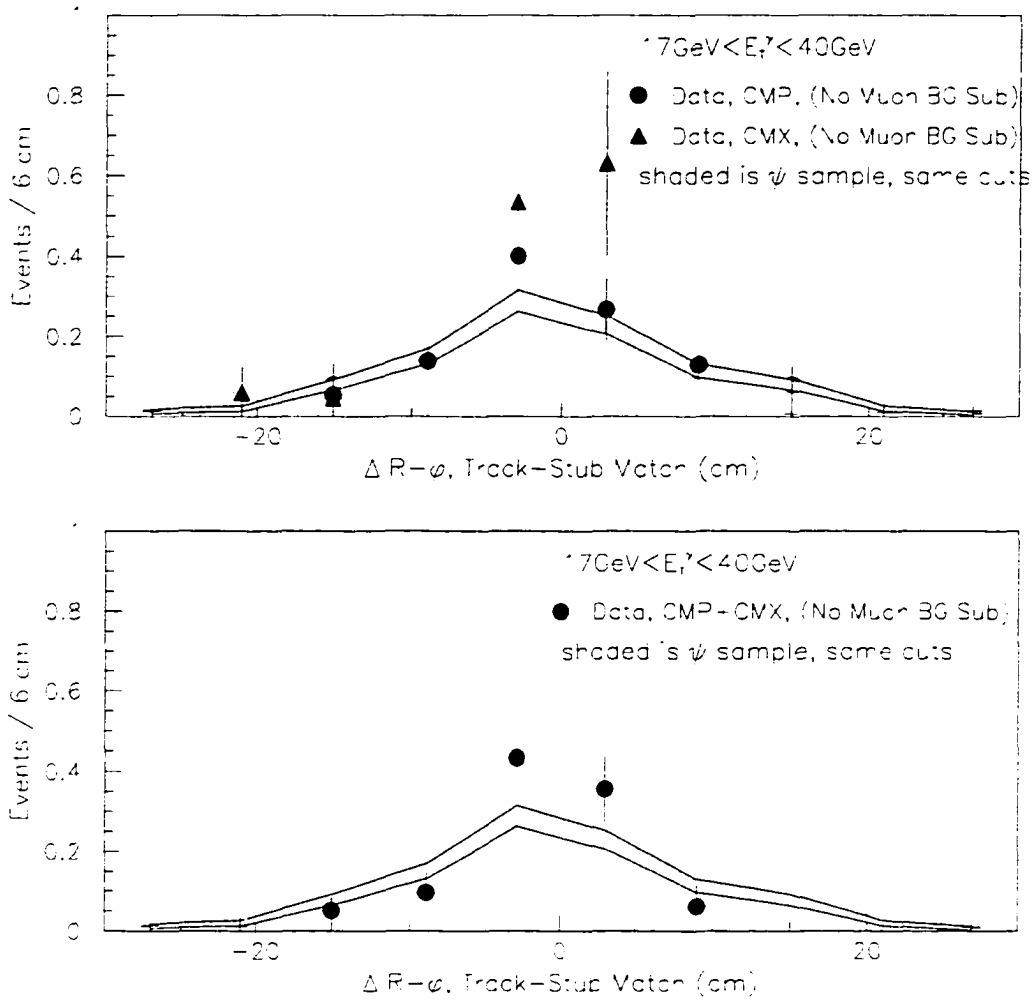

Figure 4-18: Track-stub match $\Delta R - \phi$ for muons satisfying our cuts, compared with ψ's, with the CMP and CMX displayed separately (top) and combined (bottom). All histograms are normalized to unit area, and CES-weighted.

	π	K	CMU-CMP	CMX	CMU-CMP + CMX
Pions	1.00	0.00	39.6 ± 1.2	28.3 ± 1.0	67.9 ± 1.5
Kaons	0.00	1.00	56.9 ± 2.3	53.8 ± 2.3	111.8 ± 3.4
E735	0.60	0.20	35.2 ± 0.8	27.7 ± 0.8	62.9 ± 1.1
TASSO	0.61	0.28	40.1 ± 1.0	32.3 ± 0.9	72.4 ± 1.3
OPAL	0.65	0.28	41.7 ± 1.0	33.5 ± 0.9	75.1 ± 1.4
ALEPH	0.65	0.25	40.0 ± 1.0	31.9 ± 0.9	71.8 ± 1.3

Table 4.4: Calculated decay-in-flight and punch-through numbers of events using CDFSIM for several assumptions about the charged particle fractions. The numbers are normalized to the total integrated luminosity of the $\gamma - \mu$ Run 1A sample. The CMU-CMP and CMX contributions are separated. The errors in the Table are due only to the finite statistics of the simulated sample.

GeV, and given by:

$$P(fake) = 0.46 \pm 0.04. \tag{4.16}$$

The corresponding probability for a real muon in the CMU and fiducial to the CMP is given by

$$P(muon) = 0.95 \pm 0.01. \tag{4.17}$$

From these efficiencies one can obtain a relation between the number of CMU-CMP and CMU-only candidates, and the number of real and fake muons. Inverting this expression allows one to use the number of CMU-CMP and CMU-only candidates to directly estimate the decay-in-flight and punch-through backgrounds found in the CMP.

We find 76 ± 17 CMU events without CMP confirmation and 108 ± 17 CMU-CMP events. Solving and correcting for the extra cuts, the background fraction of our sample is 44 ± 25 events. Comparison with Table 4.3 shows that the agreement with the CMP Monte Carlo decay–in–flight estimate is quite good. This method cannot

be used directly for the CMX, but the success of the Monte Carlo in the CMU-CMP makes us confident about the CMX prediction as well.

As a final cross check, we examined various muon-related variables in our sample and compared them to a clean sample of ψ's. The ψ sample was selected, as discussed in Section 4.4, by requiring two muon candidates, one of them either CMU-CMP or CMX, both with $P_T > 2$ GeV, together forming an invariant mass between 2.8 and 3.4 GeV. Figure 4-16 compares the hadronic energy deposition for muons found in the photon sample to that for muons derived from ψ decays, while Figure 4-17 compares the χ^2 of the CTC-CMP track-stub match for our muons and ψ's. In both cases good agreement is apparent. Finally, in Figure 4-18 we display the $\Delta R - \phi$ of the track-stub match, for our muons and ψ's.

4.7 Heavy Quark Background Estimates

The interpretation of the $\gamma - \mu$ cross section as a measure of the $\gamma - c$ cross section is complicated by the presence of the $\gamma - b$ background, where the bottom quark decays to a muon. As noted in Section 2.3, theory leads us to believe that the $\frac{b}{c}$ ratio in the photon sample should be about $\frac{1}{8}$. Nonetheless, we have studied kinematic variables to determine that the muons we observe do, in fact, come from charm, and not from bottom.

We estimate the bottom and charm content of the data by examining the P_T^{rel} of the muon, where P_T^{rel} is defined as the momentum of the muon times $sin(\theta)$, and θ is the angle between the muon and the nearest jet in $\eta - \phi$ space [39], as shown in Figure 4-19. For this part of the analysis, the jet is defined purely from tracks. The candidate tracks were required to have an impact parameter less than 1cm, and to originate from within 5cm of the muon vertex in z. Of these tracks, those greater than 1 GeV were taken as seeds, the seeds were then merged to form clusters, and jets were formed by adding all tracks with $P_T > 400$ MeV in a cone of R=0.7. Figure

4-20 shows the P_T^{rel} distribution for the data, compared to the PYTHIA prediction of the $b\gamma$ and $c\gamma$ Compton processes. As can be seen, the data are inconsistent with the PYTHIA $\gamma - b$ prediction, but deviate from the PYTHIA $\gamma - c$ prediction, as well.

In order to study the deviation of the data from the Monte Carlo prediction, we noted that, since the charm quark mass is relatively light compared to the final state lepton momentum, one would expect that the P_T^{rel} distribution for charm (or, for that matter, for decays-in-flight of pions or kaons), would be the same as the P_T^{rel} distribution for random tracks selected from a γ – jet data set, with P_T^{rel} calculated relative to the nearest jet in $\eta - \phi$ space. In Figure 4-21 we show the P_T^{rel} distributions for the muon data compared to random track data in the photon sample, and $\gamma - c$ Monte Carlo compared random tracks in photon-jet Monte Carlo. It is apparent that the muon data agrees with the random track data, and that the charm Monte Carlo agrees with the random track Monte Carlo, and thus the difference between the data and the Monte Carlo prediction may be attributed to PYTHIA's treatment of the transverse development of the lepton-jet system.

Since the kinematics of the $c \rightarrow \mu + X$ decay are quite simple, it follows that the problem in PYTHIA's treatment of the transverse development of the lepton-jet system should lie in how PYTHIA fragments the final state partons into the observed hadrons making up the final state jet. In order to compensate for this difference between data and Monte Carlo, we smeared the Monte Carlo tracking jets in $\eta - \phi$ space. Figure 4-22 shows the P_T^{rel} distributions for data and Monte Carlo before and after smearing the Monte Carlo jet with a 2D Gaussian of width 0.15 in $\eta - \phi$ space, yielding a good agreement between data and Monte Carlo after smearing. We justify this jet smearing by displaying in Figure 4-23 Gaussian fits to the Monte Carlo photon-charm and photon-random track distributions of $\Delta\phi$ between the lepton and the jet used to calculate P_T^{rel}, and in Figure 4-24 the same fits for data. As can be seen in these plots, the $\Delta\phi$ distributions for the data have widths of order 0.10 - 0.15 wider than those for the Monte Carlo.

Finally, in order to quantify the estimated b-fraction in our data, we performed a constrained fit of the data P_T^{rel} distribution to a normalized sum of the P_T^{rel} distributions for the $\gamma - c$ and $\gamma - b$ Monte Carlo samples, as shown in Figure 4-25. The result for the bottom fraction is $30 \pm 15\%$, consistent with the theoretical predictions. Figure 4-26 displays the χ^2 distribution for this fit as a function of the b-fraction. From this distribution we used a $\Delta\chi^2$ argument to estimate that at the 90% confidence level the bottom fraction in our data is less than 80%, which is merely a reflection of the statistical errors on our measurement.

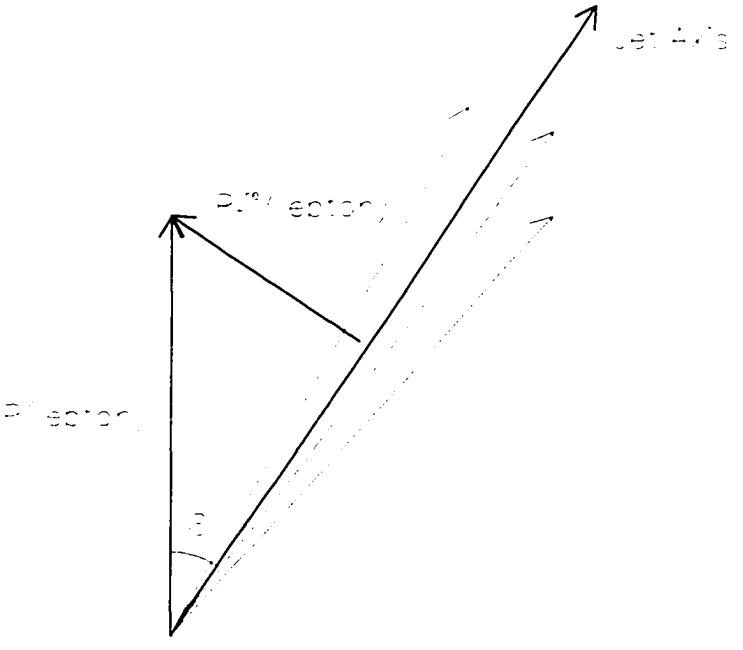

Figure 4-19: The P_T^{rel} of the muon-jet system is defined as the the momentum of the muon times the sine of the opening angle between the muon and the nearest jet in $\eta - \phi$ space.

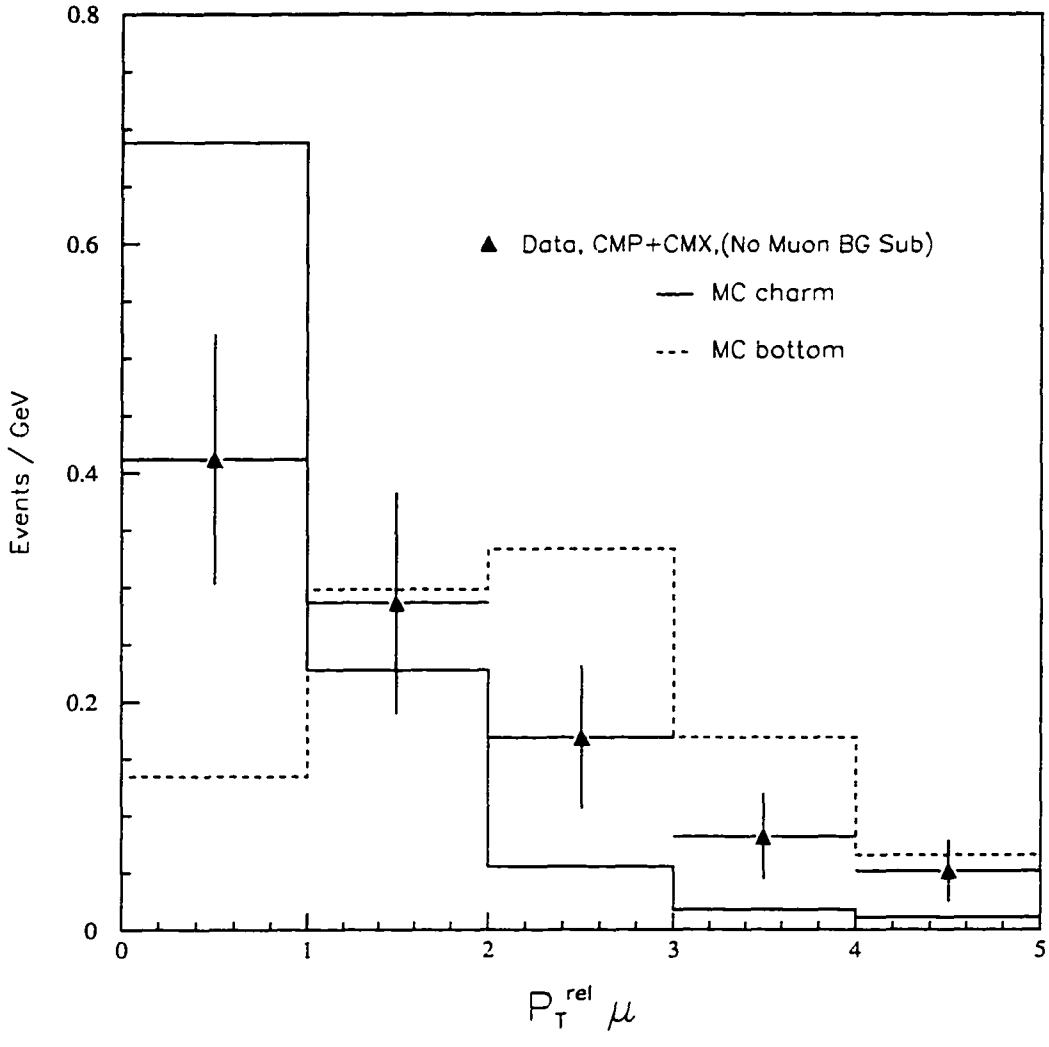

Figure 4-20: P_T^{rel} distributions for the $\gamma-\mu$ data compared to the PYTHIA prediction for the $\gamma - c$ and $\gamma - b$ Compton processes, all normalized to unit area.

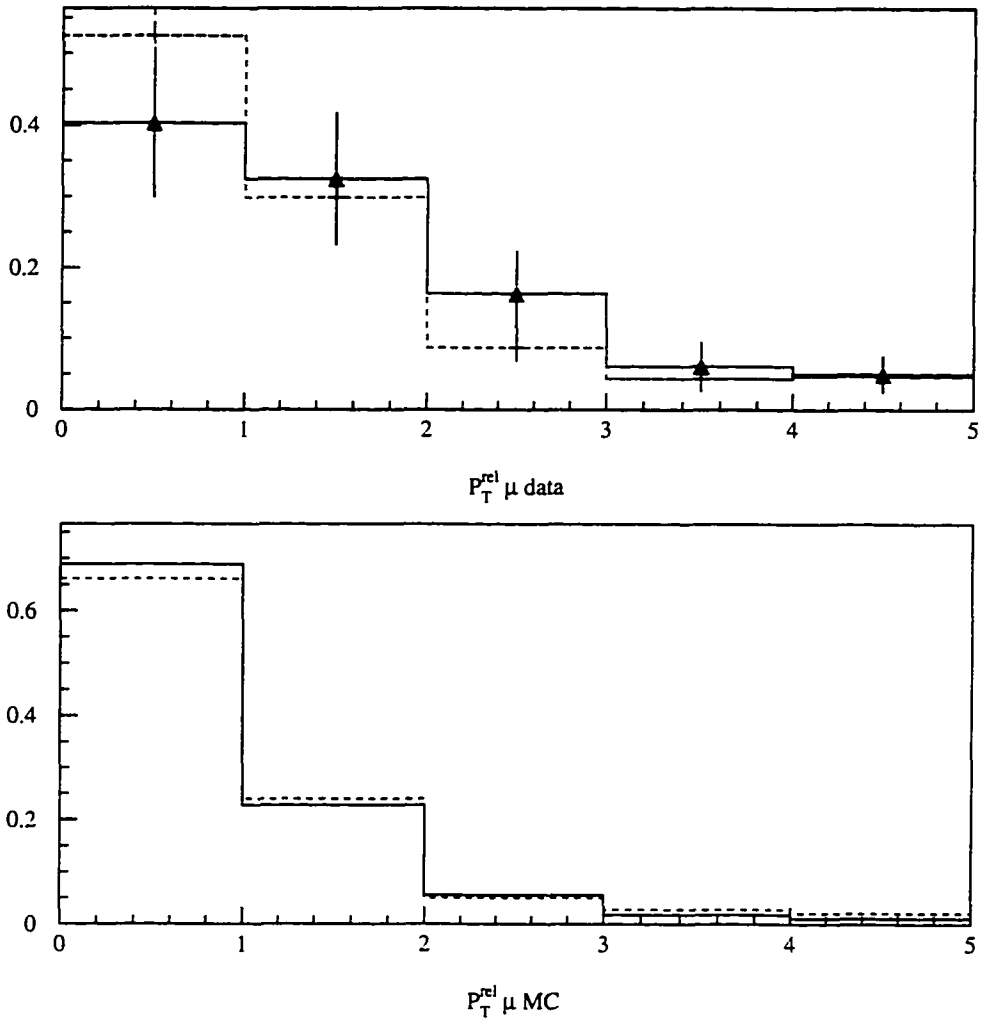

Figure 4-21: P_T^{rel} distributions for data (muons) compared to random charged particles in the photon data, normalized, at top, and the same for PYTHIA $\gamma - c$ compared to PYTHIA γ – jet, at bottom.

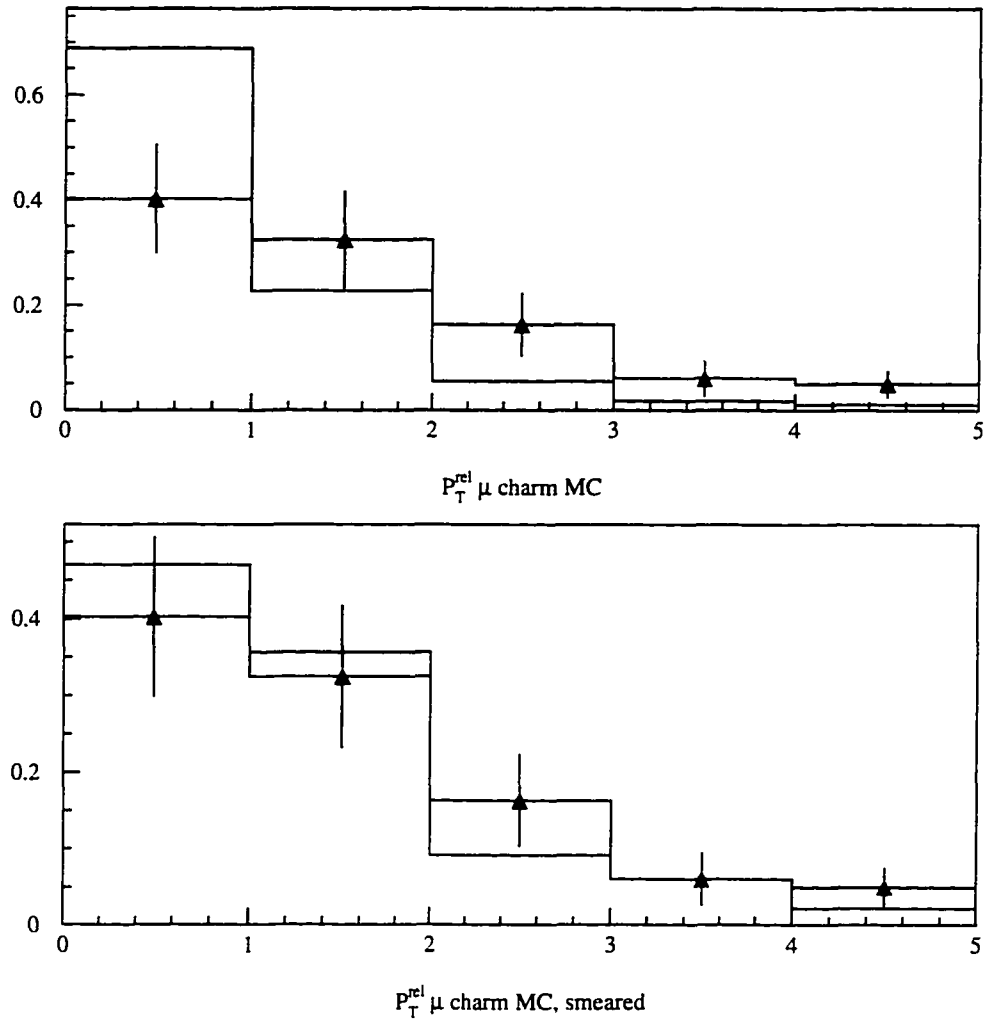

Figure 4-22: P_T^{rel} distributions for data (muons) compared to charm Monte Carlo, normalized, at top, and the same for data compared to charm Monte Carlo after smearing the Monte Carlo by a 2D Gaussian in $\eta - \phi$ space with width 0.15, at bottom.

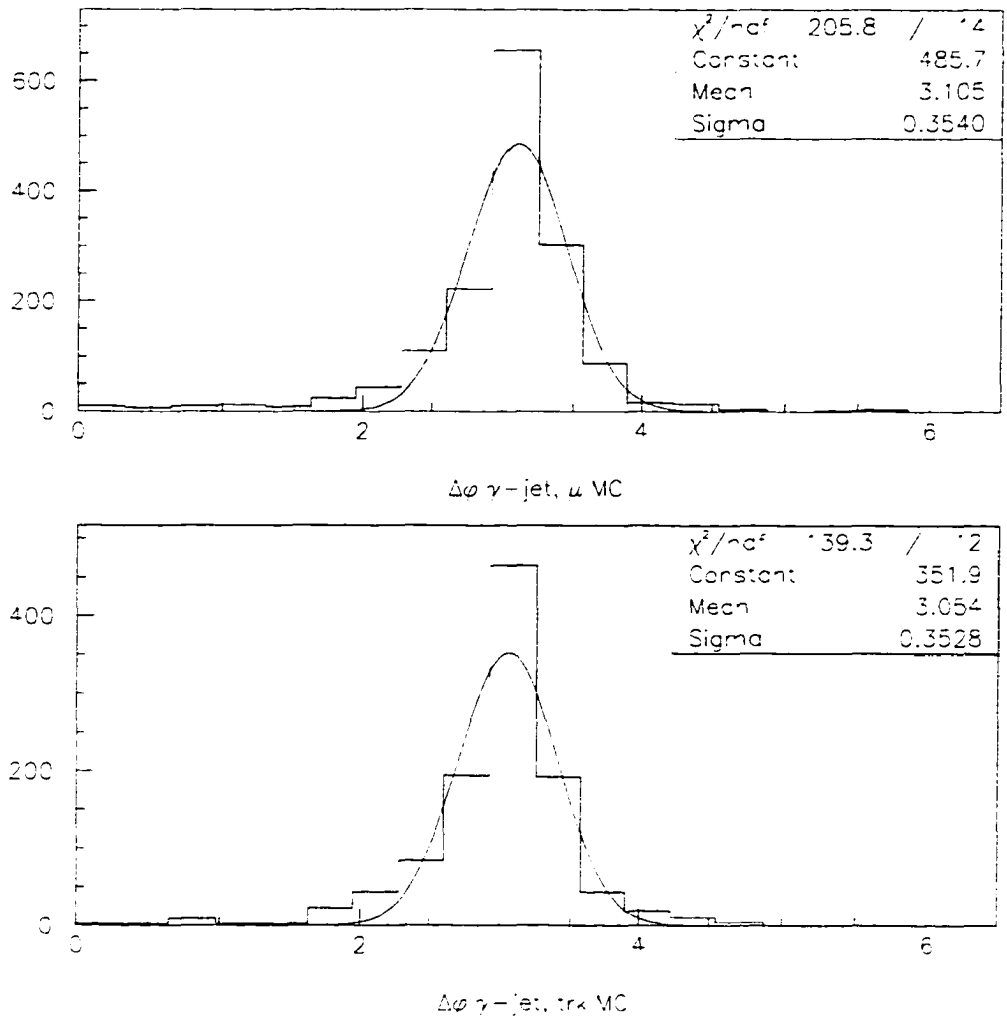

Figure 4-23: $\Delta\phi$ γ - jet for charm Monte Carlo with a Gaussian fit superimposed, at top, and the same for Monte Carlo random tracks, at bottom.

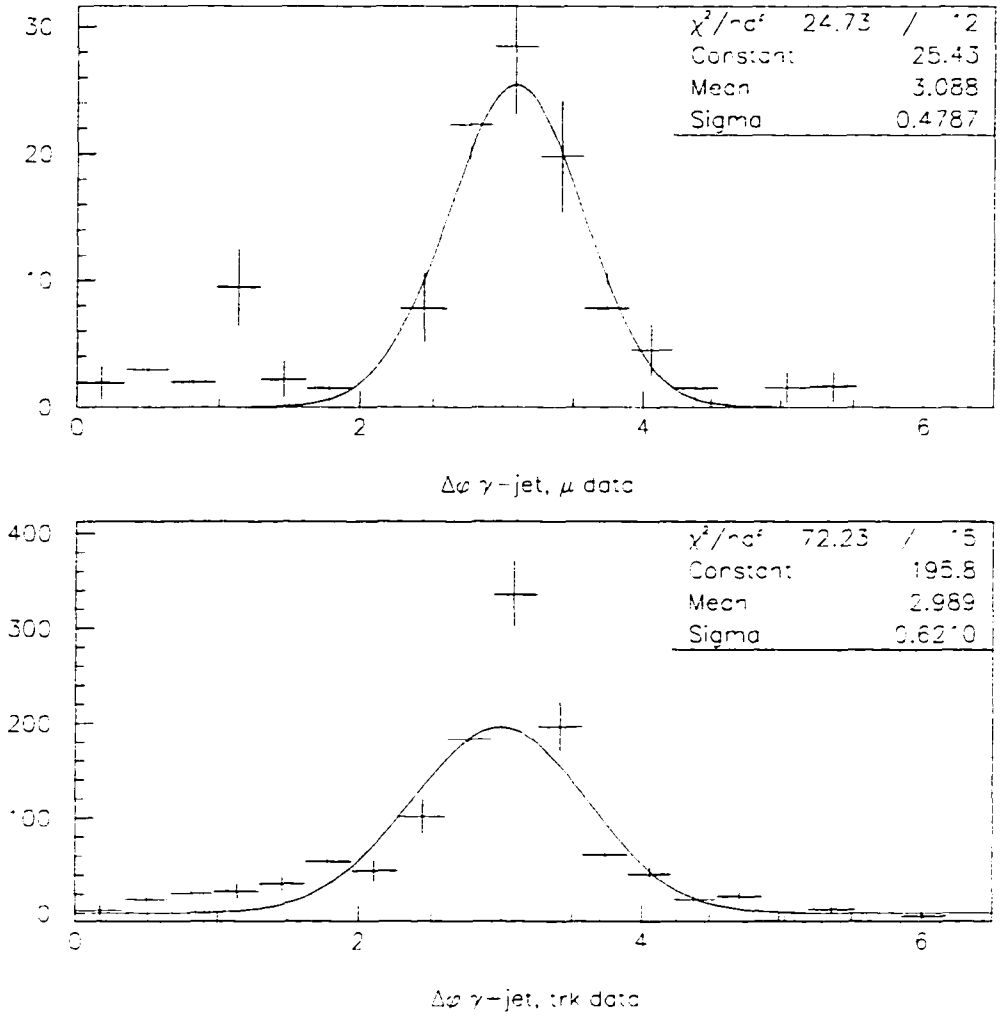

Figure 4-24: $\Delta\phi$ γ - jet for $\gamma - \mu$ data with a Gaussian fit superimposed, at top, and the same for $\gamma -$ jet data random tracks, at bottom.

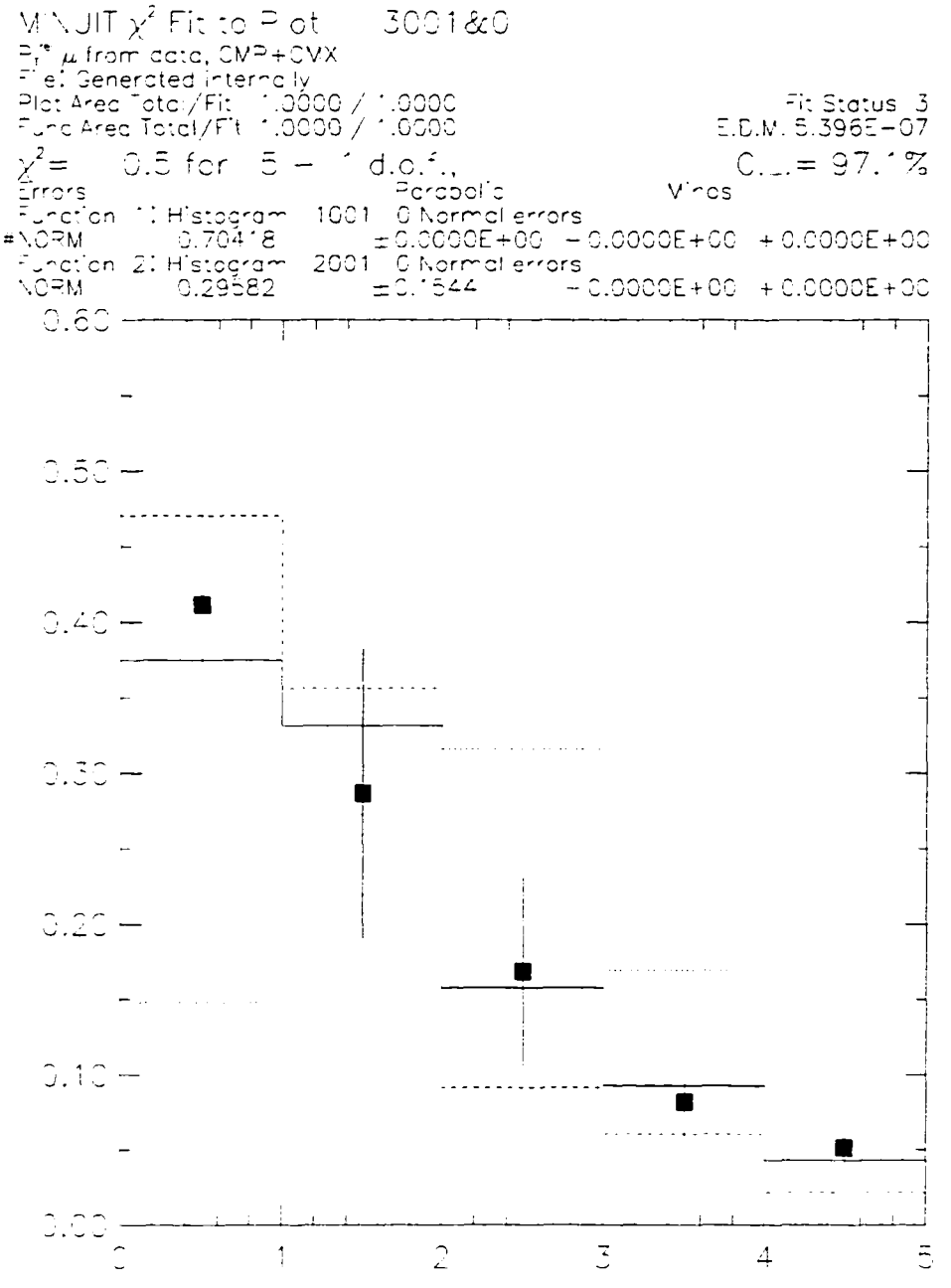

Figure 4-25: Constrained fit (solid histogram) of the data (points) P_T^{rel} distribution to a normalized sum of the smeared Monte Carlo c (dashed) and b (dotted) distributions, with the c and b templates superimposed. Both the c and b Monte Carlo templates have been smeared in $\eta - \phi$ space by a Gaussian with width 0.15, and, as can be seen, the χ^2 of the fit is very good. The bottom fraction found, $30 \pm 15\%$, is in agreement with theoretical predictions.

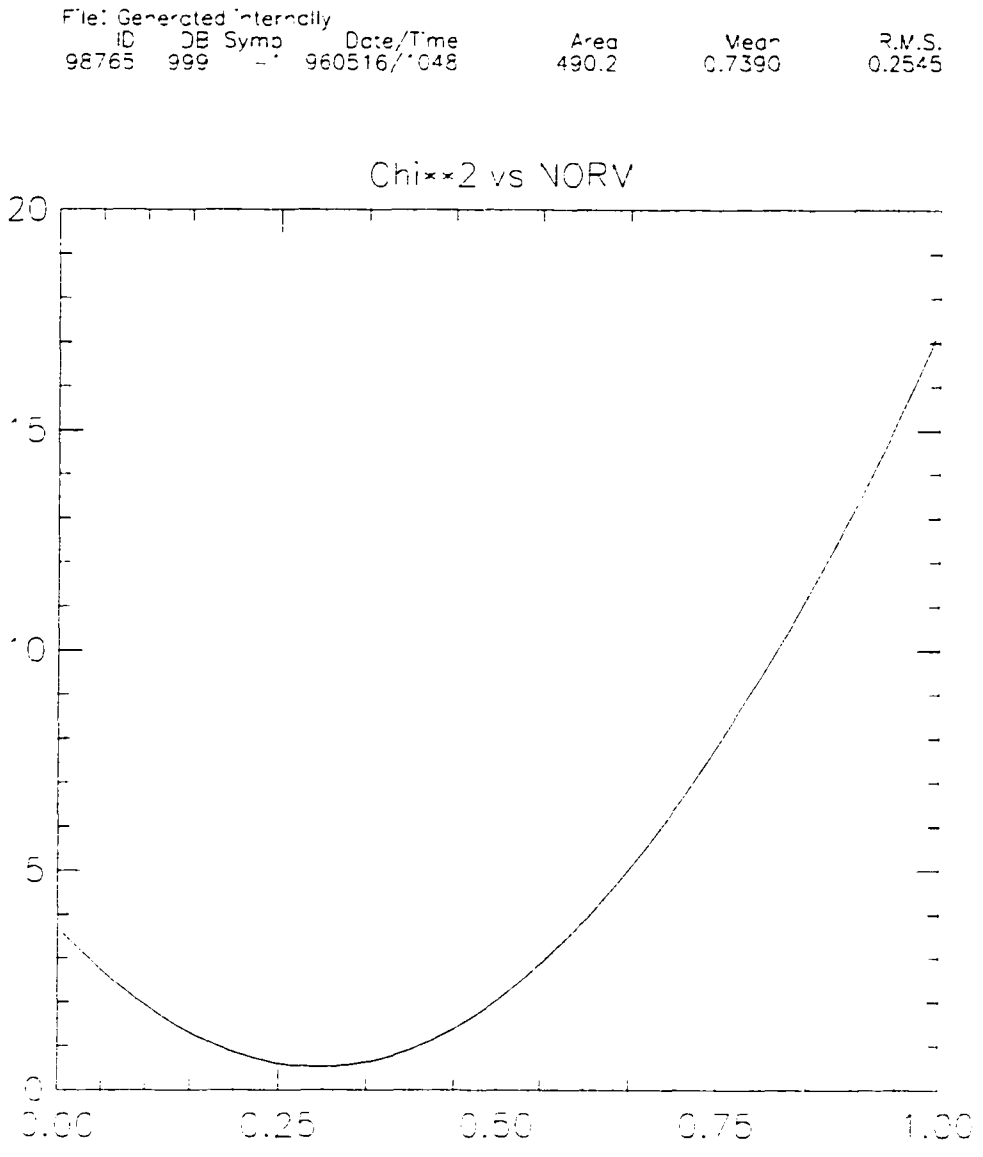

Figure 4-26: The χ^2 of the constrained fit of the data P_T^{rel} distribution to a normalized sum of the smeared Monte Carlo $\gamma-c$ and the smeared Monte Carlo $\gamma-b$, as a function of the b-fraction. A $\Delta\chi^2$ argument for the 90% confidence level limit with 4 degrees of freedom yields $\Delta\chi^2 = 7.78$, and thus a 90% confidence level limit that the bottom fraction in this data is less than about 80%.

4.8 Systematic Errors

The first systematic error we address is that due to the CMX accidental background subtraction. We calculate this by taking the statistical errors in the various background regions studied, and propagating these errors through the algebraic expression used to calculate the background. In this manner we find an error of 2.7 events, corresponding to 4% of the signal.

We next address our MC decay-in-flight estimate, for which there are a number of independent systematic errors. There is the error due to the uncertainty in the particle fractions, which we estimate by allowing the particle fractions to vary between the e^+e^- data given in Table 4.4, and find to be 6%. There is also an error due to the limited statistics of the charged particle spectrum used to generate our MC decay-in-flight estimate, which we find to be 3%, and an error due to the uncertainty in the number of interaction-lengths in front of the muon chambers for a decay-in-flight event, which we estimate by varying the number of interaction lengths in our MC simulation $\pm 10\%$, and find to be 3%.

The systematic error due to the muon acceptance and efficiency is estimated from the statistics of a MC with simulation study, and found to be 2%, while the systematic error due to the uncertainty in the CDF luminosity measurement is found to be 3.6% [42].

Finally, there are the systematic errors associated with the photon leg of the measurement. The error due to the uncertainty in the efficiency of the photon cuts was found to be 5%, while the error due to the uncertainty in the trigger efficiency was found to be 2%. The error due to the CES background subtraction method was determined by allowing the CES efficiency to fluctuate $\pm 1\sigma$ constrained by the CPR's measured efficiency, as described in [43], and found to be 9%.

4.9 Photon-Muon Cross Section

Finally we determine the photon-muon cross section. Adding up the number of real photon-muon events in Table 4.3, and using the acceptances and efficiencies in equations 4.1,4.7, and 4.8, we find a measured cross section for $p\bar{p} \rightarrow \gamma\mu X$ at $\sqrt{s} = 1.8$TeV with $17 < E_T^\gamma < 40$ GeV, $|\eta^\gamma| < 0.9$, $P_T^\mu > 4.0$ GeV, and $|\eta^\mu| < 1.0$ of:

$$\sigma^{\text{data}}_{p\bar{p}\rightarrow\gamma\mu X} = 29 \text{ pb} \pm 8 \text{ pb(stat.)} \pm 4 \text{ pb(sys.)}. \tag{4.18}$$

4.10 Comparison With Monte Carlo

For comparison, we present some theoretical estimates of the $p\bar{p} \rightarrow \gamma\mu X$ cross section. In this section we assume that the $\gamma\mu$ cross section is completely dominated by the γc subprocess, *i.e.*, that the bottom content of the photon data is negligible. As motivation for this assumption we note that, as discussed in Section 2.3, the theoretical estimates of the bottom fraction in the photon data are smaller than the systematic error on our measurement, let alone our statistical error.

With this in mind, we obtained a LO estimate of the $\gamma\mu$ cross section by using PYTHIA to study the γc Compton process, and correcting for the $c \rightarrow \mu X$ branching ratio. In this manner we find a LO cross section for $17 < E_T^\gamma < 40$ GeV, $|\eta^\gamma| < 0.9$, $P_T^\mu > 4.0$ GeV, and $|\eta^\mu| < 1.0$, with CTEQ2L structure functions, $Q^2 = P_T^2$, and full initial and final state parton shower modeling, of:

$$\sigma^{\text{PYTHIA}}_{p\bar{p}\rightarrow\gamma\mu X} = 10.3 \text{ pb} \pm 0.3 \text{ pb(stat.)}. \tag{4.19}$$

Recently, Lionel Gordon has published a full NLO calculation of the γc differential cross section as a function of the charm E_T. In order to compare this calculation with our data, one must not only correct for the charm branching ratio, but also for the charm acceptance and turn-on. In Figure 4-27 we display the efficiency for charm quark to decay into a muon in our fiducial η and P_T regions, as modeled by PYTHIA with Peterson fragmentation for a variety of values of the Peterson parameter ϵ.

Convoluting Gordon's differential cross section with our PYTHIA charm efficiency for $\epsilon = 0.06$ yields a NLO $\gamma\mu$ cross section for our cuts of:

$$\sigma^{\rm NLO}_{p\bar{p}\to\gamma\mu X} = 35 \text{ pb} \pm 1 \text{ pb(stat.)}. \tag{4.20}$$

Finally, we note that although the two Monte Carlo results presented here straddle the value of the measured cross section, given the errors on the measured value the NLO calulation is in very good agreement, and the LO PYTHIA prediction is within 2 σ. This agreement is in fact quite remarkable given that this is a first ever measurement, and that the theoretical calculations are dependent on the value of the charm parton density in a Q^2 and x regime that has never before been probed.

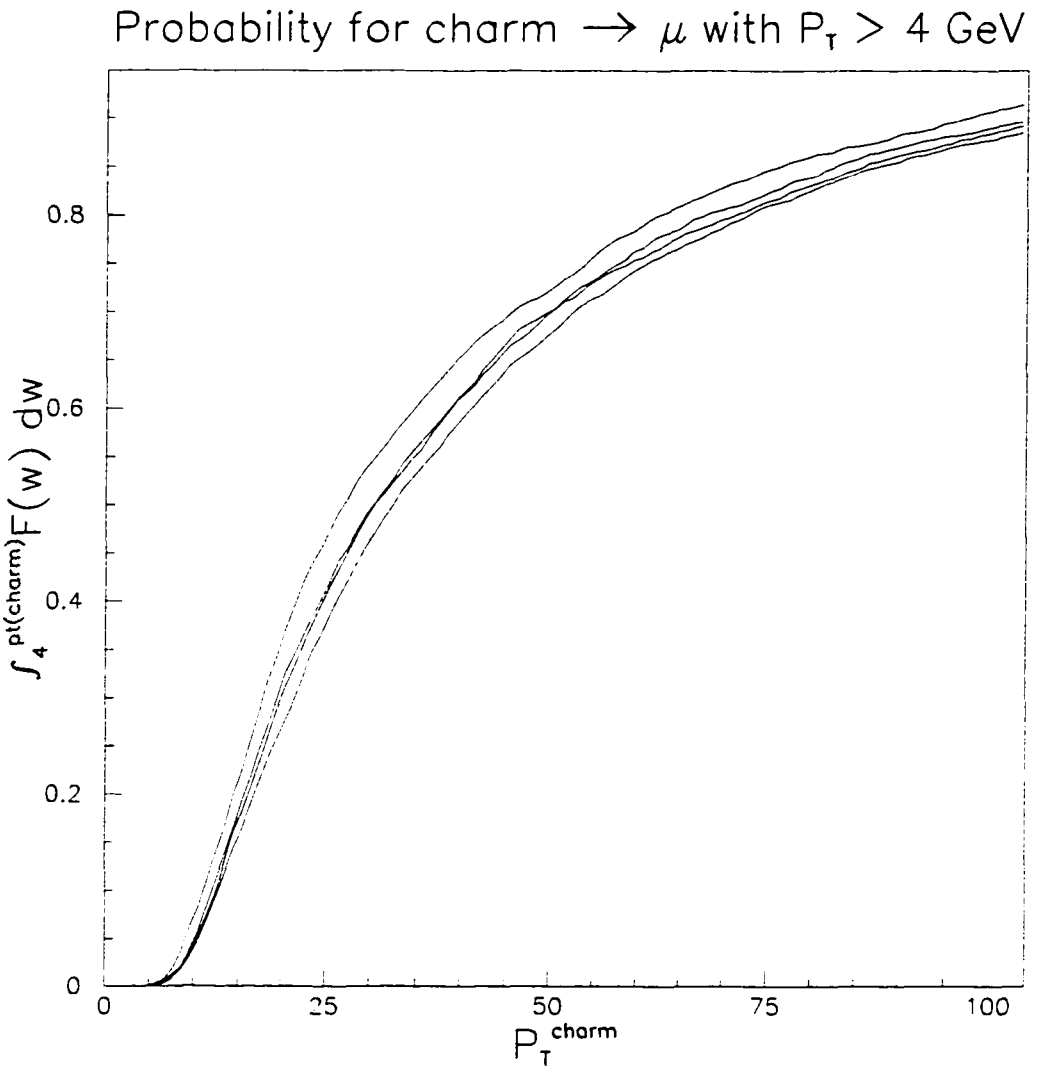

Figure 4-27: Efficiency for a charm quark to decay into a muon with P_T^μ above 4 GeV and fiducial to the CDF muon detectors, integrated over $P_T^\mu \geq P_T^c$. Curves displayed are for default PYTHIA fragmentation (at top), and for Peterson fragmentation with $\epsilon = 0.04$, 0.06, and 0.08 (below).

Chapter 5

Conclusions

We have measured the photon–muon cross section in $p\bar{p}$ collisions at $\sqrt{s} = 1.8TeV$ to be $29 \pm 8(stat) \pm 4(sys)$ pb for $|\eta_\mu| < 1.0$, $\eta_\gamma < 0.9$, $P_T^\mu > 4.0$ GeV, and $17 < E_T^\gamma < 40$ GeV. For comparison, we have studied the PYTHIA prediction for the LO $p\bar{p} \rightarrow c\gamma$ subprocess, and found that after correcting for the Particle Data Group inclusive charm branching ratio of $0.081^{+0.010}_{-0.009}$, the PYTHIA prediction is $10.3 \pm 0.3(stat)$ pb. In addition we have examined the NLO results of Bailey, Berger and Gordon, and found after correcting for the $c \rightarrow \mu + X$ branching ratio and convoluting their differential cross section with the PYTHIA prediction for the charm turn on with Peterson fragmentation and $\epsilon = 0.6$, a NLO value of $35 \pm 1(stat)$ pb. We find these quantities to be in good agreement.

In addition to this photon–muon analysis, there are two other analyses of the CDF Run 1A data that relate directly to the photon–charm cross section. A preliminary study of the photon–electron cross section has yielded $360 \pm 35(stat) \pm 51(sys)$ pb for $16 < E_T^\gamma < 40$ GeV, $P_T^e > 1.5$ GeV, and $|\eta_{\gamma,e}| < 1.0$ [22]. Also, a study of the photon–D^* cross section, where the D^* decays to a fully reconstructed $K\pi\pi$ final state, has yielded $380 \pm 150(stat) \pm 110(sys)$ pb for $|\eta_{D^*}| < 1.2$, $\eta_\gamma < 0.9$, $P_T^{D^*} > 6$ GeV and $16 < E_T^\gamma < 40$ GeV. These results, together with our photon–muon result, are shown in Figure 5-1, in ratio with their LO PYTHIA Compton $p\bar{p} \rightarrow c\gamma$ prediction, for the

appropriate fiducial volume. Again, we find good agreement.

Finally, we note that in the Tevatron Run 1B data, we added a dedicated photon–muon trigger, with the photon threshold reduced to $E_T^\gamma > 10$ GeV. The increase in luminosity in the 1B data sample (approximately a factor of 15), together with the lower photon threshold, promises vastly greater statistics for the Run 1B analysis.

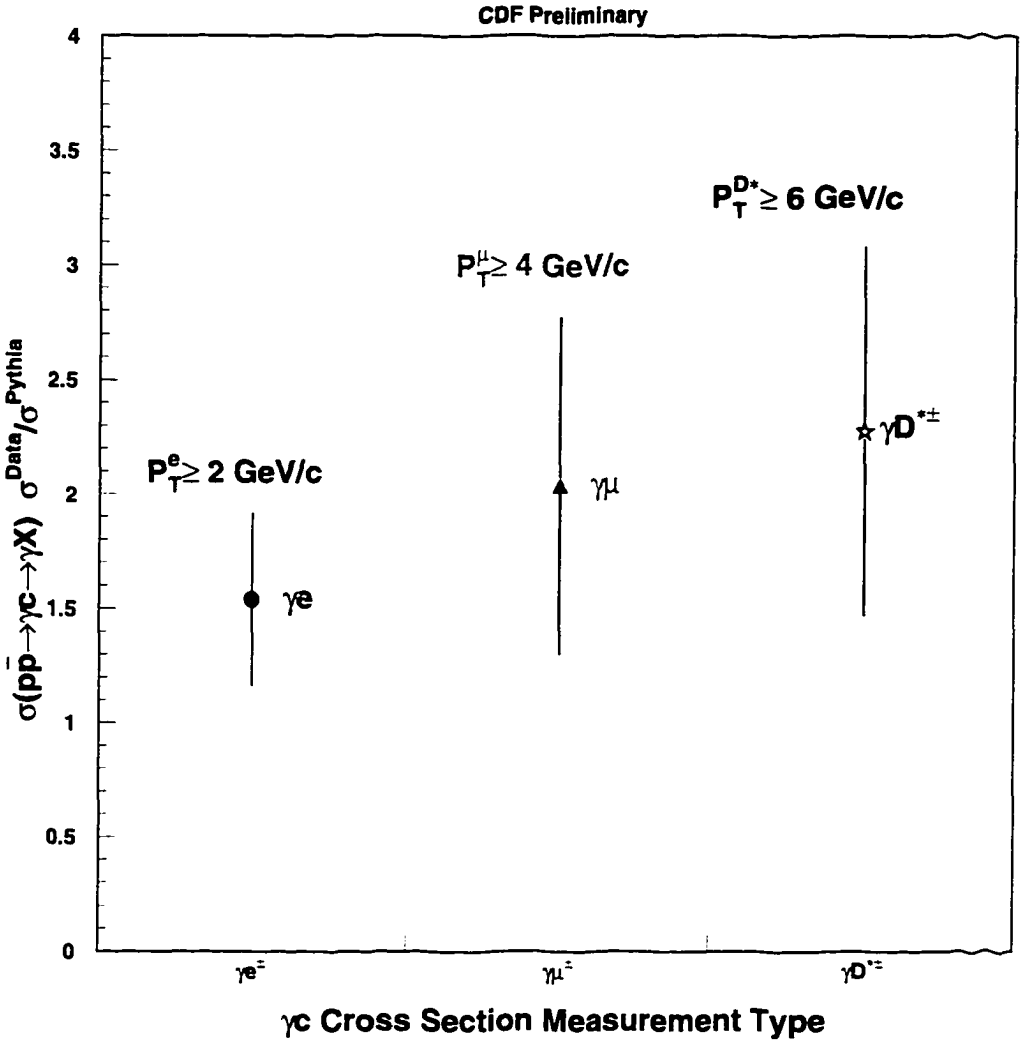

Figure 5-1: A comparison of the ratio of the measured photon-charm cross section to the PYTHIA prediction, for the three different analyses conducted at CDF during Run 1A.

Appendix A

Low Statistics Photon Background Estimate

The separation of real photons from background neutrals is accomplished using the different shower transverse profile sampled in the CES. The method compares the CES cluster shape to the expected one derived from the QFL detector simulation (calibrated using the electron test beam data) for single photons, and the result of the comparison is expressed in terms of a χ^2. Given a distribution in χ^2 we can extract the maximum likelihood number of photons and π^0's. If the statistics of the sample is large enough the method is well understood and has been used several times in CDF [21]. The maximum likelihood method can be implemented by weighting every event with a number. This number can be positive or negative so, if applied blindly for a small number of events, sometimes the surprising answer is that the expected number of photons in the sample is negative. At the same time the error bars have to be large enough to cover zero, and are overestimated. The solution to this problem is to get a step back and to calculate the full likelihood function and maximize it directly. As we are going to see, for small statistics event weights cannot be defined.

An experiment is performed where two possible results are assumed: photons and pions. We want to measure a quantity $0 \leq \chi^2 \leq 20$, and we are going to record the

following numbers: $N_- \equiv N(\chi^2 \leq 4)$ and $N_+ \equiv N(\chi^2 \geq 4)$.

We think we know the probability for a photon to have $\chi^2 \leq 4$: γ, and to have $\chi^2 \geq 4$: $\Gamma = 1-\gamma$. Analogously, the probability for a pion to have $\chi^2 \leq 4$ is known and equal to π, and for $\chi^2 \geq 4$ is $P = 1-\pi$. Now, given N_+ and N_-, we want to estimate N_γ and $N_\pi = N_+ + N_- - N_\gamma$. We are going to do this by maximizing the likelihood that a sample of N_γ photons and N_π pions produces N_+ and N_- experimentally.

Calling i the number of photons out of N_γ with actually $\chi^2 \leq 4$, the likelihood is:

$$L(N_\gamma) = \sum_i C_i^{N_\gamma} \gamma^i \Gamma^{(N_\gamma - i)} C_{(N_- - i)}^{N_\pi} \pi^{(N_- - i)} P^{(N_\pi - N_- + i)} \tag{A.1}$$

where C_i^N is the number of combinations of N elements in groups of i. We have only one degree of freedom that we choose N_γ.

The summation is just a convolution of the photon and pion binomial distributions. Assuming now that N_+ and N_- (and then N_γ and N_π) are large numbers we can substitute the binomial distributions by its Gaussian limit, and the summation by an integral.

Calling $G(x, x_0, \sigma^2)$ the Gaussian function with mean x_0 and rms σ calculated at the point x, we write:

$$L(N_\gamma) \rightarrow G(N_-, N_\gamma\gamma + N_\pi\pi, N_\gamma\gamma\Gamma + N_\pi\pi P). \tag{A.2}$$

Maximizing $L(N_\gamma)$ we get,

$$N_\gamma = \frac{1}{\gamma - \pi}(PN_- - \pi N_+) \tag{A.3}$$

and weights can be defined:

$$W(+ \rightarrow \gamma) \equiv \frac{-\pi}{\gamma - \pi} \leq 0 \tag{A.4}$$

$$W(- \rightarrow \gamma) \equiv \frac{P}{\gamma - \pi} \geq 0 \tag{A.5}$$

This is the standard CDF method. But now we see that the weights have no real meaning when the statistics is poor. The likelihood function (A.1) is very different of a Gaussian, we cannot pass from the summation to an integral and, in summary, the value of N_γ that maximizes the likelihood function is not given by (A.3).

In this analysis, the function (A.1) was built and maximized numerically. The error was defined by a change of the log of the maximum likelihood by one unit.

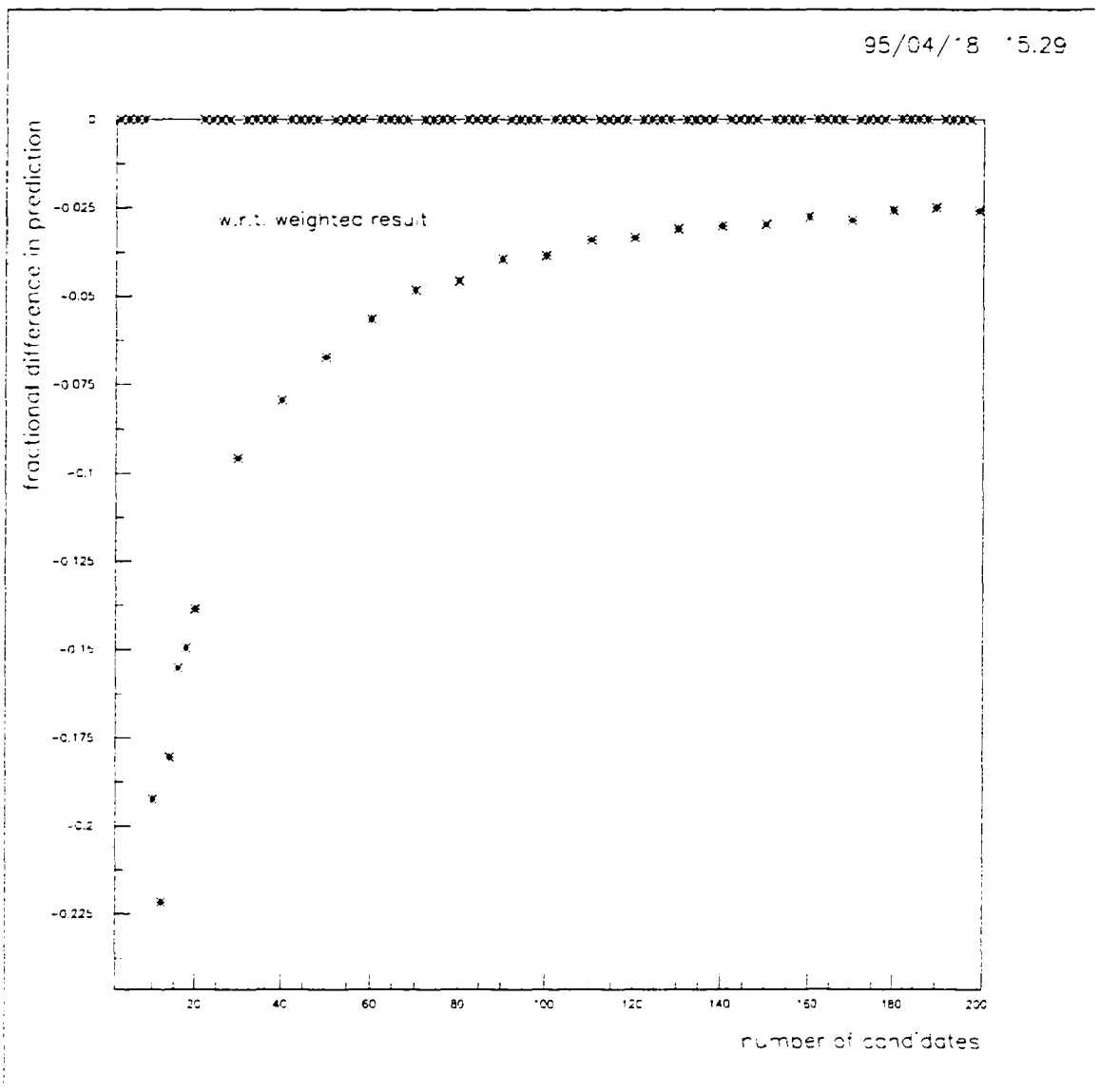

Figure A-1: Fractional difference in the predicted number of photons between our likelihood code and the standard photon weighting method, as a function of the number of photon candidates.

Bibliography

[1] M. Gell-Mann, Phys. Rev. **125**, 1067 (1962), and Y. Ne'eman, Nucl. Phys. **26**, 222 (1961).

[2] A. Salam, *Elementary Particle Theory: Relativistic Groups and Analyticity* (8th Nobel Symposium), 1968, p. 367.

[3] A sampler of texts which review the Standard Model includes: C. Quigg, *Gauge Theories of the Strong, Weak, and Electromagentic Interactions,* Benjamin, 1983; H. Georgi, *Weak Interactions,* Addison–Wesley, (1986); Aitcheson and Hey, *Gauge Theories in Particle Physics,* Adam Higler, Bristol and Philadelphia, (1989).

[4] G. Arnison, *et. al.*, Phys. Lett. B **122**, 103 (1983), Phys. Lett. B **126**, 398 (1983), and the references there contained.

[5] H. D. Politzer, Phys. Rev. Lett. **30**, 1346 (1973), D. Gross and F. Wilczek, **ibid.**, 1343.

[6] A.D. Martin, R.G. Roberts and W.J. Stirling, *Structure Functions and Parton Distributions*, Int. J. Mod. Phys. A **10** (1995) 2885–2900.

[7] CTEQ Collaboration (James Botts *et al.*), *CTEQ Parton Distributions and Flavor Dependence of Sea Quarks*, Phys. Lett. B **304**, 159 (1993,)hep-ph/9303255.

[8] Particle Data Group, Phys. Rev. D **45**, 11 (1992).

[9] G. Altarelli, *Partons in QCD*, Phys. Rep. **81**, 1 (1982).

[10] CCFR Collaboration, Z. Phys. C **44**, 187 (1989).

[11] J.J. Aubert *et al.*, Nucl. Phys. B **213**, 31 (1983).

[12] R.S. Fletcher, F. Halzen and E. Zas, Phys. Lett. B **221**, 403 (1989).

[13] M. Stratmann and W. Vogelsang, DO-TH 94/23.

[14] T. Sjöstrand, Comput. Phys. Commun. **82**, 74 (1994).

[15] B. Bailey, E. Berger, and L. Gordon, *Production of a Prompt Photon in Association with Charm at Next-to-Leading Order in QCD*, ANL-HEP-PR-95-87, EC-HEP-960201.

[16] Steve Kuhlmann, private communication.

[17] B. Bailey, E. Berger, and L. Gordon, *Prompt Photon plus Charm Quark Production at Colliders*, ANL-HEP-PR-96-16.

[18] R.Oishi,S.Kuhlmann,B.Flaugher,*Analysis of Photon + Dstar (I)*, CDF2234.

[19] F. Abe *et al.*, The CDF Detector: An Overview, Nucl. Instrum. Methods Phys. Res. A **271**, 387 (1988).

[20] M.W. Bailey *et al.*, *CTC Tracking Efficiency for the B Cross-section Analysis*, CDF2815.

[21] F. Abe *et. al.*, *Prompt Photon Cross Section Measurement in $\bar{p}p$ Collisions at $\sqrt{s} = 1.8$GeV*, Phys.Rev.D48:2998-3025,1993.

[22] Dan Crane, *Measurement of the Photon Electron Cross Section*, CDF2511.

[23] Phil Koehn *et al.*, *Measuring the Bottom and Charm Rates in an Inclusive Jet Sample and the Direct Photon Sample*, CDF2212.

[24] P. Schlabach and J. Troconiz, *Calibration of the CMX Drift Velocity and Alignment in Run 1A*, CDF2332.

[25] D. Reich, D. Kestenbaum, P. Schlabach and J. Troconiz, *A New Algorithm for Stub Reconstruction in the CMX Detector*, CDF2871.

[26] R. Hamilton, P. Schlabach, and J. Troconiz, *CMX Low p_T Muons in the Run 1A Photon Sample*, CDF2843.

[27] Carol Anway-Wiese, *Offline Muon Matching Cuts*, CDF1986.

[28] Todd Huffman, Ph. D. Thesis, Purdue Univesity, 1992.

[29] Intae Yu and Michael Schmidt, *Studies of Muon Backgrounds in Low P_T Dimuon Events*, CDF2674.

[30] David Smith, Ph.D. Thesis, University of Illinois Champagne-Urbana, 1989.

[31] P.B. Straub et al, Phys. Rev. D **45**, 3030 (1992).

[32] D. Antreasyan et al, Phys. Rev. D **19**, 764 (1979).

[33] T. Alexopoulos et al, Phys. Rev. Lett. **64**, 991 (1991).

[34] F. Abe et al, Phys. Rev. D **40**, 3791 (1989).

[35] F. Abe et al, Phys. Rev. Lett. **61**, 1819 (1988).

[36] TASSO Collaboration, Z. Phys. C **17**, 5 (1983), and Z. Phys. C **42**, 189 (1989.

[37] OPAL Collaboration, CERN-PPE/94-49, March 1994.

[38] ALEPH Collaboration, CERN-PPE/94-201, December 1994.

[39] Bob Mattingly, *The b-bbar Content of High Mass e-mu Data*, CDF2190.

[40] Alain Gauthier, *The Central Muon Trigger for the 1991 Run*, CDF1186.

[41] P. Lukens, P. Schlabach, and A. Gauthier, *Proposal to Fill the Eta Acceptance of CMP in the Trigger*, CDF1449.

[42] Stefano Belforte, Paul Derwent, John Marriner, Carla Grosso-Pilcher, σ_{BBC} *Updates*, CDF2535.

[43] Arthur Maghakian and Steve Kuhlmann, *Calibration of the CPR Conversion Probability from* $\rho^{\pm}$ *to* $\pi^0\pi^{\pm}$, CDF2478.